Università degli Studi di Catania

Dottorato di Ricerca in Fisica
XXIV Ciclo

Egidio Carria

Amorphous-Crystal Phase Transitions in $Ge_2Sb_2Te_5$ and Ge_xTe_{1-x} alloys

Tutor: Prof.ssa M. G. Grimaldi
Prof. E. Rimini

Coordinatore: Prof. F. Riggi

Tesi per il conseguimento del titolo
2008-2011

Contents

Introduction

The information and knowledge-based society creates a huge demand for data storage capacity. A wide range of commercially storage technologies try to meet this demand. These technologies differ in specific properties, such as the storage capacity and density, the speed at which data can be written, read and erased. Other important attributes include the cyclability (the number of write-erase cycles that can be performed by a storage device), the lifetime, the volatility (whether the stored data is lost if the electric power supply is turned off), and the cost of the final product. The rapid growth of the data storage market has been driven by the personal computer revolution followed by the multimedia revolution.

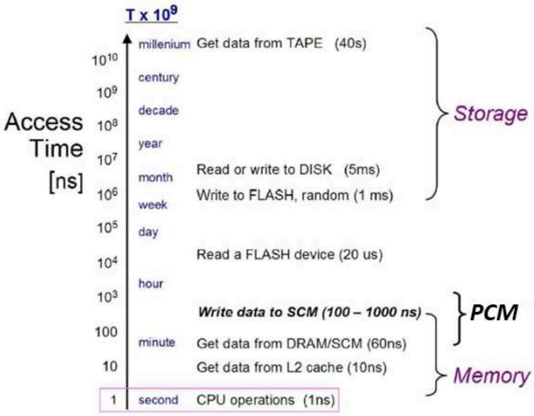

Fig. I.1 **Access times for various storage and memory technologies, both in nanoseconds and in terms of human perspective. For the latter, all times are scaled by 10^9 so that the fundamental unit of a single CPU operation is analogous to a human making a one-second decision [Bur10].**

There are three main types of data storage technologies: solid state memories, magnetic storage and optical storage. Each of them has its own characteristics, and within each type there is also a wide variation in the capabilities of each product [Bur10]. Figure I.1 shows, for example, the access times for various storage and memory technologies [Bur10]. Magnetic storage is five orders of magnitude slower than solid state memories. On the other hand, fig I.2 reports a qualitative representation of the cost and performance of various technologies, ranging from extremely dense yet slow Hard Disk Drives (HDD) to ultra-fast but expensive SRAM [Bur10].

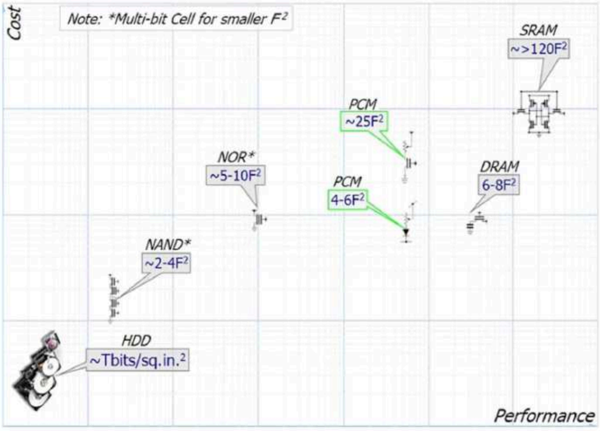

Figure I.2 Qualitative representation of the cost and performance of various storage technologies. F is the size of the smallest lithographic feature, and a smaller device footprint leads to higher density and thus lower cost.

So far, no practical universal storage medium exists, and all forms of storage have some weak point. Therefore, a computer system usually contains several kinds of storage, each with an individual purpose. Solid-state memories, which have high-speed and compact size, are mainly used as the primary memories, while magnetic and optical storage devices are typically used as the secondary storage device for computer systems. Hard disk drives, which are the primary type of magnetic storage devices, are widely used for high growth rate in areal density and low cost. They have been and still remain the choice for the secondary storage device in most of the computer systems. Recently removable hard disk drives have become popular. Optical storage offers a reliable and removable storage medium with excellent robustness, long lifetime, low cost and non-contact data retrieval. Moreover, this technology provides read only, write once read and rewritable functions. With the rapid development of portable electronics, such as mobile phones and digital cameras, non-volatile solid state memory (Flash) is becoming more and more important among the solid-state memories. In particular, starting from his basic patents in the 80s, Flash market has grown in less than three decades to become a 20 billion dollars market [Ful02][Lai08]. This growth has been possible by the increase in the system functionality that can be delivered in the same size package [Moo65]: higher densities at similar cost lead to more functionality and thus more applications which then attracts investment for the additional research needed to implement the next size smaller device. Beyond the future, while the device size may be scheduled, for the first time in many years it is not clear exactly how to achieve this target. New patterning techniques will almost certainly be required, alternative cell designs were proposed involving the replacement of the polysilicon floating gate [Whi00] or the exploration of new complicated 3-D structures [Jun06]. Fortunately, new non-volatile memory technologies have been under consideration as possible Flash substitutes [Bur08]: ferroelectric and magnetic RAM, organic RAM, resistance RAM and phase-change memories (PCM). The idea to use an amorphous-to-crystalline phase transition for information storage dates back to the 1960s when S. R. Ovshinsky suggested a memory switch based on changes in the properties of amorphous and crystalline phases of multicomponent chalcogenides [Ovs68]. A landmark was achieved in the late 1980s by Yamada *et al.* that discovered the phase changing properties of GeTe-Sb_2Te_3 pseudo-binary alloys [Yam87]. Starting from these studies Matsushita/Panasonic developed phase-change optical disk technology that remained stable over a million use cycles. This technology became the mainstream in optical disc production and in the late 1990s resulted in the commercialization of 4.7 GB digital versatile disc random access memory (DVD-RAM). With the introduction of blue laser light and maximization of the numerical aperture, the race for higher resolution and hence the development of this field may at first seem exhausted. Room for increasing storage capacity would be left only by increasing the number of data layers per disk [Shi08]. At present, a 100 GB disk employing three data layers marks the upper limit for such data storage devices, paving the way to the fourth generation of commercial optical phase-change based media [Tom08]. On the other hand, when phase-change materials were introduced by Ovshinsky, electronic memories were among their first suggested applications. Nevertheless, only now due to the availability of fast-switching phase change materials and the ability to create nanoscaled structures, it is possible to realize competitive, non-volatile phase change based electronic memories: *phase-change random access memory* , usually abbreviated *PCM* or *PCRAM* [Ter09]. As shown in the next paragraph, operation can proceed on the timescale of few nanoseconds which is orders of magnitude faster than Flash. This puts PCM in a position of a universal memory, that combines the best of both DRAM and Flash (see fig. I.1 and I.2). Moreover, the attainable scalability even surpasses the existing memories, while having low power consumption. Hence, it is not surprising that the development of such memory cells has benefited from many industrial contributions. Phase change materials are attractive for memory applications since they possess a unique property portfolio [Wut07] [Len11]. The uniqueness of this class of materials consists in the combination of high structural stability of both phases up to moderate temperatures (T~150 °C) and extremely fast phase transitions at high temperatures (t~10-100 ns). Moreover, a pronounced difference of optical and electronic properties, depending upon their atomic arrangement (amorphous or crystalline) allows to distinguish different logic states. This combination of properties also provides a unique opportunity to test the relationship between bonding and the atomic arrangement in solids and their correlation to solid state properties.

As we pointed out before, optical disks and phase change memories are functional and commercially available starting from the '90s. Despite this, fundamental aspects about the correlation between the properties and the local structure (bonding and arrangement) are still under investigation. It is not clear if the property contrast between the different phases is correlated to variations in the short or long range order. On the other hand the phase change mechanism responsible for the ultra-fast crystallization is not unambiguously understood. Many models have been proposed in the last decade and sometimes conflicting results are reported in the literature. Considerable effort has been put forward to identify materials that provide the required property combination and just recently a scheme based solely on the stoichiometry has been reported to predict which alloys fulfill the relevant criteria of contrast and speed [Len08]. Moreover, the influence of doping species is a nodal point to increase both the stability of the different phases and the switching velocity but a detailed and systematic analysis of this process is still lacking. Another interesting topic is correlated to the effect induced by laser or ion irradiation on the stability of the amorphous phase. In particular, ion irradiation with self-atomic species, produces a variation in the short-range order that affects the crystallization temperature of the alloys.

The need of reliable data and interpretation has been the motivation of the present work. Several experiments have been led to gain more insight into the fascinating world of Phase Change Materials and a significant effort has been also devoted to provide a solid interpretation of the experimental results. This dissertation presents the study of many open topics and we will discuss them according to the following scheme. In Chapter 1 the general concepts necessary to introduce the thesis work are given. A brief overview on the properties of phase change materials that allow their use in data storage devices is presented. On the other hand the functioning and the main characteristics of these devices will be discussed. The theory of the crystallization process will be presented in Chapter 2 pointing out the peculiar characteristics of phase change materials that require a deeper investigation. In Chapter 3 we will then discuss the crystallization process of as deposited $Ge_2Sb_2Te_5$ thin film induced by conventional or laser annealing. In the first case the glass temperature regime will be investigated whereas in the second case the ultra fast crystallization regime will be probed below the melting point. A unified analysis of these results will be proposed. The correlation between the local order in the amorphous network and the crystallization kinetics will by studied varying the properties of the amorphous phase and looking to the consequent variation in the phase transition speed. Both laser and ion irradiation will be used to this aim. In the second case is possible to study the role of several parameters like the fluence (i.e. the energy deposited) or the implantation temperature. The influence of a capping layer on this phenomenon will be tackled. In Chapter 4 we will discuss the crystallization process in Ge_xTe_{1-x} alloys looking to the influence of stoichiometry on the phenomenon. Recently, these compounds have attracted again great attention for high temperature applications since they present significant improvement of data retention with respect to the commonly used $Ge_2Sb_2Te_5$ and an excellent contrast in terms of electrical resistivity between the two states. Also in this case we will tackle the correlation between the local order of the different amorphous states (as deposited, ion and laser irradiated) and the crystallization kinetics.

References

[Bur08] G. W. Burr, B. N. Kurdi, J. C. Scott, C. H. Lam, K. Gopalakrishnan, and R. S. Shenoy, *IBM Journal of Research and Development*, 52(4/5) 449-464 (2008).

[Bur10] G. W. Burr, M. J. Breitwisch, M. Franceschini, D. Garetto, K. Gopalakrishnan, B. Jackson, B. Kurdi, C. Lam, L. A. Lastras, A. Padilla, B. Rajendran, S. Raoux, and R. S. Shenoy, *J. Vac. Sci. Technol. B,* 28 223 (2010).

[Ful02] B. Fulford, *Forbes*, June 24 (2002).

[Jun06] S.M. Jung, J. Jang, W. Cho, H. Cho, J. Jeong, Jaehun, Y. Chang, J. Kim, Y. Rah, Y. Son, J. Park, M.-S. Song, K.-H. Kim, J.-S. Lim, and K. Kim, *EDM Technical Digest*, par. 2.3 (2006).

[Lai08] S. Lai, *IEDM 2008*, pag. 01-02 (2008).

[Len08] D. Lencer , M. Salinga , B. Grabowski , T. Hickel , J. Neugebauer, M. Wuttig, *Nature Materials*, 7 , 972 (2008).

[Len11] D. Lencer, M. Salinga, M. Wuttig, *Adv. Mater.*, *23*, 2030–2058 (2011).

[Moo65] G. E. Moore, *Electronics*, 38(8) 114-117 (1965).

[Ovs68] S.R. Ovshinsky, *Phys. Rev. Lett.,* 21, 1450 (1968).

[Shi08] L. Shi, *Phase Change Materials Science and Applications*, chap. 12, Springer (2008).

[Ter09] M. Terao, T. Morikawa, T. Ohta, *Jpn. J. Appl. Phys.*, 48 080001 (2009).

[Tom08] J. Tominaga, *Phase Change Materials Science and Applications*, chap. 13, Springer (2008).

[Whi00] M. H. White, D. A. Adams, and J. K. Bu, *IEEE Circuits and Devices*, 16(4) 22-31 (2000).

[Wut07] M. Wuttig, N. Yamada, *Nature Materials,* 6, 824 (2007).

[Yam87] N. Yamada, E. Obno, N. Akahira, K. Nishiuchi, K. Nagata, M. Takao*, Jpn. J. Appl. Phys. Part 1,* 26, 61 (1987).

Chapter 1

Phase Change Materials: Physics and Applications

The chapter presents an overview of the properties of the phase change materials relatively to their use as active medium in optical and electronic devices.

1.1 Optical and electronic devices

The initial work on optical storage began in the 1950s and 1960s [Ovs68]. Although the research had been conducted for several decades, the first popular system was the Compact Disc-Read Only Memory (CD-ROM) which was introduced in 1982, adapted as the first mass market optical storage medium with write once read many capability as CD-R (Compact Disc-Recordable) in 1988 and with rewritable capability as CD-RW (Compact Disc-ReWritable) in 1997. The optical media can be grouped into three types, read only memory (ROM), write once read many (R) and rewritable (RW) optical disc. Optical storage is removable that is the reason why standards are needed for every generation[Shi08]. When a new generation is developed, such as moving from CD to DVD, and DVD to BD, one very critical issue is the compatibility because the global standards for music, video and computer software are well accepted. Thus each generation of optical storage needs to be compatible with interchangeable media and backward standards. Current rewritable discs such as CD-RW, DVD±RW, DVD-RAM, and BD-RE are all based on phase-change optical recording technology using phase change materials for the recording layers [Tom08]. The functioning is based on the large change in reflectivity of these materials when they switch from amorphous (R~50%) to crystalline (R~70%) phase or vice versa. Reversible phase transitions are induced by heating the material via laser pulses of proper intensity and duration.

Amorphization is obtained by the formation and the subsequent quenching of the liquid phase, whereas crystallization occurs by heating the system below the melting point. Amorphization is achievable by pulses shorter then ~10ns and quenching rate higher than ~10^7 K/s whereas crystallization by longer pulses (~100ns) at lower power. A schematic representation of the write-erase mechanism is reported in Figure 1.1 [Sal08].

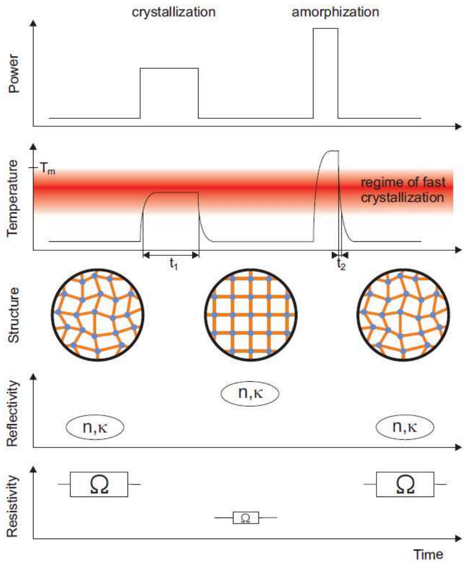

Figure 1.1 Programming of a phase change memory involves application of electrical or laser pulses leading to internal temperature changes that either melt and then rapidly quench a volume of amorphous material (RESET), or hold this volume at a slightly lower temperature for sufficient time for recrystallization (SET). The property contrast in reflectivity (symbolized by the optical constants n and κ) or resistivity (symbolized by resistors marked with an Ω of varying size) can be detected with probe powers that are reduced avoiding modifications of the structural state [Sal08].

Many materials, such as In-Sb, Ag-Zn, Ge-Sb-Te, Ge-Te-Sn, Sb-Se-Te, Ga-Se-Te, In-Sb-Te, Ag-In-Sb-Te etc. have been reported to be potential candidates for phase-change optical data storage. Among all kinds of phase-change materials, stoichiometric compositions along the GeTe-Sb_2Te_3, pseudo-binary line and quaternary AgInSbTe alloys are widely used in phase change optical storage. Figure 1.2 shows the ternary phase diagram depicting different phase change alloys, their year of discovery, and their use in different optical storage products [Wut07].

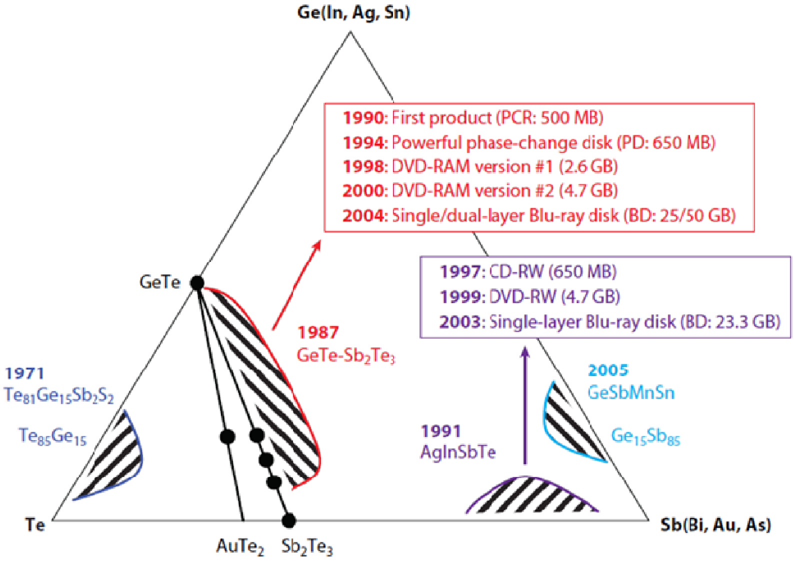

Figure 1.2 **Ternary phase diagram depicting the different phase change alloys used as recording layer in optical disks. The year of discovery and the different products are also reported [Wut07].**

In particular optical storage systems consist of a drive unit and a storage medium in a rotating disc form. In general the discs are pre-formatted using grooves and lands (tracks) to enable the positioning of an optical pick-up and recording head to access the information on the disc. Under the influence of a focused laser beam emanating from the optical head, information is recorded on the media as a change in the material characteristics. The crystalline/amorphous pits in the tracks correspond to the zeros and ones of the digital information. In the early rewritable phase-change discs, amorphous marks were recorded only on the grooves, whereas the lands served as the guides for tracking and the suppression of heat flow from the adjacent groove tracks [Shi08]. In fig.1.3 (a) and (b) a schematic view of the optical disk structure and a transmission electron micrography of a DVD-RAM (produced by Panasonic) are shown, respectively [Yam08] [Rao09]. Submicrometric amorphous marks are clear visible within the track pitches. In past decades, the recording density of optical disks has been increased by roughly a factor of a hundred up to a mark length of 150nm. Simultaneously the data-transfer rate was increased by a factor of a thousand up to 36Mbps. Progress was made by reducing the wavelength of the laser used to induce phase transitions, from infrared to red and from red to blue-violet, increasing the numerical aperture of the lens used, from 0.5 to 0.6 and from 0.6 to 0.85, recording on both land and grooves, doubling the recording layers from single to dual, and making use of improved software algorithms. These results are summarized in fig. 1.4 [Wut07].

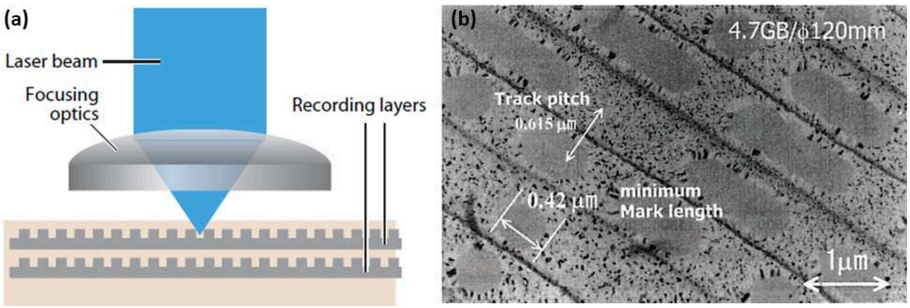

Figure 1.3 (a) Schematic of a dual-layer recording disc. The recording is done in the groove to isolate adjacent tracks [Rao09]. (b) Planar observation of recorded mark on DVD-RAM media (Panasonic, Japan). Submicrometric amorphous marks are clear visible within the track pitches. Decreasing the mark length allows to increase the recording density [Yam08].

To keep the pace of product development, a number of competing technologies are being considered. At present it is not clear which approach will prove superior, so only two concepts are briefly sketched [Tom08]. One is the near-field approach, in which a lens with a large numerical aperture is brought very close to the storage medium. At distances $d < \lambda/2$, the evanescent wave still has components at the wavelength inside the lens. These components allow much higher spatial resolution and ideally could increase the storage density by $1/n^2$, where n is the refractive index of the material. The main challenge for system reliability is the close spacing between the lens and the storage medium. Another way of increasing capacity uses the super-resolution near-field structure effect (super-RENS). Here, an optical element is placed close the surface of the medium, at a distance that is much smaller than the optical wavelength. This allows to employ evanescent waves to manipulate bits on the medium beyond the diffraction limit. The precise origin of the super-RENS phenomenon has not yet been identified.

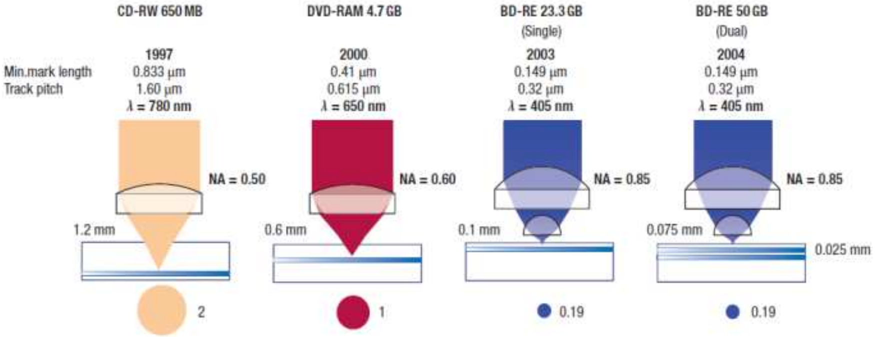

Figure 1.4 Comparison of optics, recording densities, recording capacities and disk structures used for CD , DVD and BD. Changes in the lens system are shown in the upper portion; the disk structure is depicted beneath. The change in beam cross-section is displayed at the bottom [Wut07].

As we pointed out before, when phase-change materials were introduced by Ovshinsky [Ovs68], electronic memories were among their first suggested applications. Fueled by the success of phase change optical storage, PCM technology has seen a great interest in research and development activities. These devices couple non volatility with high scalability (~50nm), low power consumption (~10mW) and short write/erase time (~10ns). This puts PCM in a position of a universal memory, that combines the best of both DRAM and Flash [Bur10]. As in optical disks, the cell operation is based on a thermally-induced phase change in the active chalcogenide layer, fig.1.1 . The amorphous phase is characterized by a large resistivity, while in the crystalline phase the resistivity is orders of magnitude lower. The chalcogenide phase can then be easily recognized by a voltage or current sensing of the cell. The phase in the chalcogenide material can be changed by the application of electrical pulses: to transform the crystalline phase into amorphous (reset operation), the pulse current must deliver enough Joule heating to raise the temperature above the melting point. The liquid phase is then quenched in a disordered amorphous phase.

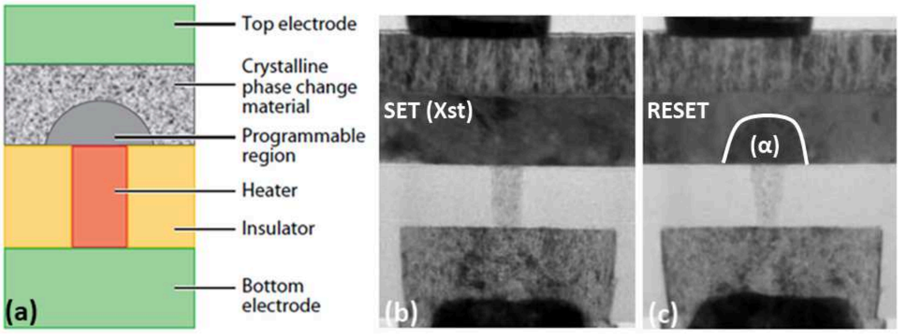

Figure 1.5 **(a) Schematic of a mushroom PCM cell. A typical electrode material is TiN with an insulator material SiO_2, and a PCM consisting of doped $Ge_2Sb_2Te_5$ [Rao09]. (b)(c) Transmission electron micrography cross-sections of a mushroom cell in the SET state and RESET state. In the first case the active layer is polycrystalline throughout. In the RESET state, a "mushroom cap" of amorphous phase change material is clearly visible over the heater [Bre08].**

The crystalline phase can be recovered by the application of a current pulse (set operation), able to heat the active layer below the melting point, but high enough to allow a fast crystallization of the amorphous structure. In the set state usually the whole chalcogenide layer is in the crystalline phase (fig.1.5(b)), while in the reset state, the amorphous phase occupies a typical dome-shaped volume (fig.1.5c)). This is the case for the so-called mushroom cell, shown in fig.1.5 [Rao09][Bre08]. The chalcogenide layer (e.g. doped GST) is embedded between a top electrode (W) and an insulator layer (Ta_2O_5/SiO_2). For efficient Joule heating in the cell, a strong confinement of heat and electrical currents is needed. The lower electrode, also known as the 'heater', is then usually shaped like a pillar within the insulator. W or TiN are generally used. The heater size is defined by lithographic techniques. After filling the hole with a conducting material, the extra W is removed by chemical mechanical polishing. The wafer is then covered with the phase change material and with the top electrode. The heater must dissipate a large power and sustain a large temperature gradient, thus high electrical resistivity and low thermal conductivity are required. Another possible PCM design is the so called line-cell. It is simply a lateral line of a phase-change material that connects two electrodes. An example of this kind of structure is reported in fig. 1.6 [Lan05].

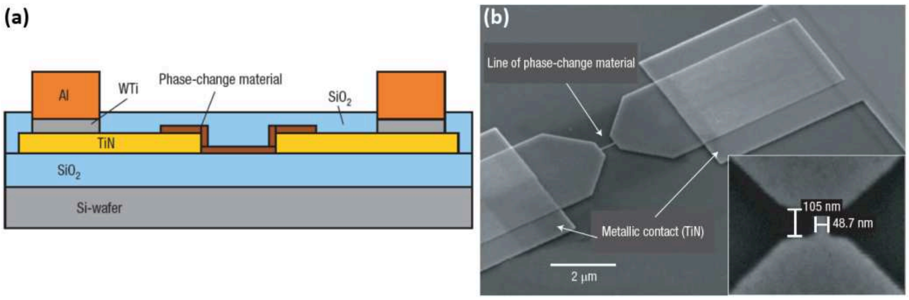

Figure 1.6 (a) Schematic cross-section of a line-cell with TiN contacts and Al bondpads. (b) Scanning electron micrograph of such a cell (length 500 nm, width 50 nm) made after structuring of the phase-change layer, which is done by electron-beam lithography. TiN contacts are structured by contact lithography. Inset, detail of similar cell with approximate dimensions 100 nm by 50 nm [Lan05].

The two electrodes are generally made by a TiN thin film (~50 nm). The phase change material is deposited by sputtering and then patterned by electron beam lithography and reactive ion etching. The active layer extends from the two electrodes and then shrinks to a narrow line structure in the middle between the two electrodes. The phase change material is contacted by WTi/Al pads for electrical testing. SiO_2 is subsequently deposited on the wafer to protect the structure. Many studies are reported in the literature that suggest different architectures trying to reduce the size and the power consumption of the devices. On the other hand high performance, cyclability and data retention must be preserved. It's difficult to find an equilibrium between the different demands [Bur10] [Ter09].

1.2 Properties of the phase change materials

In this paragraph, we summarize the requirements for storage applications that phase change materials meet. Optimal phase-change materials must provide a compromise of numerous, sometimes conflicting demands:

- In order to distinguish between the phases, their reflectivity and conductivity must differ significantly.
- Under proper conditions crystallization has to occur on a nanosecond timescale to obtain high write/erase rate.
- The amorphous phase must be stable at room temperature to ensure good data retention. It's known that amorphous bit must remain stable for ten years at room temperature.
- Simple composition and insensitivity to small variation of stoichiometry is preferred to ensure scalability on a nanometer scale. A good chemical stability is also required. Electromigration, relaxation and interaction with metallic contacts reduce indeed the lifetime of the electronic devices (10^6 cycles are required).
- Nonlinear electrical behavior in the amorphous phase and reasonably high resistivity in the crystalline one are required to minimize the power consumption.

1.2.1 Optical and electrical contrast

In figure 1.7 the optical constants n and k of the amorphous, rocksalt, and hexagonal phases of $Ge_2Sb_2Te_5$, the most investigated and prominent phase change alloy [Rao09], are shown. The laser wavelengths used for rewritable CDs, DVDs, and Blu-ray discs are also indicated. As we stressed before, the large change of refractive indices associated to the phase transitions allows to distinguish different logic states: for normal incidence at an air-material boundary the reflectivity at λ=405 nm increases from 49% to 67% during the transition from the amorphous to the metastable rocksalt structure, the two phases involved in the reset/set operations. The absorption length is then smaller in the crystalline phase rather than in the amorphous one (e.g. 12nm and 24nm at λ=633nm, respectively). In section 1.3.4 the motivation of this optical contrast will be discussed in detail.

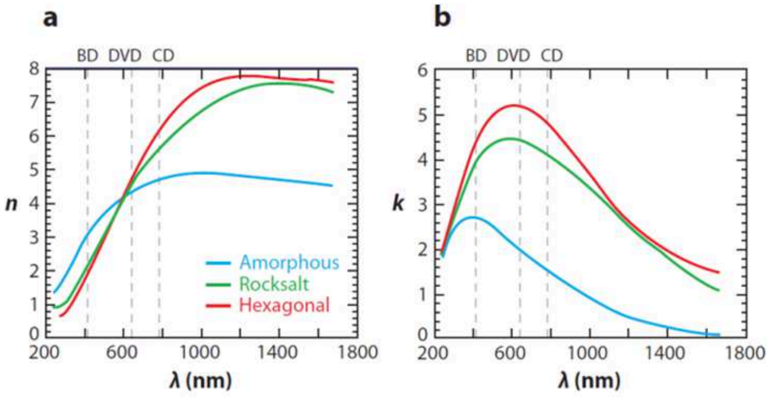

Figure 1.7 Optical constants (a) n and (b) k of the amorphous, rocksalt, and hexagonal phases of $Ge_2Sb_2Te_5$. The laser wavelength used for rewritable CDs, DVDs, and Blu-ray discs are marked [Rao09].

As underlined before, the functioning of the electronic devices is based on the change of resistivity observed during the phase transitions. Figure 1.8 show the resistivity as a function of temperature of several as-deposited phase change materials [Rao09]. Starting at room temperature, the films are heated at a constant rate; the resistivity smoothly decreases because the amorphous phase is semiconducting. With the onset of crystallization, the resistivity suddenly drops by several orders of magnitude. The resistivity change proceeds within a narrow temperature window in one single step allowing to determine the crystallization temperature (T_{xst}) of the specific alloy.

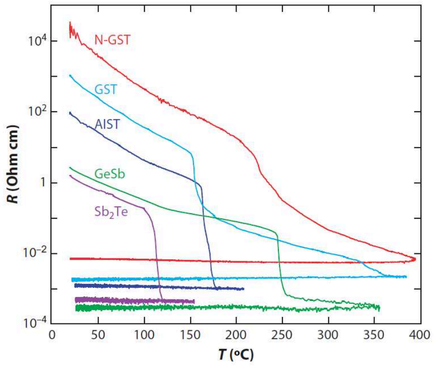

Figure 1.8 Resistivity as a function of temperature of several as-deposited,50 nm thick, phase change materials: $Ge_2Sb_2Te_5$ (GST), nitrogen doped GST (N-GST), $Ge_{15}Sb_{85}$ (GeSb), Sb_2Te, and Ag- and In-doped Sb_2Te (AIST). A huge reduction of resistivity occurs during the crystallization process.

As we will stress below, in many cases crystalline phase change materials are degenerate semiconductor, that is, the Fermi energy lies within the valence band, resulting in metal-like behavior and thus a $d\rho/dT>0$. It must be noted that GST shows a gradual reduction of resistivity during the crystallization process. This behavior is correlated to the presence of two distinct crystalline phases: a metastable rocksalt structure (T_{xst}≈150°C) and a stable hexagonal one (T_{xst}≈300°C) [Yam91].

1.2.2 Ultra-rapid crystallization

The crucial characteristic to guarantee the high performance of a phase change memory is the switching speed between the two distinct phases. Crystallization of the amorphous regions is the slowest process and hence will determine the maximum speed. A static tester is the instrument required to obtain this kind of information. Static testing is optical recording on a stationary sample: a single bit of information on the active layer of the optical recording medium can be read, written and erased. The changes in reflectivity to pulses from a focused laser beam is measured. By varying the power and length of the pulse, it can be studied when the phase-change material crystallizes or amorphizes. The minimum time to crystallize an amorphous area, independent of laser power, is called the complete erasure time and is characteristic for the crystallization speed of a material. Figure 1.9(a) shows an example of such an optical tester measurement in terms of a power-time-effect diagram [Sal08].

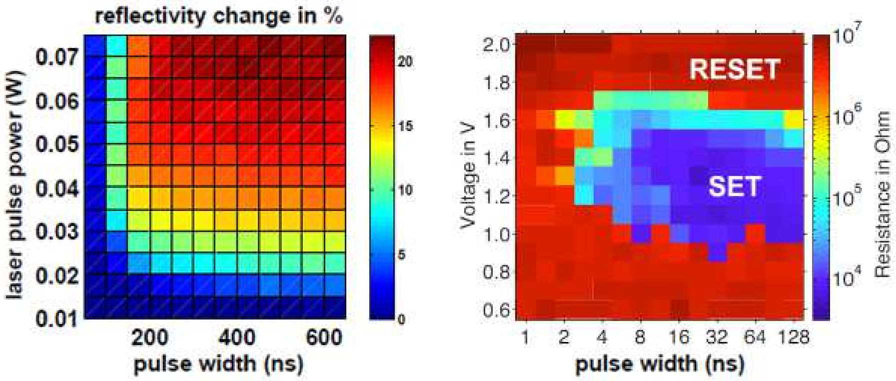

Figure 1.9 (a)Power-time-effect diagram for optical characterization of the crystallization behavior of an as-deposited amorphous $Ge_2Sb_2Te_5$ film deposited on silicon. Crystallization is detected by the increase in reflectivity after laser irradiation (i.e. red squares) [Sal08]. (b) Resistance of GeTe memory cells after application of set pulses with different amplitude and length, each starting from the amorphous reset state. The color of each data point represents the cell resistance after the test pulse. For pulses longer than 4 ns a broad crystallization window opens between 1.0 and 1.5 V [Bru09].

A laser pulse power of about 50 mW applied for only 150 ns leads to crystallization of the illuminated spot as evidenced by the pronounced enhancement in reflectivity. These data refer to an as deposited amorphous $Ge_2Sb_2Te_5$ thin film. Faster crystallization is reported in amorphous samples prepared by the quenching of the liquid phase. A similar characterization of electronic devices is also achievable using an electric tester. For this analysis, a fast pulse generator and an oscilloscope are combined with a made contact board. Figure 1.9(b) reports the results of [Bru09]. Here, crystallization, evidenced by the pronounced reduction of resistivity, can be triggered by applying pulses as short as only about 5ns. Data refers to the resistance of GeTe memory cells after application of set pulses, each starting from the amorphous reset state.

1.2.3 Amorphous phase stability

As we discussed before, to ensure good data retention, fast crystallization must be coupled with thermal stability at ambient temperature. Measurements of the crystallization time as a function of temperature have been largely reported in the literature to estimate the stability of the amorphous phase of several phase change materials. Figure 1.10(a) shows the reflectivity signal during isothermal annealing at different temperatures of as-deposited $Ge_2Sb_2Te_5$ thin films (50nm) [Deb08].

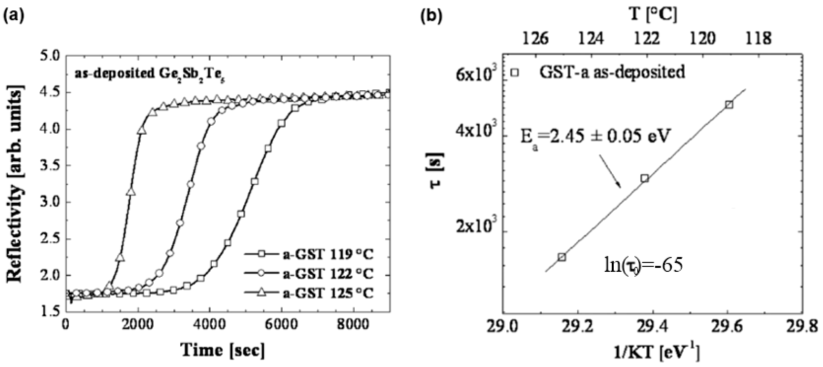

Figure 1.10 **(a) Reflectivity versus annealing time of as-deposited $Ge_2Sb_2Te_5$ thin films (b) Plot of the characteristic times τ, determined by the maximum of the first derivative of the reflectivity versus time curves, as a function of the reciprocal of temperature [Deb08].**

The zero of the time scale is the time at which the set point is reached. For the as-deposited amorphous film, a reflectivity plateau, which corresponds to the incubation time to reach a steady state nucleation rate, can be observed. After this transient, the reflectivity increases abruptly up to a saturation value at which the formed phase is polycrystalline face-centered-cubic (i.e. rocksalt).The crystallization time (τ) is experimentally defined by the maximum in the first derivative of the reflectivity versus time curve. This physical quantity is temperature (T) dependent by an exponential law according to the equation

$$\tau(T) = \tau_0 exp\left(\frac{E_A}{k_B T}\right),$$

where τ_0 is a constant pre-exponential factor and k_B is the Boltzmann constant. The values of E_A and τ_0 have been extracted by the linear fit of the ln(τ) as function of $1/k_BT$, the plot is shown in fig.1.10(b). Applying this simple Arrhenius law it is possible to state that the amorphous GST is stable at room temperature for a time τ(25°C)≈10^5 years.

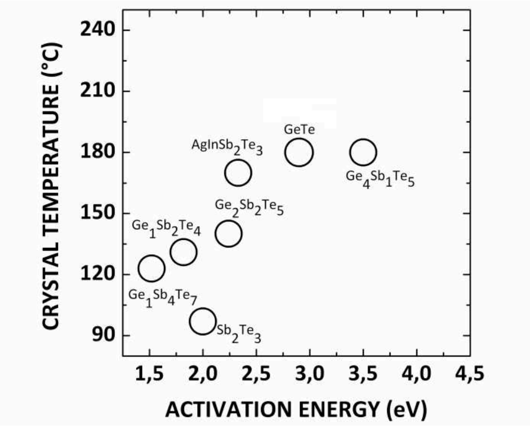

Figure 1.11 **Crystallization temperature and activation energy of the crystallization time of several phase change materials. It's clear that the higher is the amount of germanium in the alloy the higher is the crystallization temperature.**

It is important to note that in many applications the operating temperature of a device is higher than 25°C and under these conditions the crystallization time can be much lower (e.g. τ(70°C)≈20 years). Moreover, the crystallization time of an amorphous mark embedded in a crystalline environment could be further reduced. This is unfortunately the operating condition of a phase change memory, fig. 1.5(c). The higher is the crystallization temperature of a phase change material, the more are the possible applications. This is the motivation for a new interest on the study of the more stable GeTe alloys with respect to GeSbTe materials. Figure 1.11 summarizes the crystallization temperature and the activation energy of the crystallization time of several phase change materials [Yam91]. A higher amount of germanium in the alloy is generally coupled with a higher crystallization temperature. This behavior can be understood taking into account the energy of the different bonds broken and created during the crystallization process [Crc87].

1.2.4 Eutectic vs single phase materials

The higher crystallization temperature of Ge-rich chalcogenide is not necessary coupled with better phase change properties. Sensitivity to compositional variations and chemical stability have to be taken into account for the application in storage devices. From the early 70’s through the 80’s Te-based eutectic compositions with low melting temperature were actively investigated. Based on the typical eutectic systems such as Te-Ge and Te-Sb, various studies were carried out. These attempts did not reach the final goal for practical applications because the Te based eutectic alloys (e.g. $Ge_{15}Te_{85}$) exhibited some merits coupled with essential and impassable demerits. The ability to easily form the amorphous phase is a large merit due to their very low melting temperatures and their flexible coil like structures [Yam08]. On the other hand solidification from the eutectic will cause phase separation (see fig.1.12) [Han58]. If the different phases have largely different thermal properties, such as melting points and viscosities, significant variation of recording power conditions, increased noise, and limited cycle numbers are expected. Moreover in the case of the eutectic compositions, the crystallization doesn’t proceed so fast since the temperature of the liquid is quite low and then the atomic mobility is small. The last demerit is the low crystallization temperature. According to [Sak69] the glass transition temperature T_g of materials corresponds to 2/3 of their melting temperature, in Kelvin. It means that T_g (which is a lower limit for the crystallization temperature) of these materials is essentially low; therefore the thermal stability of the amorphous phase will be insufficient. To overcome these difficulties the attention was moved to single phase materials, typically stoichiometric compounds, that possess some advantages such as rapid crystallization and higher stability while they have only one demerit. Anyway, the problem of difficult amorphization can be solved by the design of the device structure, such as a multi-layered stacking structure, producing very large cooling rates (10^7-10^{10} K/s).

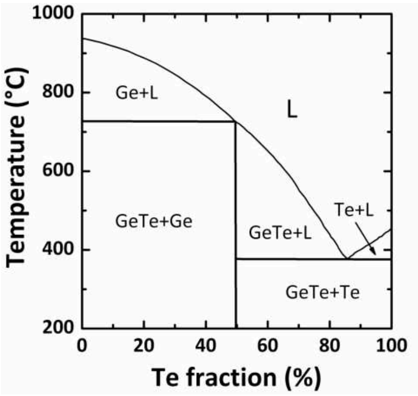

Figure 1.12 Phase diagram of the binary Ge-Te system, obtained from [Che86]. The eutectic composition $Ge_{15}Te_{85}$ shows a low melting temperature coupled with phase separation in the solid phase. Stoichiometric GeTe is a single phase material but melts at higher temperature [Han58].

Stoichiometric GeTe, in 1986, was the first single phase material that exhibits better phase change properties with respect to the corresponding eutectic alloy: the crystallization time by laser irradiation decreases from 100µs to 50ns whereas the crystallization temperature increases from 160°C to 180°C [Che86]. Unfortunately also in the case of single phase alloy, like GeTe, phase separation can locally occur during erase/write cycles affecting the life time of the electronic devices. This behavior can be due to non homogeneous deposition processes, electromigration phenomena or interaction with metallic contacts. Insensitivity to small variation of stoichiometry and low chemical reactivity are then important requirements. Unfortunately an universal scheme able to predict these features is not achievable.

1.2.5 Current-Voltage characteristic

The functioning of electronic phase change memories is based on the peculiar nonlinear electrical behavior that the amorphous phase shows under moderate applied voltage (E~V/µm). Figure 1.13 reports the characteristic current-voltage curve of a typical phase change alloy [Wut07]. Applying a voltage up to 0.7 V on the amorphous material a marginal current flows due to the high resistance of this state. Above 0.7 V, the resistance drops and the current therefore increases greatly (threshold switching).

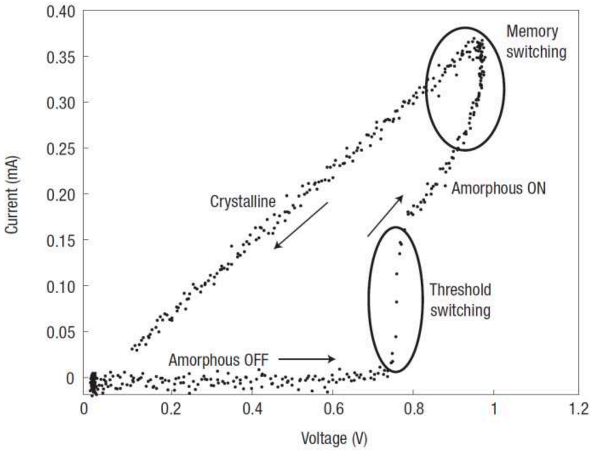

Figure 1.13 Current–voltage characteristics of a typical phase-change material. For small electric fields the curves of the crystalline and of the amorphous phase differ significantly. If a critical voltage (E~V/µm) is exceeded the amorphous phase suddenly becomes much more conductive. This effect, called threshold switching, enables sufficient joule heating for crystallization at moderate voltages [Wut07].

Now heat is dissipated in the amorphous state, leading to the formation of the crystalline phase (memory switching), which is characterized by a much lower resistance and hence high current. It's important to note that this threshold switching is a phenomenon specific to the amorphous phase and is not necessary coupled with structural phase transition. The electrical conductivity of the amorphous phase, for small electric fields, exhibits a thermally activated transport behavior [Len08],

$$\vartheta(T) = \vartheta_0 exp\left(-\frac{E_c}{k_B T}\right)$$

where the activation energy is generally half of the optical bandgap (~0.7eV). Controversial results came out from Seebeck and Hall measurements: in the first case p-type conduction was measured, whereas n-type was deduced in the second case [Bai06][Bai06b]. This is interpreted as an indication for conduction via hopping of small polarons (i.e., localized charges that trap themselves by distorting the surrounding atoms) [Iel07]. The presence of other localized states, closed to the extended band, can't be excluded and contributes to the reduction of the carriers mobility. The physical model for conduction in the amorphous phase is Poole-Frenkel conduction. The electrons are generally trapped in localized states. Occasionally, random thermal fluctuations will give sufficient energy to get out of its localized state, and move to the conduction band. The electron can then move through the material, for a brief amount of time, before relaxing into another localized state. Electrons have to overcome a potential barrier at zero voltage, which can be linearly lowered by an applied voltage V [Iel08]. The current can be calculated by the following equation

$$I = 2qAN_T \frac{\Delta z}{\tau_0} \exp\left(-\frac{E_C - E_F}{k_B T}\right) sinh\left(\frac{qV}{k_B T}\frac{\Delta z}{2u_a}\right)$$

where q is the electron charge, A is the area of contact of the active volume, u_a is the thickness of the amorphous layer, N_T is the total concentration of traps contributing to the electron current, from the Fermi level E_F to the mobility edge, τ_0 is the characteristic escape time of the electron, E_c is the mobility edge at the conduction band and Δz the distance between traps. As we discussed before, applying a voltage higher than a threshold value a characteristic decrease of resistivity is observed. Several different interpretation of this phenomenon are reported in the literature [Emi06][Iel08b][Rad08]. According to the Poole-Frenkel model, the electric field increases the probability of a carrier that occupies one trap to get to another one nearby. At low fields, this requires extended states. At the threshold field, however, also direct tunneling becomes possible, leading to the conductivity increase. The energy gain process was modeled as a tunneling injection mechanism from deep states, close to E_F, to high-energy (shallow) states close to the conduction band E_c.

So far we have discussed the peculiar properties of phase change materials that allow their use as active layer in data storage devices. Presumably, the significant differences between the amorphous and the crystalline phase are related to substantial differences in the atomic arrangement. Hence, we will review now the structures of crystalline and amorphous phase change materials relating them to the bonding mechanism. This comparison will allow us to identify the origin of this unique properties portfolio.

1.3 Structure of the crystalline phase

We discuss now the crystalline structure of phase change materials, focusing again on the prototype alloys belonging to the GeTe-Sb_2Te_3 pseudobinary line. The atomic structure of these materials exhibits generic features and structural motifs, which are uncommon. These properties are related to a unique bonding mechanism, which will be discussed in the section 1.3.4. The two fundamental alloys GeTe and GeSbTe are described below.

1.3.1 Long range order

The bulk of structural data on phase change materials has been obtained using X-ray diffraction. Unfortunately, the crystalline phases of these alloys are generally available only in metastable films a few tens of nanometers thick. An unambiguous identification of structural features is then difficult. This fact in conjunction with the presence of significant site disorder, makes the need for complementary techniques such as Extended X-ray Absorption Fine Structure (EXAFS) spectroscopy, neutron diffraction or transmission electron microscopy. Anyway we start the discussion analyzing X-ray data relative to GeTe and GeSbTe crystalline phases [Non00]. GeTe, at room temperature, exhibits a distorted NaCl type structure (rhombohedral, space group R3m) stretched in the <111> direction. Lattice constant and the interaxial angle are a=4.2810 Å and α=58.358°, respectively.

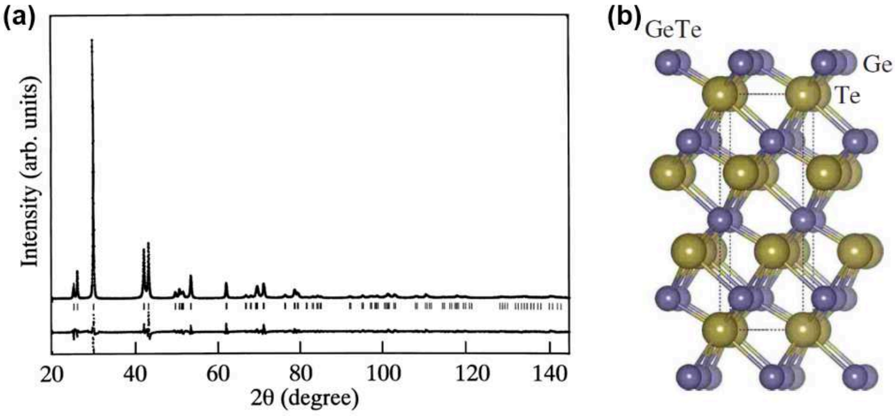

Figure 1.14 (a) Powder XRD pattern of rhombohedral crystalline GeTe [Non00]. (b) Crystal structure of bulk GeTe. The Ge (small balls) and Te (large balls) atoms are labeled, while the dashed line indicate the conventional hexagonal lattice [Das08].

The coordinate of Te (0.521, 0.521, 0.521) was found to deviate significantly from 0.5. It means that there are two different Ge-Te bonding lengths (2.84Å and 3.16Å). Locally, each atom is nominally octahedrally coordinated with three short bonds and three longer bonds. X-Ray data and a schematic model of this structure are shown in fig.1.14 [DaS08]. The quantum mechanical origin of the distortion has been suggested to be a form of Peierls distortion (a spontaneous lower of symmetry distortion that lowers the free energy of the system) and to be general to Te-based chalcogenides (sect. 1.3.2). GeTe is also an example of a material that undergoes a displacive ferroelectric transition, above ~430°C, which leads to a temperature activated lifting of the Peierls distortion with a transition to the cubic phase [Len08].

We can now turn our attention to the pseudobinary tie-line between GeTe and Sb_2Te_3 (fig. 1.2). Starting from the 1990s, it was suggested that the three stoichiometric phases $Ge_1Sb_4Te_7$, $Ge_1Sb_2Te_4$ and $Ge_2Sb_2Te_5$, would all be possible candidates for optical data storage. However, the Ge-rich compositions were found to exhibit the greater stability in the amorphous to crystalline transition and so they were preferred. X-ray powder diffraction investigation of the average structure of $Ge_1Sb_2Te_4$ and $Ge_2Sb_2Te_5$, established that they crystallize in the rocksalt structure.

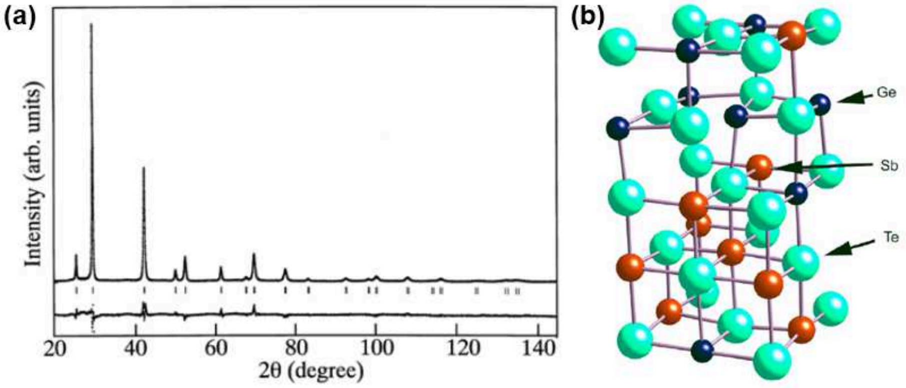

Figure 1.15 **(a) Powder XRD pattern of face centered cubic crystalline $Ge_2Sb_2Te_5$ [Non00]. (b) Crystal structure of bulk $Ge_2Sb_2Te_5$. The Ge (small balls), Sb (medium balls) and Te (large balls) atoms are labeled [Sha05].**

It can be visualized as consisting of two interpenetrating fcc sub lattices, one located at the origin and the other at (1/4, 1/4, 1/4). Rietveld analysis suggested that Te fully occupies one fcc sublattice while Ge and Sb are randomly distributed on the other with either 25% ($Ge_1Sb_2Te_4$) or 20% ($Ge_2Sb_2Te_5$) vacancies. EXAFS analysis confirms the presence of vacancies (10%) also in the rhombohedral GeTe crystalline structure. X-Ray data and a schematic model of the $Ge_2Sb_2Te_5$ metastable structure are shown in fig.1.15 [Non00][Sha05]. Lattice constant and the interaxial angle are a=6.0117Å and α=90.000°, space group $Fm\bar{3}m$. Each atom is again octahedrally coordinated. It must be noted that also GeSbTe exhibits two possible crystalline structures: a metastable face centered cubic (described above) and a stable hexagonal one with each atom type, Ge, Sb and Te possessing a different stacking sequence [Par06].

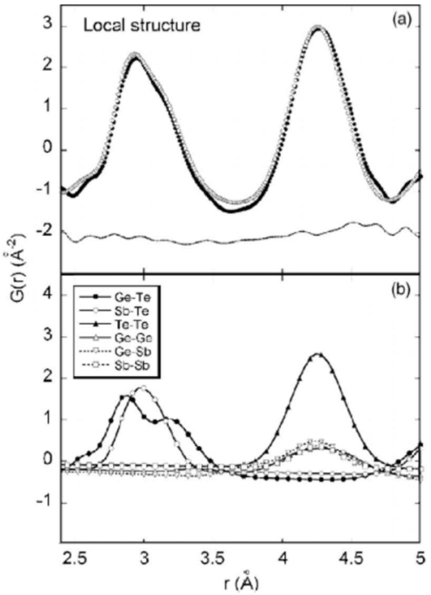

Figure 1.16 **(a)Observed (closed circle), calculated (open circle), and difference (small closed circle) pair distribution function profiles of rocksalt crystalline $Ge_2Sb_2Te_5$. Fitted G(r) components for local structure in (b) are shown in (c), indicating large displacement of germanium atoms.**

For example, in the case of $Ge_2Sb_2Te_5$, the stable phase belongs to the space group $p\bar{3}ml$, (a=4.22Å, c=16.96Å) and is composed by nine cyclic layers Te–Sb–Te–Ge–Te–Te–Ge–Te–Sb.

More recent diffraction measurements suggested, however, a disordered phase with Sb and Ge randomly occupying the same layer [Mat04]. We focused our attention to the metastable rocksalt structure since the transition between this phase and the amorphous one is used for memory storage applications. The fact that X-ray diffraction of a site disordered system can only see the average structure obscured the possible presence of Peierls like distortion in these metastable alloys. To overcome this difficulty Shamoto *et al.* performed atomic pair distribution function measurements coupled with conventional Retvield neutron diffraction analysis on fcc crystalline $Ge_2Sb_2Te_5$ [Sha05]. In the first case local order is probed whereas in the second one average information are obtained. Figure 1.16 shows the local order analysis. Pair distribution function, G(r), was calculated by the Fourier transformation of the total structure function. Fitted G(r) components for local structure in (a) are shown in (b), indicating large displacement of germanium atoms. If the average crystal structure was intrinsic, the first nearest neighbor peak in the G(r) should be a broad simple Gaussian. The observed first nearest neighbor peak had instead a complex structure. Since one site is entirely occupied by Te, only Ge–Te and Sb–Te atomic correlations appear in the first peak. To fit the data a periodic nonsymmetric cubic unit cell was fixed with one Te atom at the origin. Other parameters were chosen according to the X-ray diffraction results previously described. As a whole, large displacement of Ge atoms is characteristic in the crystal structure. Ge–Te bond lengths of 3.03(22)Å have much wider distribution than Sb–Te bond lengths of 3.02(10)Å, where numbers in parentheses are estimated standard deviations of the last digits. The wide and split Ge–Te correlation peak would be due again to Peierls distortion.

In conclusion, we can affirm that both vacancies and Peierls-like lattice distortions are structural motifs of crystalline phase change materials.

1.3.2 Vacancies and distortions

Since the distortions of the crystalline lattice are of utmost importance for phase change materials, we shall briefly introduce the underlying concept. Here we adopt the common approach to explain the concept for a crystalline system, the results on the shifts in the density of states and the local distortions can be transferred to non-crystalline systems as well [Wut07b]. As a prerequisite, dominant p-type bonding (equivalent to the absence of hybridization between s- and p- states) is assumed, leaving us first with a (hypothetic) highly symmetric six-fold coordination. This is the case of metastable crystalline GeTe and GeSbTe alloys. To simplify matters, we assume a one-dimensional chain of equally spaced atoms with a simple parabolic band structure as shown in fig. 1.17 [Len10]. Depending on the number of electrons or equivalently on the position of the Fermi wavevector k_F (located within the Brillouin zone) this chain is unstable against a periodic distortion. This distortion introduces a Fourier component of the potential at this wavevector, V_{k_f} , and then leads to the opening of a gap of size $2V_{k_f}$ and thus a decrease of the energy of the occupied states. The Brillouin zone shrinks according to the periodicity of the distortion pattern.

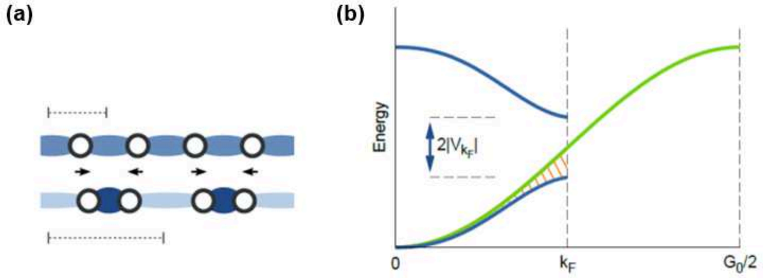

Figure 1.17 **(a) The model of a Peierls distortion is shown for a one dimensional atomic chain with a half filled band (b) By the periodic distortion a potential is introduced leading the opening of an energy gap at the Fermi level. Consequently a decrease of the energy of the occupied states (hatched) is obtained. This energy gain is the driving force of the distortion [Len10].**

With this model, we can understand the coordination of GeTe, for instance, if we assume that each dimension may be treated separately. Then, we have three p-valence electrons per atom out of a maximum of six, one per dimension. Thus, the initially equally long bonds in one dimension split into a short and a long bond. So in three dimensions, three short and three long bonds per atom result. A detailed calculation of the energy gain obtained by the introduction of distortions and vacancies in the crystalline phase of GeSbTe alloys has been proposed by Wuttig *et al.* and is reported in fig.1.18 [Wut07b]. The energy of the system lowers on removing Ge atoms from the $Ge_2Sb_2Te_4$ composition, fig.1.18(a). It is even favorable to remove several Ge atoms up to a maximum of 12.5% Ge vacancies. The composition $Ge_{1.5}Sb_2Te_4$ is the most favorable. A second point is that lattice distortions also play a crucial role, blue stars in fig. 1.18(a). They lead to a considerable further reduction in energy. Interestingly, the energy gain on the lattice distortions increases with increasing number of Ge vacancies and the maximum gain is reached again at 12.5% vacancies concentration. In subsequent calculations, the change in energy on removal of Sb atoms was also computed.

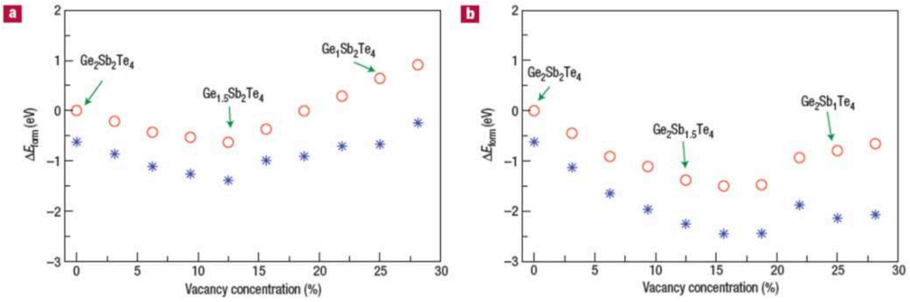

Figure 1.18 Formation energies of Ge (a) and Sb (b) vacancies for different vacancies concentration (open red circles). A negative value of the formation energy implies that vacancy creation is energetically favorable. The distortion leads to a further energy gain (blue stars) [Wut07b].

The resulting data are shown in fig.1.18(b). Quite similar to the case of Ge removal, the total energy of the $Ge_2Sb_2Te_4$ phase is also lowered by the removal of Sb atoms. The energy further lowers on relaxation. Removal of Te atoms increases the energy. These findings clearly needs an explanation. The composition $Ge_2Sb_2Te_4$ is characterized by both massively antibonding Ge–Te and Sb–Te interactions close to the Fermi level. This is related to the presence of *p-bonding* coupled with octahedral coordination. Thus, the composition $Ge_2Sb_2Te_4$ is characterized by a too high valence-electron concentration (VEC), which must be lowered to achieve better stability. The decrease of the VEC by including vacancies results then in a lower charge-carrier density. $Ge_2Sb_2Te_4$ exhibits a high density of antibonding states at the Fermi level. In $Ge_{1.5}Sb_2Te_4$, this density is significantly lower, whereas for $Ge_1Sb_2Te_4$ it decreases even further. A simple chemical argument explains why these excess electrons cannot be removed by expelling tellurium atoms. It is the 'anionic' Te atom (with a high absolute electronegativity χ=5.49 eV) whose orbital contributions are dominant in the lower-lying valence band, whereas the 'cationic' Ge and Sb atoms (χ = 4.6 and 4.85 eV, respectively) mix mostly in the frontier bands, that is, where the too high VEC must be lowered. On structural relaxation (blue stars in fig.1.18), the bandgap between the valence and conduction band increases significantly. Numerical energy partitioning contributions evidences that, due to the Peierls instability, it is mostly the Te substructure that gains total energy on structural relaxation. Elemental Te has four valence p electrons but is only twofold coordinated. One p-orbital can be described as a nonbonding orbital filled with two electrons (lone pair). Germanium has one completely empty p-orbital. This is due to the fact that its 2p electrons occupy one p-orbital each according to Hund's rule, whereas the third orbital remains unoccupied. In this simple scheme, adding germanium to an Sb–Te alloy therefore reduces the number of these non-bonding states and promotes an octahedral arrangement by the formation of *p*-bonds. Thus, adding Ge to $Ge_1Sb_2Te_4$, on one side, reduces the energy gain by the Peierls distortion since supports the formation of linear atomic chains but it is energetically favorable, on the other side, as it reduces the number of non-bonding Te states (see sect.1.3.4). Therefore, just the addition of a small amount of germanium to $Ge_1Sb_2Te_4$ is favorable. Along the $Ge_2Sb_2Te_4$–$Ge_2Sb_1Te_4$ series analogous arguments apply. As Sb has more p electrons than Ge, however, it is less effective in reducing the number of Te lone pairs, which thereby leads to a more pronounced occupation of antibonding states.

1.3.3 Short range order

The property contrast between the amorphous and the crystalline state of phase change materials was attributed to a different short range order between these two phases. This interpretation was proposed by Kolobov *et al.* on the basis of EXAFS analyses performed on $Ge_2Sb_2Te_5$ thin films but a similar approach was suggested also for stoichiometric GeTe [Kol04][Kol03]. They stated that the main structural rearrangement taking place upon crystallization is a flip of germanium from tetrahedral to octahedral sites. The EXAFS data of the different atomic edges are shown in fig. 1.19 [Kol04]. For the crystalline phase they used the rocksalt structure as the starting structural model for data fitting. The bond lengths (Ge-Te=2.83±0.01Å), Sb-Te=2.91±0.01Å) were in good agreement with X-ray results (~3.0±0.3Å). Unexpectedly, they found that the overall fit intensity was significantly less than predicted.

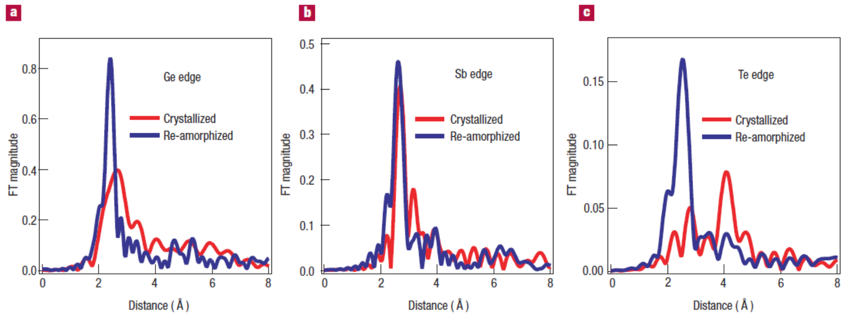

Figure 1.19 **EXAFS spectra for crystallized and amorphized $Ge_2Sb_2Te_5$ samples. The spectra refer to the K-edges of: Ge (a), Sb (b) and Te (c). On amorphization the bonds become shorter (as shown by shifts in the peak positions) and more locally ordered (as shown by increases in the peak amplitudes and concurrent decreases in the peak widths) [Kol04].**

It is known that the amplitude of the Fourier transform peaks is proportional to the abundance of the corresponding bonds (i.e., coordination number). On the other hand the EXAFS process is affected by atomic disorder that can be due to a structural configuration or to the atomic vibrations. In this case it is easy to believe that this low intensity is correlated to the “structural disorder” of the crystalline phase as described in the previous sections. We now turn to the amorphous state. Ge-Te and Sb-Te bonds get shorter (2.61 Å and 2.85 Å, respectively) and “stronger” as shown by the blue lines of fig. 1.19. At the same time, the Te second-neighbour peak becomes considerably weaker. The mean-square relative displacements value decreases from 0.02 $Å^2$ in the crystalline state to 0.008 $Å^2$ in the amorphous state and then the average deviation of the bond length is expected to follow the same trend. This behavior is also coupled with a lower coordination of the amorphous phase with respect to the crystalline one (see sect. 1.4.1). As previously anticipated, on the basis of the different Ge-Te bond length between amorphous and crystalline state, Kolobov suggested that the main difference between the two phases is the local order around Ge atoms that could be alternatively tetrahedral (i.e., sp^3 hybridization) or octahedral coordinated (i.e., *p* bonding). Unfortunately, this is not the case. First of all, the presence of homopolar Ge-Ge or Ge-Sb bonds in the amorphous phase was detected by subsequent EXAFS analyses [Bak06][Jov08] and predicted by several theoretical calculations [Car07][Ako07] (see sect. 1.4.1). The Kolobov model instead admits only Ge-Te bonds. Moreover extensive theoretical simulations have shown that, while tetrahedrally coordinated germanium atoms are present, they represent only a minority, making up only roughly one third of all germanium atoms in the amorphous phase. A definitive rejection of this model is due to the X-ray photoemission spectroscopy results presented by Kim *et al*. [Kim07]. In the case of the umbrella flip model of Kolobov, the valence-band density of states of the amorphous phase should be greatly different from that of the crystalline phase due to the sp^3 bond formation, and also due to the inevitably introduced broken bonds in the amorphous phase. It is not the case in all the studied GeTe-Sb_2Te_3 alloys. The measured valence-band spectra of the crystalline phases, shown in fig.1.20(a), exhibit three-peak structure that is maintained during the crystalline to amorphous phase transition, indicating that no drastic changes occur in the s^2p^3 valence configuration, fig. 1.20(b). We can now focus our attention on the details of fig. 1.20(a). Each spectrum of crystalline $(GeTe)_{1-x}(Sb_2Te_3)_x$ shows the structure expected according to the previous discussions. The two peaks of deep energy level are due to the *s* band, and the peak near the valence band maximum is due to the *p* band. The three-peak structure in the present valence-band spectra can be indexed as follows. The peak at the lowest binding energy (peak A) is due to the Ge 4*p*, Sb 5*p*, and Te 5*p* orbitals. The second peak (peak B) between 6 and 10eV is due to the Ge 4*s* and Sb 5*s* orbitals, and the last peak C at 12eV is due to the Te 5*s* orbital. There is a main variation with increasing *x*. Peak B, which is located at 8.3 eV (B1) as a single peak in the GeTe, reveals a different structure at 9.4 eV (B2) with the incorporation of Sb. The B1 peak becomes weak and the B2 peak becomes intense with increasing *x*.

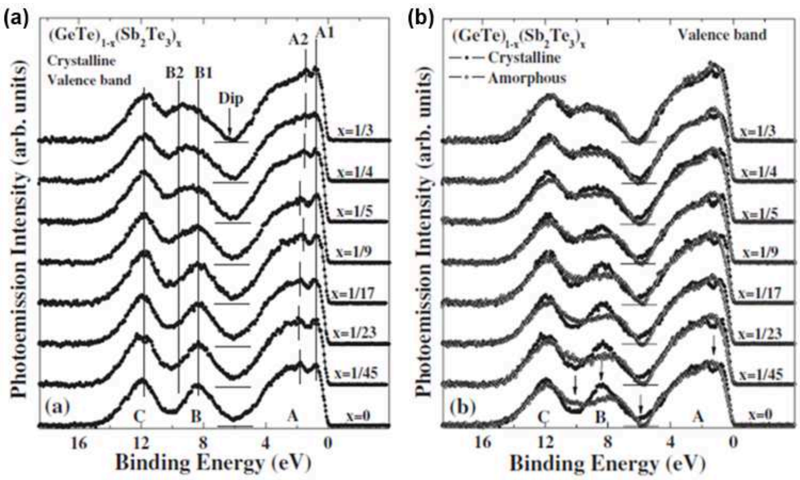

Figure 1.20 (a) Valence-band spectra of crystalline $(GeTe)_{1-x}(Sb_2Te_3)_x$ alloys. (b) Comparison between the valence-band spectra of the amorphous (open circles) and of the crystalline (closed circles) phases [Kim07].

This behavior well reflect the content ratio between Sb and Ge in $(GeTe)_{1-x}(Sb_2Te_3)_x$ and reveals the different contributions to the total peak B intensity. Peak A and C don't show a distinct variation with changing composition. We can now discuss the electrical properties of crystalline phase change materials on the basis of the valance band description that we have just reported. It is known that the concentration of charge carriers in the crystalline phase is particularly high, reaching values on the order of $\sim 1\times10^{20}$ cm^{-3}. This is not a consequence of the small gap (~0.5eV) and thermal excitation, but induced by a pronounced shift of the Fermi-level towards or even into the valence bands due to high defects concentration. The situation is summarized in fig.1.21 [Len10]. The states around the Fermi-level and their nature dominate the electrical behavior of phase-change materials. Depending on the position of the Fermi level, these defects are (negatively) charged or neutral. With increasing temperature, the number of these defects increases.

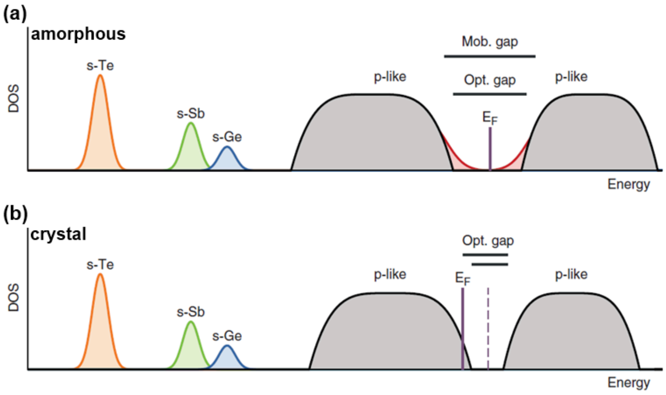

Figure 1.21 The schematic electronic densities of states of Ge:Sb:Te-materials in the amorphous (a) and crystalline (b) phase are compared. The optical gap of the crystalline phase is narrower than in the amorphous. Here, the Fermi level is stuck in the mid gap and localized state are present within the gap (red area). In the crystalline state, the Fermi level is typically shifted towards or even into the valence band [Len10].

Concurrently, the Fermi-level is dragged towards the valence band. Also in the amorphous phase, the position of the Fermi-level and the presence of defect states within the optical (or the mobility) gap have intensively been addressed. In this case the Fermi-level is found in the mid gap. More specifically, the robustness of the position of the Fermi-level has been noted. Therefore, a microscopic picture explaining the pinning of the Fermi level is desirable. The model of valence alternation pairs (VAP) was proposed [Adl80]. Here, the deviation from two-fold-coordination of chalcogen-atoms "C", namely threefold-coordination, creates a pair of acceptor-like and donor-like states, which thus pin the Fermi-level near mid gap. Anyway, no unique defect model is able to accurately describe the conduction in phase change materials and controversial experimental results are reported. The most accepted conduction mechanism in the amorphous phase was described in section 1.2.5.

At this point of the discussion is still not clear why the crystalline and the amorphous phase can simultaneously exhibit very different optical properties and a similar bonding arrangement. The answer is within the next section.

1.3.4 Resonant bonding

As stressed in the previous section, the amorphous and the crystalline state of phase change materials are characterized by a similar short range order. Just the bond lengths and the coordination number of the different atomic species show a clear variation. On the other hand the huge different optical properties need an explanation that can't be related to variations in the long range order. An interpretation of this peculiar behavior has been proposed by Shportko *et al.* [Shp08]. They have investigated the dielectric function ε(ω) of each phase by infrared spectroscopy and spectroscopic ellipsometry. Their study focused on the energy range above the highest phonon frequencies (30 meV) but below the optical gap of typically 0.75 eV. In this range, the dielectric function ε(ω) is governed by the electronic polarizability of the valence electrons, and probes the chemical bonding of the materials. Evidence of a large component of resonant bonding in the crystalline phase was found. The sample geometry shown in fig.1.22(a) was used to determine the dielectric function. Films of different stoichiometry were analyzed. The reflectance curves of the phase-change alloy $Ge_2Sb_1Te_4$ is shown in fig.1.22(b). The blue curves are for the as-deposited amorphous state and the red curves for the rocksalt crystalline film. There are three significant differences between the curves. First, the interference fringes extend to much higher photon energies for the amorphous than the crystalline phase, owing to the larger bandgap of the amorphous phase. Second, the reflectance maxima are lower in the crystalline phase, owing to subgap (Drude-like) absorption by free carriers. Third, and most important, is the pronounced difference in spacing of the reflectance minima. The spacing is about 40% smaller in the crystalline phase which implies that the refractive index (*n*) is 50% larger.

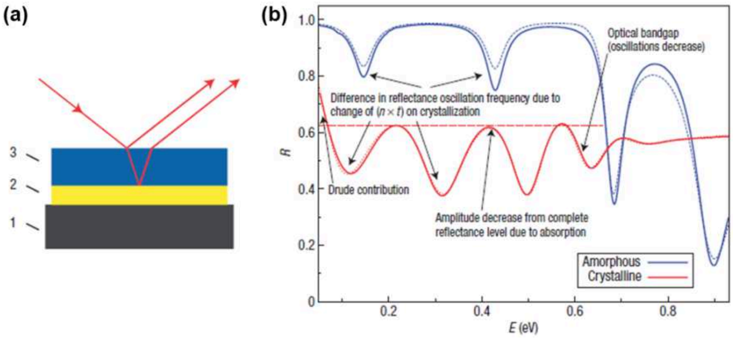

Figure 1.22 **(a) Sample investigated. 1: glass substrate, 2: Au layer, 3: semiconductor layer. (b) Infrared reflectance spectra of a $Ge_2Sb_1Te_4$ film. Blue: amorphous state, red: crystalline state. The contributions of different phase-change film properties to the reflectance curve are marked [Shp08].**

The reflectance spectra of all investigated phase-change materials show a similar effect; ε_∞ is much larger in their crystalline phase. ε_∞ is the low energy limit of $\varepsilon(\omega)$ in the range studied here and, neglecting the absorption, $n \approx \sqrt{\varepsilon}$. The excess of ε_∞ for the crystalline phase is significant and reaches values over 200% (fig.1.23). This difference is a generic feature of phase change materials. The mechanism for this polarizability enhancement can be explained in terms of the difference in chemical bonding. The structure of crystalline Sb is a nice example. The Sb atom has a filled valence *s*-orbital, and its bonding occurs between the *p*-orbitals which each contain one electron. To first approximation, these form three independent chains of *p*-states along the *x*,*y* and *z* directions. This leads to a half-filled band with a zero bandgap at the Fermi energy. The situation in which a single *p*-band forms two bonds to the left and right (more than allowed by the 8-*N* rule) was called resonant bonding by Pauling [Pau39]. Each Sb atom has six nearest neighbours, but only three *p*-electrons to facilitate covalent bonding between adjacent Sb atoms. In reality, a superposition of the possible configurations is observed. The pronounced electron delocalization, which characterizes resonant bonding, leads to a significantly increased electronic polarizability. This phenomenon is one of the fingerprints of resonance bonding. The true crystal structure of Sb is not a simple cubic structure, but a rhombohedral structure, which can be described as a distorted cubic structure.

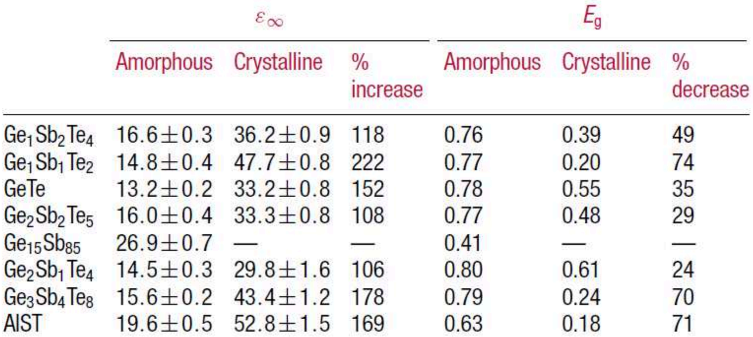

	ε_∞			E_g		
	Amorphous	Crystalline	% increase	Amorphous	Crystalline	% decrease
$Ge_1Sb_2Te_4$	16.6±0.3	36.2±0.9	118	0.76	0.39	49
$Ge_1Sb_1Te_2$	14.8±0.4	47.7±0.8	222	0.77	0.20	74
GeTe	13.2±0.2	33.2±0.8	152	0.78	0.55	35
$Ge_2Sb_2Te_5$	16.0±0.4	33.3±0.8	108	0.77	0.48	29
$Ge_{15}Sb_{85}$	26.9±0.7	—	—	0.41	—	—
$Ge_2Sb_1Te_4$	14.5±0.3	29.8±1.6	106	0.80	0.61	24
$Ge_3Sb_4Te_8$	15.6±0.2	43.4±1.2	178	0.79	0.24	70
AIST	19.6±0.5	52.8±1.5	169	0.63	0.18	71

Figure 1.23 Optical dielectric constants and energy gaps of several phase change materials in both the amorphous and the crystalline phase (absorption contribution subtracted) [Shp08].

As we described in section 1.3.2, the rocksalt structure is unstable with respect to a Peierls distortion, which forms alternative shorter and longer bonds along the atomic chains, lowers the free energy and opens up a gap at E_F. This distortion increases electron localization because the two different electron configurations are no longer energetically equivalent. Thus, resonance bonding is weakened by the Peierls-like distortion. As stressed before, the crystal structures of phase-change materials are all based on distorted cubic structures and all possess resonant bonding. It is therefore the cause of their anomalous high optical dielectric constants. An electron pair bond only requires the ordering of the nearest neighbours forming the bond. Resonant bonding, on the contrary, requires the second and higher neighbours to be aligned. In the amorphous state, this higher level of ordering is not possible, and so the alloy reverts to a simple more “covalent” structure, which requires a lower level of ordering. This emphasizes that the bonding between the phases differs not only in coordination numbers, as seen by EXAFS spectroscopy, but also in their medium range order. This is the origin of the optical contrast between the two phases. Tetrahedrally bonded covalent semiconductors such as Si, Ge, GaAs, GaN or $CuInS_2$ possess on average four valence electrons per atom. For this electron configuration, sp^3-hybridization and hence a tetrahedral atomic arrangement are more favorable. Therefore, for these systems, resonance bonding is impossible (3*p* electrons required), which also prohibits sufficient optical contrast.

1.4 Structure of the amorphous phase

The structure of the amorphous phases of phase-change materials has been largely studied by means of X-ray techniques (EXAFS) [Kol04][Bak06], neutron diffraction [Jov08] and molecular dynamics-simulations [Koh06] [Car07]. As pointed out in sect. 1.3.4, the amorphous phase of these materials generally represent a covalently bound network. The aim is then to reveal the coordination number and the bonding geometry of each atomic species. This allows to describe the amorphous phase in terms of the previously introduced concepts and aids the understanding of the transition kinetics between the amorphous and the crystalline phase on an atomistic level.

1.4.1 Short range order

A comparison of recent experimental studies reveals that despite its technological importance, the structure of amorphous chalcogenide is still debated. The following discussion is focused on the most investigated and promising phase change materials, i.e. $Ge_2Sb_2Te_5$ and stoichiometric GeTe. Anyway similar features can be reasonably assigned to all the alloys belonging to the pseudo-binary line GeTe-Sb_2Te_3. As stressed before, the "umbrella flip" mechanism of order-disorder transition proposed by Kolobov *et al*. for these alloys suggests that 4-coordinated Ge atoms are bound just with Te atoms, and Ge-Ge and Sb-Ge bonds cannot be found (or, at least, are not significant) in the amorphous structure. From the similarity of Sb *K*-edge X-ray near edge structure spectra in the two phases, it was inferred that the arrangement of atoms around Sb remains practically unchanged during amorphization, which means that Sb atoms are bound only to Te in both phases (fig.1.19)..

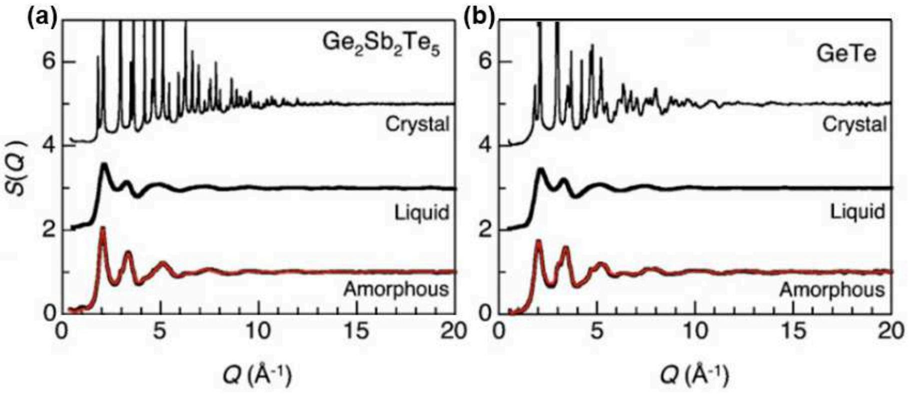

Figure 1.24 (a)(b) Total structure factors S(Q) of crystal, liquid, and amorphous $Ge_2Sb_2Te_5$ and GeTe. Black lines and red lines represent the experimental data and the best-fitted result of the RMC simulation [Koh06].

Baker *et al.* combined bond constraint theory and coordination numbers extracted from extended X-ray-absorption fine structure (EXAFS) spectra of amorphous $Ge_2Sb_2Te_5$ concluded that 17% of Te atoms are overcoordinated and Ge atoms are involved in Te3Ge-GeTe3 structural units [Bak06]. In contrast to the umbrella flip mechanism, this model is based on the preferential formation of Ge-Ge bonds. More recently, Kohara *et al.* carried out an X-ray diffraction study on the structure of amorphous, liquid, and crystalline GeTe and $Ge_2Sb_2Te_5$, fig. 1.24 [Koh06]. The experimental structure factor was fitted by the reverse Monte Carlo simulation technique by assuming that there are no Ge-Ge, Ge-Sb, and Sb-Sb bonds in amorphous $Ge_2Sb_2Te_5$. The analysis of the obtained particle configuration, fig.1.25(a), showed that similar to the crystalline state, ring size distribution is dominated by four- and six-membered rings, which can be the key for fast crystallization. On the other hand, they found that *a*-GeTe has various size (both odd- and even-numbered) rings due to the formation of Ge–Ge homopolar bonds. These differences in the network of the ring structure are clearly visible in three dimensional atomic configurations obtained from the Random Monte Carlo simulation, as shown in fig.1.25(b).

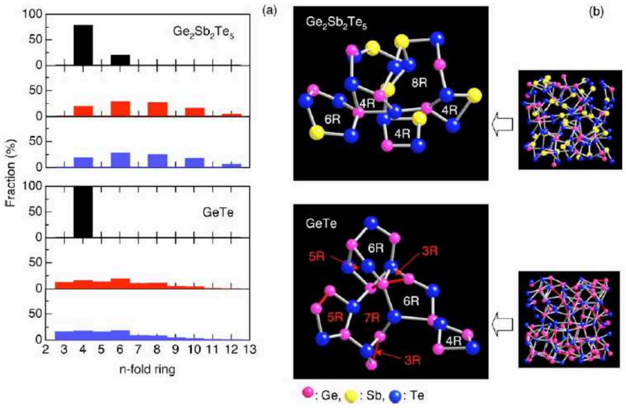

Figure 1.25 **(a) GST and GeTe ring size distribution of crystalline (black bars), amorphous starting from crystal (red bars) and amorphous starting from random atomic distribution (blue bars). (b) Atomic configuration and enlarged framework of a-GST and a-GeTe obtained from the RMC calculations (blue=Te, pink=Ge, yellow=Sb) [Koh06].**

Thus the construction of odd-numbered rings induced by the formation of Ge–Ge homopolar bonds in *a*-GeTe disturbs the fast crystallization of the amorphous phase, and it is worth mentioning that the addition of Sb atom to GeTe can effectively prevent the formation of Ge–Ge bonds in *a*-$Ge_2Sb_2Te_5$. This description is able to explain the higher crystallization temperature measured in GeTe with respect to GST. Unfortunately, it was also shown that, in this last case, even if Ge-Ge, Ge-Sb, and Sb-Sb bonds were allowed, the ring size distribution was dominated by even-membered rings. Though this model is simple and straightforward, experimental observations do not lend sufficient support to it. The main problems are that Sb and Te are practically indistinguishable by X-ray diffraction and the weights of Ge-Ge and Ge-Sb correlations in the experimental data are too low (2% and 7%, respectively), thus a good fit of a single X-ray measurement does not necessarily mean that these bonds are really missing from the amorphous phase.

An interesting paper was published by Jovari *et al.* [Jov08]. Here, they investigated in a unic framework the amorphous structure of GST by high energy X-ray diffraction, extended X-ray-absorption fine structure, neutron diffraction and reverse Monte Carlo simulations. Their attention was focused on the presence of Ge-Ge, Ge-Sb and Te-Te “wrong bonds”, not existing in the crystalline phase. Experimental data are reported in fig.1.26. A model structure accounting for both neutron and x-ray structure factors could already give a more accurate determination of Ge-related structural parameters. Unfortunately, even neutron diffraction is not able to distinguish between Sb and Te since the atomic scattering lengths are similar (5.58 and 5.80 fm, respectively). Sb and Te are also similar as photoelectron backscatterers, thus a Ge *K*-edge EXAFS measurement alone cannot distinguish between Ge-Te and Ge-Sb pairs. This degeneracy can be resolved by Sb and Te *K*-edge data since Ge and Te possess rather different backscattering powers. The five datasets of fig.1.26 were modeled simultaneously by the reverse Monte Carlo simulation technique. The results obtained are thus consistent with all the experimental data. Within the errors, the coordination number of Te, Sb and Ge is 2, 3 and 4, respectively. Thus, all atoms seem to satisfy the 8-N rule in agreement with the considerations of sect. 1.3.4. We will tackle this topic more in detail in par. 3.2. Besides Te-Ge and Te-Sb bonds, present in the crystalline phases, Ge-Ge and Sb-Ge bonding was also found to be significant (~20%). They have also calculated the bond angle distributions centered on Ge, Sb, and

Te. They are similar in amorphous $Ge_2Sb_2Te_5$ and have their peaks at about 90° suggesting an under coordinated octahedral arrangement rather than a tetrahedral configuration. In the case of Te-Sb-Te, there is a minor peak close to 180° showing that some Sb atoms and two of their three neighbors can be found in a linear arrangement, which also means that these Sb atom and their neighboring Te atoms are in the same plane.

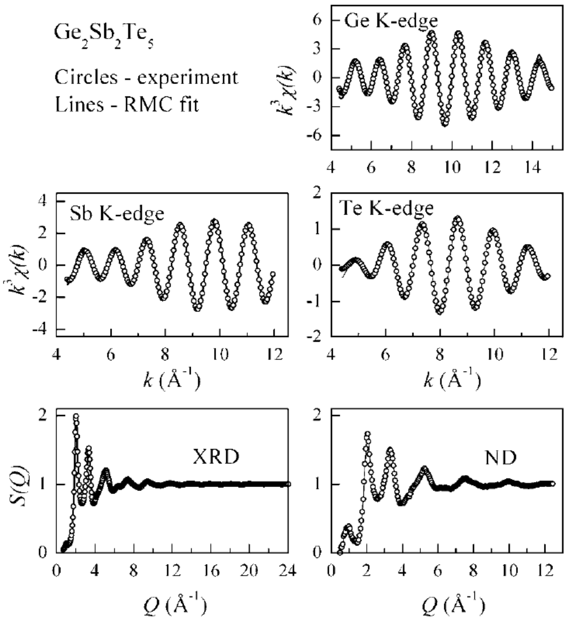

Figure 1.26 Measured EXAFS spectra and X-ray/neutron diffraction structure factors of as-sputtered amorphous $Ge_2Sb_2Te_5$ (circles). Simultaneous reverse Monte Carlo simulation of the experimental XRD, ND, and EXAFS data (lines) [Jov08].

As current models of Ge-Sb-Te phase-change materials concentrate mostly on the environment of Ge atoms more profound analysis of Ge four-coordination environments was carried out. Unfortunately, the predominance of certain local motifs suggested by Kolobov ($GeTe_4$) or Baker (Te3Ge-GeTe3) was not verified. All the previous considerations can be reasonably extended to the other phase change materials belonging to the pseudo-binary line GeTe-Sb_2Te_3.

Another point of view about the structure of amorphous GST was proposed by Caravati *et al.* by *ab initio* molecular dynamics simulations [Car07]. Their results are similar to the RMC calculations proposed by Jovari. The amorphous structure is obtained starting from the rock-salt crystal by the quenching of the liquid phase. The distribution of the coordination number for the different species are reported in the inset of fig.1.27. Ge and Sb atoms are mostly four-coordinated and form bonds preferentially with three coordinated Te atoms. Sb and Te are then over coordinated and as stressed in the previous sections this is a peculiar feature of the crystalline phase.

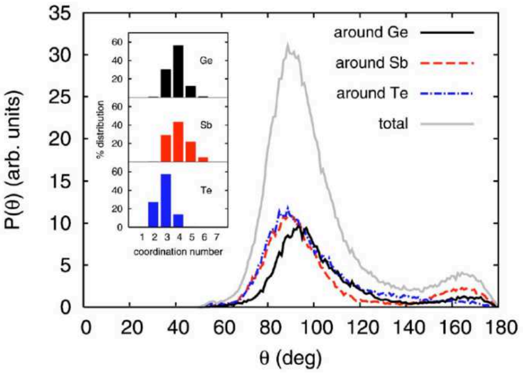

Figure 1.27 Angle distribution function (total and resolved for different central atoms) of the amorphous $Ge_2Sb_2Te_5$ network. Inset: distribution of coordination numbers of the different atomic species obtained by integration of the partial pair correlation functions [Car07].

They observed also a large fraction of homopolar Ge-Ge, Sb-Sb and Ge-Sb bonds, namely, 38% of Ge are bonded with at least another Ge or Sb, a percentage which is raised to 52% for Ge atoms four-coordinated. The fraction of Sb bonded to another Sb or Ge is instead 59%. The concentration of Te-Te bonds is somehow lower; 27% of Te atoms are involved in homopolar bonds arranged into dimers and trimers. As stressed before, the large concentration of homopolar bonds is not reproduced by the RMC model proposed by Kohara but is confirmed by Baker and Jovari. Insight on the local geometry is further gained from the angle distribution function in fig. 1.27. Angles at ~90° and ~180° clearly dominate the bonding network and this is a reminiscent of the distorted octahedral-like geometry of the metastable cubic crystal.

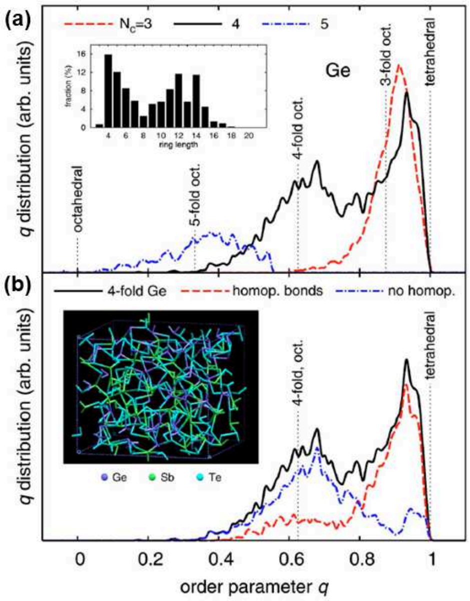

Figure 1.28 Distribution of the local order parameter q for Ge with different coordination numbers. q=1 for the ideal tetrahedral geometry, q=0 for the six-coordinated octahedral site, and q=5/8 for a four-coordinated defective octahedral site. (a) q-distribution resolved for Ge with different coordination number. (b) q-distribution for four-coordinated Ge further resolved for Ge with at least one homopolar bond with Ge or Sb or bonding with Te only (no homopolar bonds). Top panel inset: ring distribution function of a-GST. Bottom panel inset: snapshot of the 270-atom model of a-GST [Car07].

A snapshot of the *a*-GST model is shown in fig.1.28(b). However, the main coordination of Ge(Sb) and Te of four and three, respectively, is lower than the ideal octahedral value of six. The presence of neighboring vacancies could be responsible for the lower coordination. Contrary to Te and Sb, only a fraction of Ge atoms are in a defective octahedral site. A large fraction of four-coordinated Ge atoms ($\sim 30\%$) are in a tetrahedral environment. A better indicator of the tetrahedral geometry is given by the local order parameter $q = 1 - 3/8 \sum_{i>k} \left(1/3 + \cos\theta_{ijk}\right)^2$ where the sum runs over the couples of atoms bonded to a central atom *j*. The distribution of the local order parameter *q* for Ge atoms is reported in fig.1.28(a) for different coordination numbers. The four-coordinated Ge distribution is clearly bimodal with peaks corresponding to defective octahedral and tetrahedra. In contrast, the *q*-distribution for Te and Sb does not show any signature of the tetrahedral geometry. The *q*-distribution for four-coordinated Ge is further analyzed in terms of atoms bonded to Te only or to at least one Ge or Sb, fig.1.28(b). The presence of bonds with Ge or Sb clearly favors the tetrahedral geometry. Only few tetrahedral Ge are bonded to Te only. On the other hand, all Ge with more than one homopolar bond (with Ge or Sb) are in the tetrahedral geometry. By integrating the tetrahedral peak of the *q*-distribution in the range of 0.8-1.0, they estimated that 33% of Ge atoms are in a tetrahedral environment. What about the medium range order? In contrast with the results of Kohara proposed in fig.1.25, both even and odd rings are present in the amorphous network. Anyway, the distribution has a pronounced maximum at four-membered rings typical of the rocksalt structure. The 82% of four-membered rings are in the form *ABAB* (A=Sb or Ge, B=Te), without homopolar bonds.

In conclusion we can summarize the main features of the amorphous network of phase change materials belonging to the pseudo-binary line GeTe-Sb_2Te_3. Sb and Te are slightly over-coordinated with respect to the value expected from the 8-N rule. Ge-Ge, Te-Te, Sb-Ge wrong bonds, not existing in the crystalline phase, are present in a significative concentration. Te, Sb and the 70% of Ge atoms are in defective octahedral sites but lower than six coordinated. The remaining Ge atoms are tetrahedrally bound. The medium range order is dominated by the presence of four-membered *ABAB* rings characteristic of the metastable rocksalt structure.

1.4.2 Bonding mechanism

A good description of the bonding mechanism in phase change materials was proposed by Xu *et al.* [Xu09]. In an ‘‘ideal’’ covalent glass model, each constituent atom (e.g., Ge, Sb, and Te) strives to obey the ‘‘*8-N rule*’’. The coordination number should be equal to 8-N where N is the number of the valence electrons. We focus our attention again on GST alloys. For Ge, its four valence electrons, $4s^2 4p^2$, hybridize into four sp^3 orbitals to lower the total energy, thus forming the 109° angle tetrahedral bonding typical of the IV group solids.

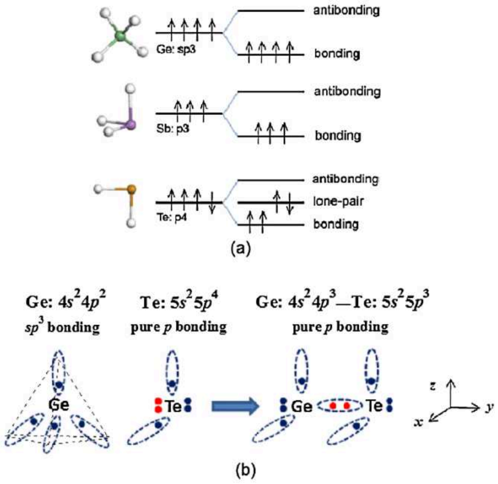

Figure 1.29 Schematic of (a) the electronic structure and the bonding geometry of Ge, Sb, and Te in an ideal glass model, and (b) the valence alternation process between Ge and Te. In 3D space, the sp^3 bonds have the tetrahedral shape with bond angles of ~109°, while the *p* bonds are perpendicular to each other. The valence alternation changes not only the coordination number of the Ge and Te, but also the bond angle around Ge [Xu09].

The Sb atom has two *5s* electrons which are usually not involved in covalent bonding, and the remaining three *5p* electrons occupy the three *p* orbitals. The Te atom has one more electron than Sb, such that one of the *p* orbitals is fully occupied by two paired electrons, which are called nonbonding or ‘‘lone pair’’ electrons, leaving two bonding valence electrons, fig.1.29(a).

The bonds of Sb and Te tend to have the 90° right angle because the *p* orbitals are perpendicular to one another. As stressed before, in the bond-angle distribution of fig. 1.27, the Sb and Te in the a-GST have then predominantly right-angle bonds and resembles the scenario in c-GST (rocksaltlike structure) to a large extent. Interestingly most of the Ge atoms have bond angles close to 90°, but not 109°.

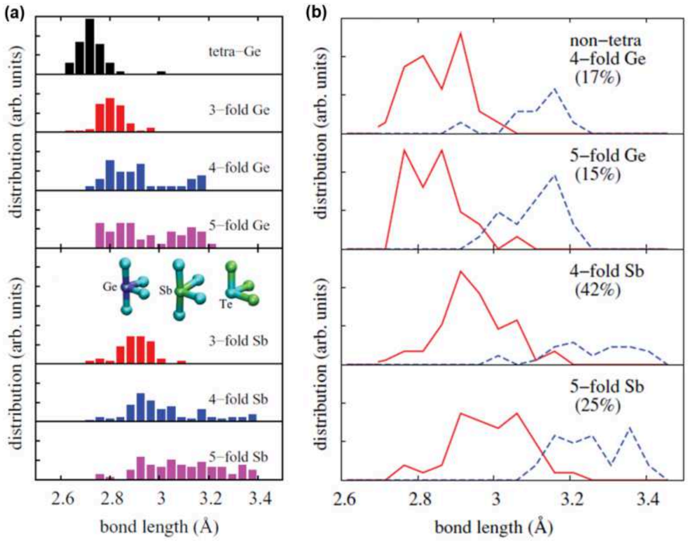

Figure 1.30 (a) Calculated distribution of bond lengths of Ge and Sb in tetrahedral and defective octahedral sites with different coordination numbers. $Ge_2Sb_2Te_5$ is the investigated alloy. Sketches of the common local arrangement of the different atomic species is also shown. (b) Distribution of the three shorter and longer bond lenghts of Ge/Sb in different octahedral sites [Sos11].

This difference results from the changes in the electronic structure when Ge interacts with Te in GST, in a process known as valence alternation. This scenario is schematically illustrated in fig.1.29(b). The two lone-pair electrons of Te (red dots) are in a higher-energy state compared to the bonding electrons, so Te tends to donate one of them to the neighboring Ge, and becomes trivalent as a result. In the meantime, the sp^3 hybridization in Ge is replaced by *p* bonding via the three *p* orbitals. In this process, there is an energy cost when the four *sp*^{3} electrons break into two *s* electrons and two bonding *p* electrons, because the stability resulting from the hybridization is lost. However, the energy decreases when the two energetic lone-pair electrons convert to bonding *p* electrons. The overall energy change of the entire system is presumably composition dependent, and for Ge atoms the *sp*^{3} hybridization and local tetrahedral configuration are more likely to be converted into *p* bonding in a Te-rich environment, where the energetic lone-pair *p* electrons are abundant. As a result of the valence alternation, both of Ge and Te atoms become threefold coordinated with the *p* bonds. The bond angles around Ge tend to become 90°, as illustrated in fig.1.29(b). This is a simplified model. As we stressed in the previous section, the presence of Ge-Ge or Ge-Sb "wrong" bonds promotes tetrahedral coordination and a Ge average coordination number between three and four is expected in the real amorphous network. In the case of Te atoms, higher coordination is statistically not prohibited but the presence of homopolar Te-Te bonds, by the preservation of the lone pairs, lowers the average coordination number below three. Anyway, all Te and Sb and ~70% of Ge atoms are in a defective octahedral geometry with octahedral bonding angles but lower than six coordination. The calculated bond length distributions of Ge and Sb atoms in octahedral-like sites are reported in fig.1.30(a) varying the coordination number [Sos11]. These distributions are bimodal and this feature becomes more evident in fig.1.30(b), where they are plotted for the three shorter bonds and for the longer ones. Therefore the defective octahedral-like environment of Ge/Sb recalls a 3+*n* (*n* = 0–2) geometry similar to the 3+3 bonding coordination in crystalline α-GeTe (i.e. 3 shorter and 3 longer bonds).

1.4.3 Local order of the liquid phase

Much less is known about the liquid state of phase-change materials. This is an important topic since the liquid phase plays a prominent role in both amorphization and recrystallization. As stressed in the previous paragraphs, the amorphous state is achieved by quenching the liquid, while fast recrystallization proceeds above the glass temperature, through the undercooled liquid state. The functioning of the storage devices involves then the liquid phase during the erase/write cycles. A paper of Steimer *et al.* has shed light on this argument [Ste08]. The large part of phase change material contain roughly 50% Te atoms. Hence, an octahedral order, as found in Te, or a tetrahedral order, as found, e.g., in most II-VI alloys is expected.

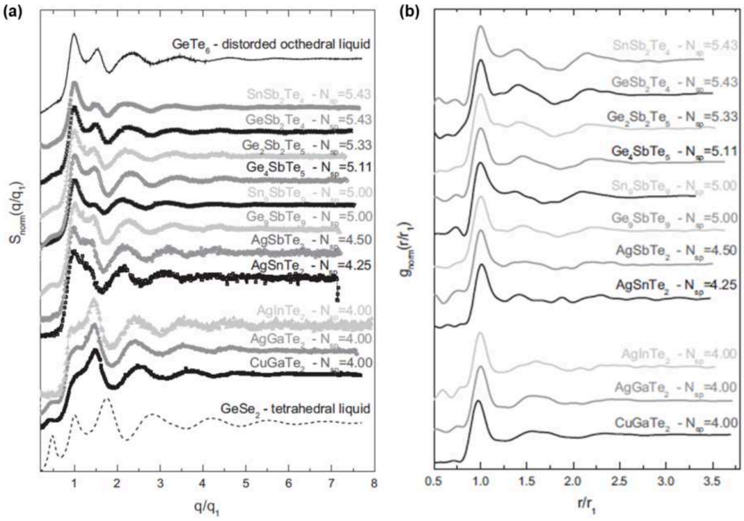

Figure 1.31 (a) Normalized structure factors of several Te-rich alloys as function of the number of valence electrons (N_{sp}). An inversion of the relative heights of the first two peak occurs for $N_{sp} \geq 4.25$ (b) Normalized pair correlation functions. A shift of the second peak position towards lower r/r_1 is clear increasing N_{sp}. This reflects the transition from tetrahedral to octahedral liquids [Ste08].

Total structure factors obtained by neutron scattering measurements are displayed in fig. 1.31(a). For a better comparison, these factors have been normalized. The figure is ordered by increasing the number of valence electron (N_{sp}), from bottom to top. Two extreme cases have been added: $GeSe_2$, which is known to form a tetrahedral liquid [Pen91], and $GeTe_6$, which shows distorted octahedral order [Ber03]. The different structure factors are indicative of a shift from tetrahedral to octahedral order. An inversion of the relative heights of the first two peaks of S(q) with increasing number of valence electrons is clear in fig. 1.31. Taking the quantity S =S(q_2)/S(q_1), by comparison with the known structures of $GeSe_2$ and $GeTe_6$, liquids with S>1 are tetrahedral, while those with S<1 are octahedral. The pair correlation functions g(r) corresponding to the structures in 1.31(a) are plotted in part (b), normalized and shifted. The positions of the first two peaks (r_1 and r_2) are less sharply defined than q_1 and q_2.

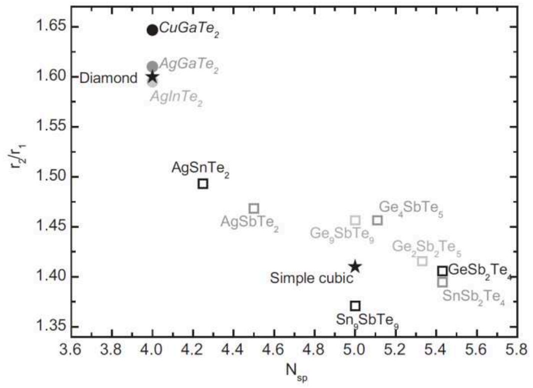

Figure 1.32 Ratio of next-nearest neighbor to nearest neighbor distance r_2/r_1 for liquid alloys as a function of the number of valence electrons (N_{sp}). Full circles and open squares are used for tetrahedral and octahedral liquids, respectively. The black stars indicate the two ideal cases, diamond and simple cubic structures.

The ratio r=r_2/r_1 is plotted in 1.32 as a function of N_{sp}. With increasing N_{sp}, this ratio decreases from roughly $4/\sqrt{6} \approx 1.6$ (nextnearest to nearest neighbor distance in diamond structure, corresponding to an ideal tetrahedral environment) to $\sqrt{2} \approx 1.4$ (simple cubic or rocksalt structure, corresponding to an ideal octahedral environment). This confirms the systematic trend observed, from tetrahedral to octahedral order in liquid Te alloys with increasing average number of valence electrons. The structures of the liquids, as proposed for the amorphous and the crystalline phase, can be explained by the same molecular orbital argument: in a tetrahedral structure, electrons occupy the bonding sp^3 orbitals up to $N_{sp}=4$. Above $N_{sp}=4$, the antibonding sp^3 levels are occupied, and stability decreases. Analogously, in a simple cubic structure the electronic configuration can be described by three levels: a filled s level (with 2 electrons) and a pair of bonding-antibonding p levels (p and p*), which may accommodate 3 electrons each. As a consequence, the bonding levels are filled up to a maximum of 5 sp-electrons. Bonding is achieved through the sole *p* orbitals (p_x, p_y, p_z), and due to their orthogonal orientations, an octahedral coordination is expected. The maximum stability in the octahedral environment is achieved for 5 *sp* electrons. The experimental data for the Te-based liquid alloys presented here demonstrate that the competition between the tetrahedral and octahedral orders leads to a crossover at around $N_{sp}=4.25$.

References

[Adl80] D. Adler , M. S. Shur , M. Silver , S. R. Ovshinsky , *J. Appl. Phys.*, *51* , 3289 (1980).

[Ako07] J. Akola , R. O. Jones , *Phys. Rev. B*, *76* , 235201 (2007).

[Bai06] S. A. Baily, D. Emin , *Phys. Rev. B*, *73* , 165211 (2006).

[Bai06b] S. A. Baily, D. Emin, H. Li , *Solid State Communications*, *139* , 161 (2006).

[Bak06] D. A. Baker, M. A. Paesler, G. Lucovsky, S. C. Agarwal, P. C. Taylor, *Phys. Rev. Lett.*, *96*, 255501 (2006).

[Ber03] C. Bergman, C. Bichara, J. P. Gaspard,Y. Tsuchiya, Phys. Rev. B, 67, 104202 (2003).

[Bre08] M. J. Breitwiseh, *Phase Change Materials Science and Applications*, chap. 17, Springer (2008).

[Bru09] G. Bruns, P. Merkelbach, C. Schlockermann, M. Salinga, M. Wuttig, T. D. Happ, J. B. Philipp, M. Kund, *Appl. Phys. Lett.* 95, 043108 (2009)

[Bur10] G. W. Burr, M. J. Breitwisch, M. Franceschini, D. Garetto, K. Gopalakrishnan, B. Jackson, B. Kurdi, C. Lam, L. A. Lastras, A. Padilla, B. Rajendran, S. Raoux, and R. S. Shenoy, *J. Vac. Sci. Technol. B,* 28 223 (2010).

[Car07] S. Caravati, M. Bernasconi, T. D. Kuhne, M. Krack, M. Parrinello, *Appl. Phys. Lett.*, *91*, 171906 (2007).

[Che86] M. Chen, K. A. Rubin, R. W. Barton, *Appl. Phys. Lett.*, 49, 502-504 (1986).

[Crc97] R. C.Weast (Ed.), *CRC Handbook of Chemistry and Physics*, 78th edition, CRC Press, Cleveland, Ohio (1997)

[Das08] J. L. F. Da Silva , A. Walsh , H. L. Lee , *Phys. Rev. B*, *78* , 224111 (2008) .

[Deb08] R. De Bastiani, Crystallization and Ion Beam Induced Amorphization of $Ge_2Sb_2Te_5$ thin films, Doctoral thesis, University of Catania (2008).

[Emi06] D. Emin, *Phys. Rev. B*, *74* , 035206 (2006).

[Han58] M. Hansen, ed., *Constitution of binary alloys*, McGraw-Hill, New York, (1958).

[Iel07] D. Ielmini, Y. G. Zhang, *Appl. Phys. Lett.*, *90* , 192102 (2007).

[Iel08] D. Ielmini, *Phase Change Materials Science and Applications*, chap. 14, Springer (2008).

[Iel08b] D. Ielmini, *Phys. Rev. B*, *78* , 035308 (2008).

[Jov08] P. Jovari, I. Kaban, J. Steiner, B. Beuneu, A. Schops, M. A. Webb, *Phys. Rev. B*, *77*, 035202 (2008).

[Kim07] J. J. Kim, K. Kobayashi, E. Ikenaga, M. Kobata , S. Ueda, T. Matsunaga, K. Kifune, R. Kojima, N. Yamada , *Phys. Rev. B*, *76*, 115124 (2007).

[Koh06]S. Kohara, K. Kato, S. Kimura, H. Tanaka, T. Usuki, K. Suzuya, H. Tanaka, Y. Moritomo, T. Matsunaga, N. Yamada, Y. Tanaka, H. Suematsu, M. Takata, *Appl. Phys. Lett.*, *89*, 201910 (2006).

[Kol03] A. V. Kolobov , J. Tominaga , P. Fons , T. Uruga , *Appl. Phys. Lett.*, *82* , 382 (2003).

[Kol04] A. V. Kolobov , P. Fons , A. I. Frenkel , A. L. Ankudinov , J. Tominaga , T. Uruga , *Nature Materials*, *3*, 703 (2004).

[Lan05] M. H. R. Lankhorst, B. W. S. M. M. Ketelaars, R. A. M. Woltersm, *Nature Materials,* 4, 347 (2005).

[Len08] D. Lencer , M. Salinga , B. Grabowski , T. Hickel , J. Neugebauer, M. Wuttig, *Nature Materials*, 7 , 972 (2008).

[Len10] D. Lencer, Design Rules, Local Structure and Lattice-Dynamics of Phase-Change Materials for Data Storage Applications, Doctoral thesis, RWTH Aachen University (2010).

[Mat04] T. Matsunaga, N. Yamada, Y. Kubota, Acta Cryst. B 60, 685, (2004).

[Non00] T. Nonaka, G. Ohbayashi, Y. Toriumi, Y. Mori, H. Hashimoto, *Thin Solid Films*, 370, 258-261 (2000).

[Ovs68] S.R. Ovshinsky, *Phys. Rev. Lett.,* 21, 1450 (1968).

[Par06] Y. J. Park, J. Y. Lee, Y. T. Kim, *Applied Surface Science*, 253, 714–719 (2006)

[Pau39] L. Pauling, *Nature of Chemical Bond* (Cornell Univ. Press, New York, 1939).

[Pen91] I. T. Penfold, P. S. Salmon, Phys. Rev. Lett., 67, 97 (1991).

[Rad08] A. Redaelli, A. Pirovano, A. Benvenuti , A. L. Lacaita, *J. Appl. Phys.*, *103* , 111101 (2008).

[Rao09] S. Raoux, *Annu. Rev. Mater. Res.*, 39, 25–48 (2009).

[Sak69] S. Sakka, J.D. Mackenzie, *J. Non-Cryst. Solids*, 1, 107-142 (1969).

[Sal08] M. Salinga, Phase Change Materials for Non-volatile Electronic Memories, Doctoral thesis, RWTH Aachen University (2008).

[Sha05] S. Shamoto, N. Yamada, T. Matsunaga, T. Proffen, J. W. Richardson, J. H. Chung , T. Egami, *Appl. Phys. Lett.*,*86* , 081904 (2005).

[Shi08] L. Shi, *Phase Change Materials Science and Applications*, chap. 12, Springer (2008).

[Shp08] K. Shportko, S. Kremers, M. Woda, D. Lencer, J. Robertson, M. Wuttig, *Nat. Mater.*, *7* , 653 (2008).

[Sos11] G. C. Sosso, S. Caravati, R. Mazzarello, M. Bernasconi, *Phys. Rev. B*, *83* , 134201 (2011).

[Ste08] C. Steimer, V. Coulet, W. Welnic, H. Dieker, R. Detemple, C. Bichara, B. Beuneu, J. P. Gaspard, M. Wuttig, *Adv. Mater.*, *20* , 4535 (2008).

[Ter09] M. Terao, T. Morikawa, T. Ohta, *Jpn. J. Appl. Phys.*, 48 080001 (2009).

[Tom08] J. Tominaga, *Phase Change Materials Science and Applications*, chap. 13, Springer (2008).

[Wut07] M. Wuttig, N. Yamada, *Nature Materials,* 6, 824 (2007).

[Wut07b] M. Wuttig , D. Lusebrink , D. Wamwangi , W. Welnic , M. Gillessen, R. Dronskowski, *Nature Materials*, 6, 122 (2007).

[Xu09] M. Xu , Y. Q. Cheng , H. W. Sheng , E. Ma , *Phys. Rev. Lett.*, *103*, 195502 (2009).

[Yam08] N. Yamada, *Phase Change Materials Science and Applications*, chap. 10, Springer (2008).

[Yam91] N. Yamanda, E. Ohono, K. Nishiuchi, N. Akahira and M. Takao, *J. Appl. Phys.*, 69, 2849 (1991).

Chapter 2

Theory of phase transitions

After the discussion of the properties of both the amorphous and the crystalline phase, we will focus our attention on the phase transitions, i.e. amorphization and crystallization. While the properties in both phases govern the contrast, the kinetics of the phase transition determine the stability of the states (data retention) and the transition times (device speed). In the following sections, we will first describe the process of amorphization via melt-quenching. Subsequently, the process of crystallization, which typically limits the maximum write rate of phase change memories, is addressed. To this aim we refer to the following papers [Kal06][Kal08][Len11].

2.1 Glass Formation

The second law of thermodynamics states the direction of a spontaneous transition if temperature T and pressure p are externally imposed: $\Delta G<0$. The Gibbs free energy G is defined as $G = U + pV - TS$ where U is the internal energy, S the entropy and V the volume of the system. Hence, under these conditions, if $\Delta G<0$ a process can occur spontaneously. ΔG is the energy gain associated to the transition. The Gibbs free energy for the liquid and the crystalline phase of a generic phase change alloy is shown in fig. 2.1 and it's clear that below the melting point the crystalline phase is energetically favorable. Thermodynamics, on the other hand, is unable to tell if an allowed transition ($\Delta G<0$) occurs or not, and when or how it occurs. This prediction can only be made by kinetic theories of nucleation and growth. We will discuss this point in the next paragraph. As long as another phase of lower free energy does not nucleate, the metastable equilibrium cannot be distinguished from the full equilibrium. Therefore, under proper conditions, crystallization does not occur although the crystalline phase is energetically favorable. As a melt is quenched, it becomes increasingly rigid. Once a critical temperature is passed, i.e. the glass transition temperature T_g, the atomic mobility D becomes too small for the structural rearrangements required to reach thermal equilibrium. Thus, the undercooled liquid is "frozen" in its current structural configuration and crystallization is then avoided.

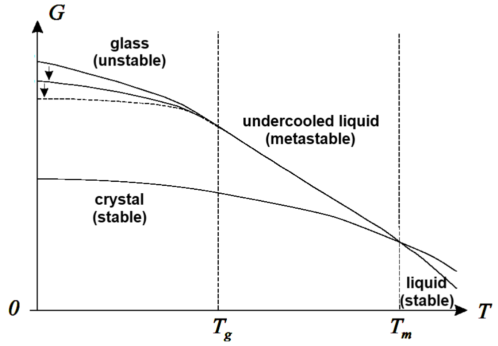

Figure 2.1 Gibbs free energy G in various stability regimes. The glass is created if the formation of the stable crystalline phase is avoided during the quenching of the liquid. The arrows indicate the aging of the glass structure towards more stable isoconfigurational states [Kal06].

The glass transition temperature is commonly defined as the temperature, at which the viscosity equals 10^{12} Pa·s. The resulting glass is out of thermal equilibrium. Thus, a glass is always subject to "aging" effects, evidencing the relaxation towards equilibrium conditions, as indicated by the arrows of fig. 2.1 and 2.2(a). The timescale of these relaxations can be controlled by temperature. The microscopic atomic mobility of a liquid can be inversely related to the macroscopic viscosity η via the Stokes-Einstein relation, that here we report

$$D(T) = \frac{k_B T}{3\pi\lambda\eta(T)}$$

where λ is the interatomic distance, T the temperature and k_B the Boltzmann constant. A glass can be formed at small cooling rates (easy glass former) or via rapid quenching (bad glass former). This behavior is linked to the viscosity temperature dependence. Equivalently, it also relates to the speed of crystallization. Rapid crystallization is a feature of bad glass former materials. The temperature dependence of η varies among materials as is shown in fig.2.2(b). If it is Arrhenius-like, a material is said to have a *strong* liquid. However, many materials exhibit a behavior empirically described by the Tamann–Vogel–Fulcher equation $\eta(T) = \eta_0 \exp\left(A/(T - T_0)\right)$ with η_0, A, and T_0 being constants. These liquids are named *fragile*. Given that the viscosity at both T_g and T_l would be fixed, crystallization upon cooling of a strong (undercooled) melt is more likely bypassed even at moderate cooling rates as compared to the case where the melt is a fragile liquid.

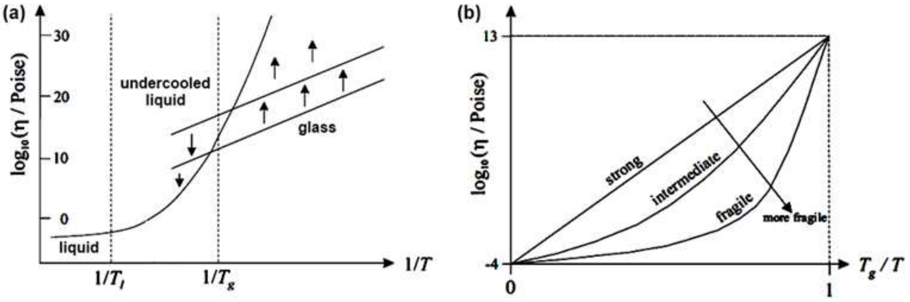

Figure 2.2 **(a) Viscosity η in various stability regimes: stable equilibrium for $T>T_l$, metastable equilibrium for $T_g<T<T_l$ and isoconfigurational states for $T<T_g$. These states experience structural relaxation towards the undercooled liquid, which is in internal equilibrium. This is indicated by the arrows [Kal08]. (b) Qualitative temperature dependence of the viscosity η in the undercooled liquid for strong, intermediate, and fragile liquids (T_g scaled plot) [Kal06].**

Hence, a link between fragility and the difficulty of glass formation can be drawn. For phase-change applications, a rather fragile liquid appears favorable since the crystallization speed would increase more rapidly with increasing temperature (above T_g) although this feature is coupled with bad glass formation. However, the selection of a material with a fragile liquid over one with a strong liquid is, of course, only reasonable if both the normalized temperature dependence and the absolute values of T_g as well as the atomic mobility at elevated temperatures are suitable for operation.

2.2 Crystallization

In a melt, atoms approach each other statistically, forming crystal-like clusters by thermodynamic fluctuations. For simplicity, the clusters are assumed spherical with radius r. The equilibrium cluster distribution follows then the Boltzmann statistics according to the equation

$$N(r) = N_0 \exp\left(-\frac{\Delta G(r)_{cluster}}{k_B T}\right)$$

where N_0 is the total number of atoms in the liquid, $\Delta G_{cluster}$ the free energy change for cluster formation, k_B the Boltzmann constant and T the temperature. The energy gain, fixed the temperature, can be explicated by a sum of two contributions

$$\Delta G(r)_{cluster} = \Delta G_{lc} \cdot \frac{4}{3}\pi r^3 + \sigma \cdot 4\pi r^2$$

ΔG_{lc} is the free energy difference between the liquid and the crystalline phase (fig. 2.1), normalized per unit volume. It is defined to be positive above T_m and negative below T_m. The second term results from the creation of an interface between the cluster and the liquid. This term is always positive, and hence, it doesn't produce an energy gain. The quantity $\sigma>0$ is the interfacial free energy and it's constant. Figure 2.3 shows the evolution of $\Delta G(r)_{cluster}$ as function of r for two different temperatures above and below the T_m. In the first case $\Delta G(r)_{cluster}>0$ and crystallization is always energetically unfavorable. Below the melting point the curve for $\Delta G(r)_{cluster}$ passes through a maximum. Its position, calculated by the simple derivative of the previous equation, defines the critical radius of a cluster. Above this dimension the cluster growth becomes energetically favorable and new stable phase substitutes the metastable one. This critical radius decreases as the free energy difference between the phases increases.

$$\frac{\partial \Delta G(r)_{cluster}}{\partial r} = 0 \rightarrow r_c = -\frac{2\sigma}{\Delta G_{lc}}$$

Substituting r_c to the $\Delta G(r)_{cluster}$ it is possible to obtain the critical work for the formation of a stable cluster

$$\Delta G_c = \frac{16\pi}{3}\frac{\sigma^3}{{\Delta G_{lc}}^2}$$

Therefore, ΔG_c forms an activation barrier against crystallization and is crucial for the undercooling of a liquid. Simply speaking, nucleation is the formation of post-critical clusters of size $r>r_c$ that grow due to a gain in free energy.

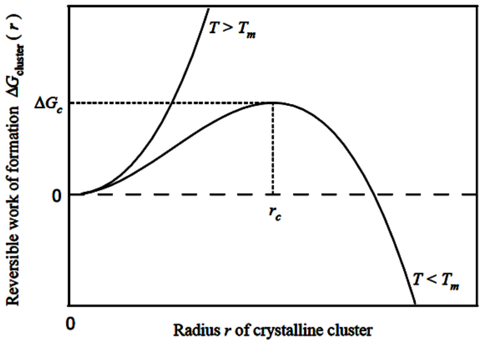

Figure 2.3 Free energy change $G(r)_{cluster}$ for the formation of crystalline clusters of radius r in a liquid. For $T>T_m$, clusters spontaneously decay at any radius. For $T<T_m$, in contrast, clusters decay for $r<r_c$ and grow for $r>r_c$ [Kal08].

In the reality, there can be a back-flux of atoms from the crystalline to the liquid phase also for a post-critical cluster and hence, it can decay again with a certain probability. Hence, Becker and Döring assumed that a steady state cluster distribution is more reasonable than the equilibrium distribution [Bec35][Voh26]. It is clear looking to fig. 2.4 in which a comparison between the distributions is displayed. The particle conservation requires the integral over the cluster distribution to converge, so that the stationary distribution becomes essentially zero at large cluster sizes. The steady state nucleation I^{ss} employed by Becker and Döring and developed by Turnbull and Fisher [Tur49] in the case of diffusion-limited crystallization (i.e. changes of neighbors by diffusive motions are necessary for crystallization) is then

$$I^{ss} = s_{ic} \cdot \frac{2k_B T}{\eta\pi} \cdot N_0^2 \cdot \underbrace{\frac{1}{i_c}\left(\frac{\Delta G_c}{3\pi k_B T}\right)^{1/2}}_{\Gamma} \cdot exp\left(-\frac{\Delta G_c}{k_B T}\right)$$

where s_{ic}~10 and i_c are the number of surface and volume atoms in a critical cluster, η is the viscosity, $N_0 \sim 10^{28} m^{-3}$ the total number of atoms in the liquid phase. Γ is the Zeldovich factor, which only has a weak temperature dependence and is generally between 1/100 and 1/10.

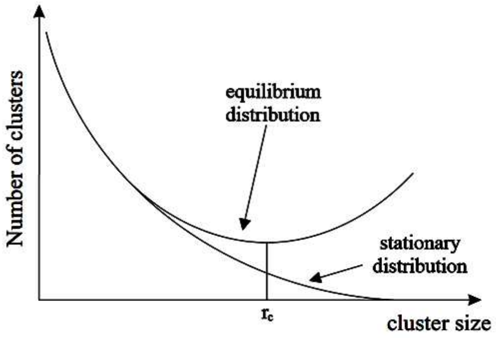

Figure 2.4 Equilibrium and stationary statistical cluster distribution function. The particle conservation requires the integral over the cluster distribution to converge, so that the stationary distribution tends to zero at cluster sizes larger than the critical value r_c [Kal08].

It is then possible to reduce the previous equation to this form

$$I^{ss} \approx \underbrace{\frac{10^{36}}{\eta}}_{I_0^{ss}} \cdot exp\left(-\frac{\Delta G_c}{k_B T}\right) \qquad \frac{1}{m^3 s}$$

As we pointed out before, near the glass temperature the viscosity is equal to ~10^{12} Pa·s and then the pre-exponential factor I_0^{SS} tends to ~10^{24} $m^{-3}s^{-1}$. The nucleation rate becomes negligibly small close to the melting where ΔG_{lc} becomes small (i.e. ΔG_c very large), and close to the glass transition temperature T_g, where the viscosity strongly increases. Starting from the liquid phase, depending on the cooling rate and on the height of the maximum in I^{ss}, which is located between glass transition and melting temperature, crystallization can occur and then prevent glass formation.

The steady state nucleation rate is derived assuming a steady state distribution of clusters with different size. Starting from the liquid phase, if the melt is quickly cooled from above to below the melting point, the steady state cluster distribution has to be established first. The same applies to a glass or an undercooled liquid for which the temperature is suddenly changed since the cluster distribution depends on temperature.

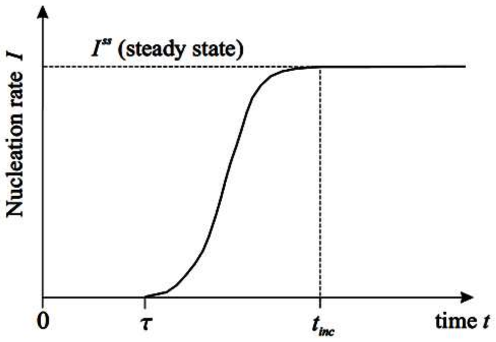

Figure 2.5 Time dependence of the nucleation rate. For t <τ (time lag), no nucleation is observed. The steady state nucleation rate I^{ss} is attained after the incubation time t_{inc} has elapsed [Kal06].

The nucleation rate is then a function of time until the steady state distribution of clusters is attained. As the nucleation rate depends essentially on the number of critical clusters, there is a characteristic time before which nucleation cannot be observed experimentally, i. e. before which the probability for a nucleation event is too low to be observed. This

is called the time lag for nucleation (τ). Subsequently, nucleation can be observed, and the nucleation rate increases with time until the steady state rate is attained. This second time is named incubation time t_{inc}, fig. 2.5.
We have described the formation of stable crystal clusters. Those can grow to macroscopic size. If there is not a composition change upon crystallization, growth is controlled by rearrangement processes only at the liquid(amorphous)-crystalline interface. This growth mode is called interface-controlled [Kal08]. The rearrangement frequency is then independent of the interface position so that the growth velocity is time-independent. The liquid-crystalline interface moves with the velocity

$$u = \nu \cdot \lambda \cdot f_s$$

Where ν is the net rearrangement frequency at the interface, λ the average interatomic distance (i. e., the distance that the interface moves by each rearrangement) and f_s the fraction of sites where a new atom can be incorporated. In the case of diffusion limited crystallization, the difference between the atomic transfer rate from the liquid to the crystal and reverse transfer rate from the crystal to the liquid (i.e. ν) can be written as

$$\nu = \frac{6D}{\lambda^2}\left[1 - exp\left(-\frac{\left|\Delta G_{lc,atom}\right|}{k_B T}\right)\right] \qquad (T < T_m)$$

Where D is usually associated with the diffusivity in the undercooled liquid, and the energy gain is referred to a single atom. Using the Stokes-Einstein equation

$$u = f_s \frac{2k_B T}{\pi\eta\lambda^2}\left[1 - exp\left(-\frac{\left|\Delta G_{lc,atom}\right|}{k_B T}\right)\right] \qquad (T < T_m)$$

The grain growth becomes negligibly small close to the melting where $\Delta G_{lc,atom}$ becomes small, and close to the glass transition temperature T_g, where the viscosity strongly increases. Hence, u exhibits a maximum between T_g and T_0, which is usually located at higher temperature than the maximum for the nucleation rate.

2.2.1 The Johnson–Mehl–Avrami (JMA) model

For isothermal crystallization of an amorphous solid, Johnson, Mehl and Avrami derived a model that relates the three (time-dependent) quantities crystal nucleation rate I, crystal growth velocity u, and crystallized material fraction $0 < \chi < 1$ at constant temperature T [Avr39] [Joh39]. In particular they found

$$\chi(t) = 1 - exp(-kt^n)$$

where

$$k = k_0 exp\left(-\frac{\Delta H}{k_B T}\right)$$

The so called Avrami exponent n, the activation energy ΔH and the values of k are related with both the nucleation rate and crystal growth velocity according to the equations [Rui02]

$$n = a + bc$$

$$\Delta H = E_I + bcE_u$$

$$\ln(k_0) = \ln(I_0) + bc \cdot ln(u_0)$$

$$k = \frac{\pi u^{n-1} I}{3}$$

The parameter a is named nucleation index and governs the time dependence of the nucleation rate. In stationary conditions it results a=1. The dimensionality of the growth is related to the value of b (b=1, 2 or 3 for one-, two- or three-dimensional growth, i.e., where the crystals grow like needles, disks or spheres, respectively). The growth index c=1 for interface controlled growth and c=0.5 when growth is controlled by diffusion (i.e.

composition change upon crystallization occurs). Near the glass temperature, as we will show in the next paragraph, both the nucleation and the growth rate exhibit an Arrhenius dependence on temperature; E_n and E_u are the corresponding activation energies and I_0 and u_0 the pre-exponential factors

$$I = I_0 t^{a-1} exp\left(-\frac{E_I}{k_B T}\right)$$

And

$$u = u_0 exp\left(-\frac{E_u}{k_B T}\right)$$

Kolmogorov derived an expression for the total number of crystallites formed during the transformation in terms of the nucleation and growth parameters [Kol37]. This expression determines implicitly how the average grain size ρ in the crystalline phase depends on the annealing temperature. According to his calculation

$$\rho = \rho_0 exp\left(-\frac{\Delta H'}{k_B T}\right)$$

$$\Delta H' = \frac{ac}{a+bc}\left[E_u + \frac{E_I}{a}\right]$$

When an incubation time, τ, precedes the crystallization process, its temperature dependence is given by

$$\tau = \tau_0 exp\left(\frac{\Delta H/n}{k_B T}\right)$$

In the case of phase change materials is possible to follow the crystallization process near the glass temperature by time resolved reflectivity(resistivity) measurements, fig. 2.6(a). As pointed out in paragraph 1.2.3, these techniques are useful to determine the stability of the amorphous phase by measuring the incubation time as function of temperature. During isothermal annealing, it is possible to define τ as the time at which the maximum of the first derivative of the reflectivity vs time curve occurs. If the amorphous film is crystallized by a random formation of spherical crystalline clusters, according to the effective medium approximation (EMA), this time corresponds to a crystalline fraction $\chi \approx 0.5$ [Bru35]. Anyway, a perfect linear dependence between reflectivity R and the crystalline volume fraction can be assumed as a good approximation

$$\chi(t) = \frac{R(t) - R_\alpha}{R_{Xst} - R_\alpha}$$

Where R is the measured reflectivity, R_α and R_{Xst} the corresponding values of the amorphous and of the crystalline phase, respectively.

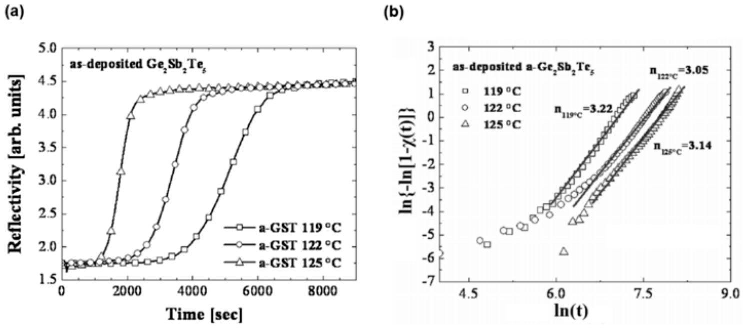

Figure 2.6 **(a) Reflectivity versus annealing time of as-deposited GST thin films. (b)The corresponding JMA at different temperatures. A straight line (continuous lines) with slope n=3 (two-dimensional growth) is fitted to the data points [Deb08].**

It also possible to estimate the value of the Avrami exponent n coupled with the values of k by fitting the first stage of the crystallization process (i.e. $\chi < 0.5$) according to the equation $\chi(t) \approx kt^n$. Alternatively these values are derivable from the fit of the curves

$$ln\{-ln[1 - \chi(t)]\} = \ln(k) + n \cdot \ln(t)$$

attained starting from the JMA equation, fig.2.6(b) [Deb08]. The lag time must be subtracted and this represents a critical point. The results of these analyses should be in agreement with the direct observation of the nucleation and growth rates achievable by microscopy techniques. This topic will be discussed in paragraph 4.3.4 in the case of stoichiometric GeTe.

2.2.2 Nucleation and growth parameters

A detailed analysis on the amorphous-crystal transition of several phase change materials has been performed by Kalb *et al.* [Kal04][Kal05]. Due to the mass density increase upon crystallization, which induces a reduction in film thickness on the order of 5%, crystals could be directly observed as depressions in the amorphous film by atomic force microscope (AFM).

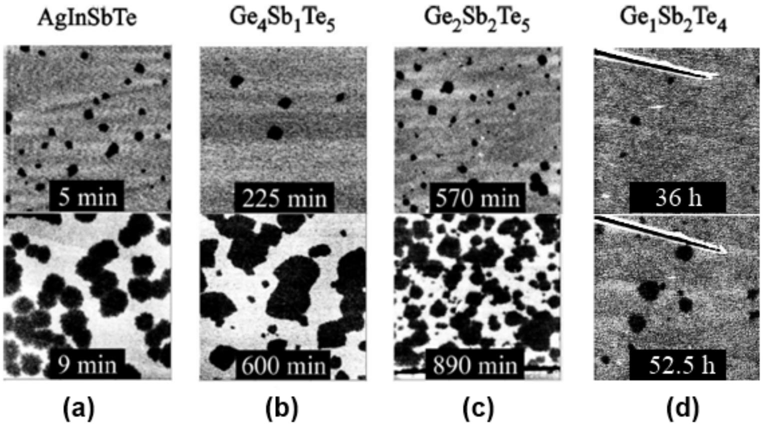

Figure 2.7 AFM scans (3µm x 3µm) of partially crystallized films. Crystals (dark) are visible in an amorphous background (bright). (a) AgInSbTe, 160°C. (b) $Ge_4Sb_1Te_5$, 140°C. (c) $Ge_2Sb_2Te_5$, 115°C. (d) $Ge_1Sb_2Te_4$, 95°C. Total annealing times are indicated [Kal04].

Isothermal annealing in furnace has been employed for a systematic study of sputtered amorphous $Ag_{5.5}In_{6.5}Sb_{59}Te_{29}$ (AIST), $Ge_4Sb_1Te_5$, $Ge_1Sb_2Te_4$ and $Ge_2Sb_2Te_5$ thin films (30-40 nm). Direct observation of crystals enable to establish the temperature dependence of the crystal nucleation rate and crystal growth velocity near the glass transition temperature. While these alloys exhibited similar crystal growth characteristics, the crystal nucleation behavior of AIST differed significantly from that of $Ge_4Sb_1Te_5$, $Ge_1Sb_2Te_4$ and $Ge_2Sb_2Te_5$. Figure 2.7 shows a selection of two AFM scans per alloy. The scans on AgInSbTe differ in two major respects: first, at a given time and temperature (represented by a single AFM scan), the crystal diameter distribution is rather sharp for AgInSbTe but broad for the GeSbTe alloys. Since the isothermal crystal growth velocity of neighboring crystals was observed to be identical, this implies that all (heterogeneous) nucleation sites are approximately simultaneously exhausted for AgInSbTe. In contrast, the isothermal nucleation rate remains nonzero at all times for the GeSbTe alloys.

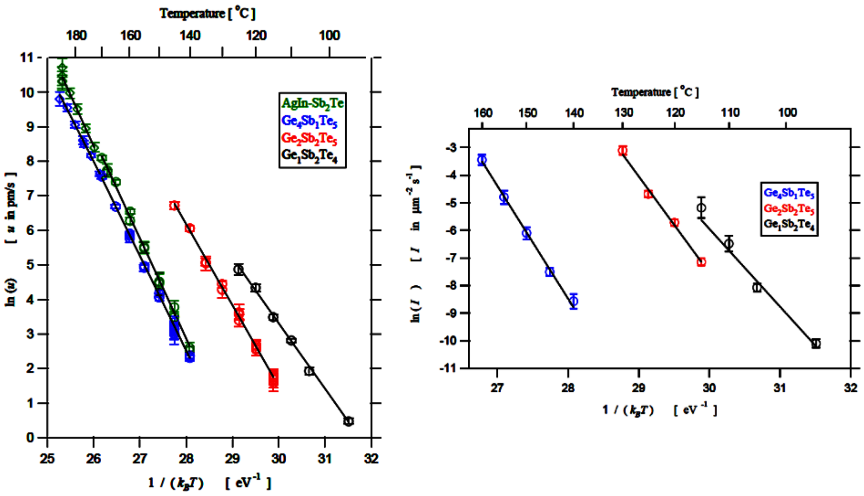

Figure 2.8 (a) Arrhenius plot of the grain growth velocity of several as deposited phase change materials: $Ag_{5.5}In_{6.5}Sb_{59}Te_{29}$ (AIST), $Ge_4Sb_1Te_5$, $Ge_1Sb_2Te_4$ and $Ge_2Sb_2Te_5$. (b) Corresponding Arrhenius plot of the nucleation rate. Data on AIST are not reported since this alloy shows a simultaneous exhaustion of nucleation sites [Kal06].

Second, the total number of crystals per unit area, which would be observed after complete crystallization of the sample surface, increases with increasing temperature for the GeSbTe alloys, but adopts a temperature-independent value of 5.0±0.3 µm^{-2} for AgInSbTe. This behavior was observed in the entire temperature range investigated. The isothermal crystal growth velocity was observed to be time independent for all three alloys. This implies that the growth was interface-controlled (in contrast to diffusion-controlled growth, where the position of the interface is proportional to the square root of time). Figure 2.8(a) is an Arrhenius plot of the crystal growth velocities u. Growth velocities of AgInSbTe and $Ge_4Sb_1Te_5$ are similar at a given temperature. As pointed out in the previous paragraph, crystal growth is thermally activated. The fitting parameters obtained from the Arrhenius fits are given in Table 2.1. For small times, no crystals nucleate. The time lag is defined as the time at which the first crystal (the one with the largest diameter) nucleates, counted from the beginning of the first isothermal anneal. Also this physical quantity has an Arrhenius dependence on temperature and fitting parameters are reported in Table 2.1. The nucleation rate $I(t_i)$ at time t_i was obtained from

$$I(t_i) = \dot{N}(t_i)/(1 - \chi(t_i))$$

where $N(t_i)$ is the crystal number and $\chi(t_i)$ is the crystallized surface fraction. The factor $\left(1 - \chi(t_i)\right)$ normalizes $\dot{N}(t_i)$ because crystals can only nucleate in the untransformed fraction $\left(1 - \chi(t_i)\right)$ of the surface. $I(T)$ is plotted as a function of temperature in fig.2.8(b) for the GeSbTe alloys. The fit parameters are listed in the following table.

Alloy	$\ln(u_0)$ (u_0 in pm/s)	E_u (eV)	$\ln(\tau_0)$ (τ_0 in s)	E_τ (eV)	$\ln(I_0\ )$ (I_0^{ss} in $\mu m^{-2}s^{-1}$)	E_I (eV)
AgIn-Sb_2Te	84.00 ± 1.22	2.90 ± 0.05	-57.75 ± 4.86	2.33 ± 0.18	no data	no data
$Ge_4Sb_1Te_5$	79.15 ± 0.79	2.74 ± 0.03	no data	no data	105.96 ± 5.53	4.09 ± 0.20
$Ge_2Sb_2Te_5$	71.95 ± 1.46	2.35 ± 0.05	-72.36 ± 3.77	2.74 ± 0.13	97.53 ± 4.86	3.50 ± 0.17
$Ge_1Sb_2Te_4$	60.11 ± 1.53	1.89 ± 0.05	-60.19 ± 1.97	2.27 ± 0.06	78.75 ± 5.69	2.82 ± 0.18

Table 2.1 Arrhenius fit parameters for the crystal growth velocity (u), for the nucleation rate (I) and for the lag time (τ) of several amorphous phase change materials.

We can now turn our attention on the stoichiometric GeTe alloy. A systematic study performed by Coombs *et al.* has proved to be particularly important for our work [Coo95]. It demonstrated that two different classes of phase change materials can be defined: growth- and nucleation-dominated materials. In the first case the probability for nucleation is much lower than for crystal growth, as is depicted in fig. 2.9(b), and then the crystallization of an amorphous mark will start from the amorphous-crystalline interface and proceed inwards. In the second case the nucleation rate is high enough to allow the crystallization by random nucleation and growth even in presence of a crystalline rim.

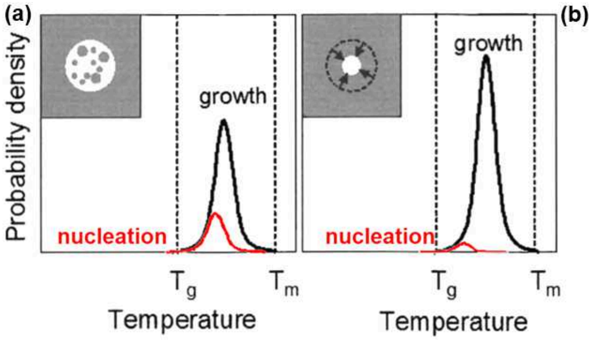

Figure 2.9 Probability for nucleation and growth as a function of temperature for nucleation- (a) and growth-dominated materials (b). If we consider an amorphous mark in a crystalline layer, in (a) crystallization occurs by a process of nucleation and growth, in (b) crystallization proceeds by crystal growth from the amorphous-crystal interface [Pie08].

Unlike GeSbTe alloys, stoichiometric GeTe shows a growth-dominated crystallization. This behavior induces the formation of micrometric crystalline grain in a full amorphous film since in this case the crystallization always starts with the formation of a nucleus. Under these conditions, to study the amorphous-crystal transition, an optical microscope is then necessary rather than a transmission electron or atomic force microscope. The change in reflectivity is used to distinguish the formation of crystalline grains within the amorphous background. This topic will be discussed more in detail in sect. 4.4.1. Here we report only the nucleation and growth parameters that we have measured, table 2.2. The $Ge_2Sb_2Te_5$ and Ge data are reported for comparison [Ger79]. It's interesting to note that GeTe exhibits a higher nucleation activation energy than $Ge_2Sb_2Te_5$ whereas the pre-exponential factors are similar. The activation energy for crystal growth shows an opposite trend equilibrated by a change in the pre-exponential factor. These differences are able to explain the different crystallization kinetics (i.e. growth- vs nucleation-dominated). A higher activation energy for nucleation can be related to a higher interfacial free energy or alternatively to a smaller energy difference between the amorphous and the crystalline phase.

Alloy	$\ln(u_0)$ (u_0 in pm/s)	E_u (eV)	$\ln(I_0\ )$ (I_0^{ss} in µm^{-2}s^{-1})	E_I (eV)
$Ge_2Sb_2Te_5$	71.95 ± 1.46	2.35 ± 0.05	97.53 ± 4.86	3.50 ± 0.17
GeTe	62 ± 4	2.0 ± 0.2	103 ± 6	4.3 ± 0.2
Ge	45 ± 5	2.3 ± 0.1	30 ± 1	2.5 ± 0.1

Table 2.2 Arrhenius fit parameters for the crystal growth velocity (u) and for the nucleation rate (I) of GeTe and $Ge_2Sb_2Te_5$ thin films. Ge data are reported for comparison.

On the other hand, looking to the data of pure Ge it is clear that phase change materials exhibit huge pre-exponential factors for both nucleation and growth. This is a strange feature and several orders of magnitude cannot be reasonably related to a change in diffusivity (viscosity). A peculiar phase change mechanism could be the source of this particular behavior. Several studies are reported in the literature about this topic and in the next paragraph a short overview is presented.

2.2.3 Atomistic models for crystallization

As discussed in the previous chapter, a noteworthy model for Ge:Sb:Te systems crystallization was given by Kolobov et al., the so-called umbrella-flip model [Kol04]. It stated that the main structural rearrangement taking place upon crystallization is a flip of germanium from tetrahedral to octahedral sites. A schematic representation of this mechanism is shown in fig. 2.10. Since this model not only gave an intuitive explanation of why the phase transition proceeds so fast, yet involved a change in bonding significant enough to account for the properties contrast observed, it attracted much attention. A lot of successive studies attempted to test this model. As pointed out in paragraph 1.3.3, extensive theoretical simulations and experimental studies have shown that, while tetrahedrally coordinated germanium atoms are present in the amorphous phase, they represent only a minority, making up only roughly one third of all germanium atoms.

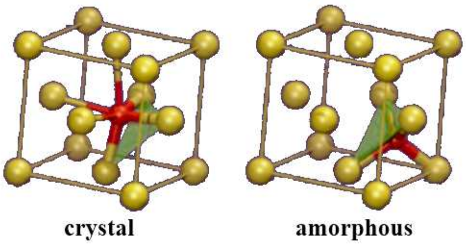

Figure 2.10 **Local structure of a Ge:Sb:Te systems around Ge atoms in the crystalline and in the amorphous phase, according to the umbrella-flip model. Stronger bond are shown thicker than weaker bonds. Coordination changes from tetrahedral to octahedral upon crystallization [Kol04].**

Moreover, they typically involve homopolar Ge-Ge or Ge-Sb bonds ("wrong bonds") rather than only Ge-Te bonds as stated by the umbrella-flip model. To conclude, the umbrella-flip model turned out not to be a realistic model of the phase transition. A second model was proposed by Kohara on the basis of the measurements and Monte Carlo calculations that we have shown in paragraph 1.4.1. From the comparison of the ring statistics, fig. 1.25, the mechanisms of crystal-liquid-amorphous (record) and amorphous-crystal (erase) phase changes in $Ge_2Sb_2Te_5$ and GeTe are proposed by the schematic presentation of fig. 2.11 [Koh06]. In the crystal-liquid phase-change process (stage I), the atomic configuration of the crystal is disarranged by the laser heating and melted in liquid, where there is no significant structural difference between $Ge_2Sb_2Te_5$ and GeTe. Meanwhile in the liquid-amorphous phase-change process (stage II), only even-numbered rings are constructed in a-$Ge_2Sb_2Te_5$ whereas a-GeTe exhibits various size (both odd- and even-numbered) rings due to the formation of Ge–Ge homopolar bonds. During the crystallization (stage III), a-$Ge_2Sb_2Te_5$ can transform to the crystal phase with only the transformation of the large-size even-numbered (8-, 10-, 12-fold) rings to NaCl-type structure (4- and 6-fold rings) with forming Ge/Sb–Te bonds and without breaking bonds. On the contrary, in the case of *a*-GeTe the recombination of the various size rings occurs by the breaking of Ge–Ge homopolar bonds and by the forming of Ge–Te bonds. Thus the construction of odd-numbered rings, induced by the formation of Ge–Ge homopolar bonds in *a*-GeTe, disturbs the fast crystallization of the amorphous phase, whereas the addition of Sb atoms to GeTe effectively prevents the formation of Ge–Ge bonds in *a*-$Ge_2Sb_2Te_5$.

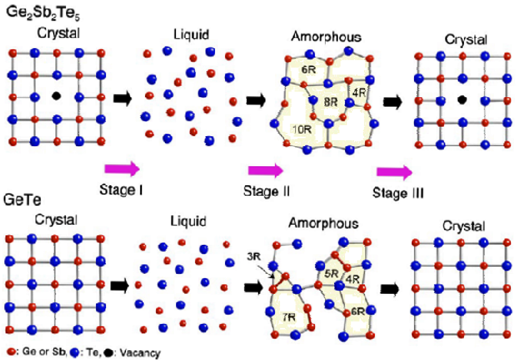

Figure 2.11 Schematic presentation for the possible ring size transformation in crystal-liquid-amorphous and amorphous-crystal phase change in $Ge_2Sb_2Te_5$ and GeTe, according to the Kohara model. The red colored bond represents the Ge–Ge bond [Koh06].

Though this scheme is simple and straightforward, experimental observations do not lend sufficient support to it. In fact the presence of Ge-Ge, Ge-Sb, Te-Te wrong bonds has been subsequently verified also in a-$Ge_2Sb_2Te_5$. Based on the current state of structure assessments, it is known that both the amorphous and the crystalline phase share structural features such as AB-alternation and preferentially octahedral coordination (see chapter 1). To a first approximation, the amorphous phase represents a strongly distorted copy of the crystalline phase. One might suspect that only a small change in structure is required upon crystallization, that is the reduction of the strong distortions. The erasure of “wrong bonds” and the tetrahedral portion of Ge-atoms appears to be the most significant rearrangement and likely impedes fast crystallization. As shown by Kohara, the evolution of the amorphous phase upon crystallization can be described in terms of the ring statistics. More detailed molecular dynamics calculations were performed on $Ge_2Sb_2Te_5$ by Hegedus and Elliott, simulating a whole phase-change cycle, that is melt-quenching and subsequent re-crystallization [Heg08]. Very high densities of connected square rings, characteristic of the metastable rocksalt structure, form during the melt cooling and are also quenched into the amorphous phase.

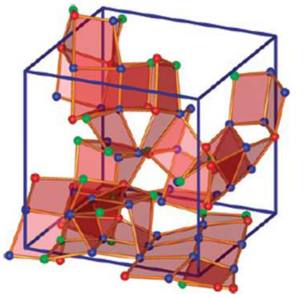

Figure 2.12 $Ge_2Sb_2Te_5$ transient near-regular connected four-fold rings (building blocks of the metastable rocksalt crystal structure) for a liquid configuration at 800°C. Color coding of atoms: Sb, red; Ge, green; Te, blue.

From this, the time-resolved evolution of wrong bonds and near-regular fourfold rings (i.e., near-planar, near-rectangular four-fold rings) was simulated during the subsequent heating. Crystallization leads to a decrease in the concentration of wrong bonds and simultaneously, the concentration in the number of the near-regular four-fold rings increases. Thus, a concise model of the phase transition in $Ge_2Sb_2Te_5$ is obtained. As an example, transient near-regular connected four-fold rings for a liquid configuration at 800°C are shown in fig.2.12. Very large, rather ordered crystal seeds appear even about 180°C above the melting point. Note the large near-planar structure (11 in-plane connected four-fold rings) at the bottom of the simulation box for this transient configuration. It is important to stress that this connected cluster of 11 four-fold rings alone contains about 30% of all the atoms in the simulation box, meaning that, in the high-temperature liquid phase of $Ge_2Sb_2Te_5$, a large fraction of atoms can participate in such a crystal seed. As a consequence, quenching this configuration, the amorphous phase will contain a large amount of subcritical crystalline nuclei and this feature can explain the peculiar crystallization kinetics of phase change materials. A similar behavior is then expected along the entire GeTe-Sb_2Te_3 pseudo-binary line. Just the amount of wrong bonds and the ring distribution should change on stoichiometry.

2.3 Polymorphism, capping, volume and doping effects

The crystallization kinetics of phase change materials is affected by several phenomena that we discuss briefly in this paragraph. It is known that the degree of short range order in amorphous solids depends on the sample processing (i.e. polymorphism). For a given alloy composition, different amorphous states exist with a crystallization kinetics depending on their structure. The knowledge of the structure is therefore a crucial issue for its relevance in the subsequent crystallization rate. Differences in the crystallization velocity between as deposited, relaxed, melt quenched and ion implanted amorphous samples have been reported [Khu00][Rao09] [Iel09][Deb08b]. In particular, both melt quenched and ion irradiated amorphous GST and GeTe show a faster crystallization with respect to the as deposited film. This difference is likely to be related to a variation of the structure of the amorphous state and a detailed investigation of the local order variation is needed to get insights into the microscopic mechanism governing this phase transition. Our contribution to this topic will be discussed in paragraphs 3.6 and 4.4. Here we show just an example of the effect of laser and ion irradiation on the crystallization of $Ge_2Sb_2Te_5$. Table 2.3 shows a comparison between the crystallization kinetics data of various amorphous states, namely, as-deposited, melt-quenched, and primed [Khu00]. This study shows that the melt-quenched amorphous film, obtained by laser irradiation starting from the crystalline phase, has a shorter crystallization onset time and a higher crystallization rate in comparison with the as-deposited amorphous film.

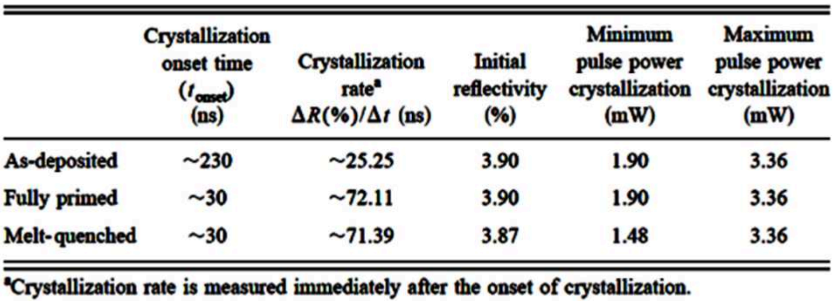

	Crystallization onset time (t_{onset}) (ns)	Crystallization rate[a] $\Delta R(\%)/\Delta t$ (ns)	Initial reflectivity (%)	Minimum pulse power crystallization (mW)	Maximum pulse power crystallization (mW)
As-deposited	~230	~25.25	3.90	1.90	3.36
Fully primed	~30	~72.11	3.90	1.90	3.36
Melt-quenched	~30	~71.39	3.87	1.48	3.36

[a]Crystallization rate is measured immediately after the onset of crystallization.

Table 2.3 Comparison of the crystallization behavior of different amorphous $Ge_2Sb_2Te_5$ samples: as deposited, melt quenched and primed. Laser irradiation induces an enhancement of the crystallization kinetics [Khu00].

Moreover variable priming leads to crystallization behavior falling between that of the as-deposited and melt-quenched states. Priming is achieved by laser irradiation, without crystallization, of as deposited amorphous layer. A qualitative model of the modification in crystallization behavior due to priming is given based on the notion that priming produces crystalline embryos which hastens crystallization process.

Also ion irradiation is able to induce a local rearrangement of the amorphous network. This phenomenon is related to the energy released inside the material by the impinging ions during the collision cascade. Figure 2.13 shows time resolved reflectivity measurements performed on as deposited and ion implanted amorphous $Ge_2Sb_2Te_5$. Ion irradiated film, implanted at several fluencies, exhibits a shorter lag time before crystallization during isothermal annealing (122°C) [Deb08]. This behavior is related to a ion induced rearrangement of the bonds distribution in the amorphous structure. It is important to note that the effect of laser and ion irradiation on the crystallization kinetics of $Ge_2Sb_2Te_5$ is the same observed in stoichiometric GeTe. A unique reading of this topic will be discussed in paragraph 4.4.

As we pointed out in paragraph 2.2.2, the crystallization of an amorphous mark embedded in a crystalline layer proceeds starting from the rim if the phase change material exhibits a growth-dominated crystallization (e.g. GeTe). Obviously it depends also on the dimensions of the mark.

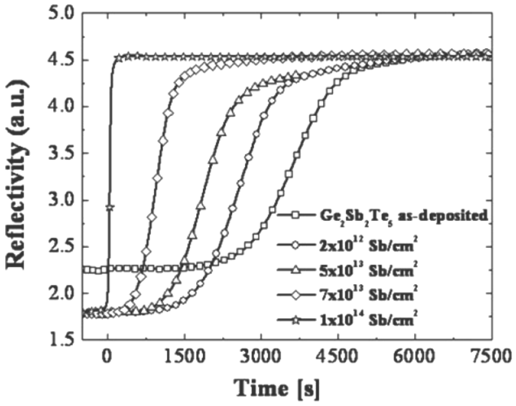

Figure 2.13 Reflectivity versus annealing time in as-deposited amorphous and ion irradiated amorphous films. The samples were annealed, after a constant heating rate, at 122 °C [Deb08].

Fast crystallization can be achieved since nucleation is not required but a lower stability of the amorphous phase (i.e. data retention) is expected. This issue will be detailed in paragraph 3.4. Here we report the crystallization of an amorphous Ge_4Te_6 mark in comparison with the data of the as deposited film, fig. 2.14. In the first case the crystallization time is much lower since nucleation of the crystalline phase is not required. It appears clear looking to both the power-time-effect curves and to the time resolved reflectivity measurements [Rao09].

The crystallization of chalcogenide thin films (~50nm) is often characterized by a heterogeneous nucleation at the interface between the material and the cover layer. Moreover, the thickness of the film affects the dimensionality of the phase transition and then it can improve the stability of the amorphous phase. The interfacial free energies of the phase change-cap interfaces play an important role during the crystallization, especially for thinner films. The optimum thickness for fastest crystallization times is the consequence of the optimization of the interfaces so as to decrease the crystallization barrier. On the other hand heat diffusion must be taken into account during the planning of a memory device. It is then possible to tune the properties of a phase change alloy by the proper choice of the capping layer and of the film thickness [Che09].

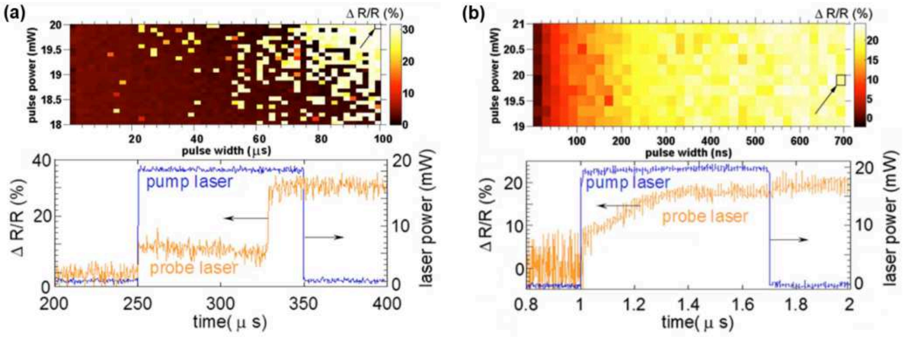

Figure 2.14 (a) Δ*R*/*R* as a function of laser power and duration for a single-pulse experiment on amorphous, as deposited Ge_4Te_6. Arrow points to the laser spot shown in the bottom panel where Δ*R*/*R* is plotted as function of time. (b) The same experiment was also performed on a melt quenched amorphous mark. The crystallization time is smaller [Rao09].

Figure 2.15(a) shows the crystallization time of 10nm as deposited amorphous $Ge_2Sb_2Te_5$ varying the cover layer. The part (b) reports the crystallization temperature (T_x) as function of the GST thickness. The change in T_x is particularly large when the thickness is less than 10 nm. In capped film, a higher crystallization temperature is coupled with a lower phase-change kinetics. Both the crystalline phases (i.e. rock-salt and hexagonal) are taken into account.

To improve the cyclability of phase change materials and to increase the crystallization temperature—of interest for applications in which high temperature data retention is required—doping of oxygen, nitrogen, and other chemical species, in the concentration range of at least a few atom percent, has been adopted [Pri04] [Pri07]. The doping with Bi or Sn lowers, instead, the transition temperatures and allows an ultrafast recrystallization (10 ns) [Wan07]. Some of the chemical bonds are expected to change toward stronger or weaker covalent bonds if the doping species are more (N, O) or less (Bi, Sn) covalent than Ge-Sb-Te, respectively, and the crystallization temperature increases with the strength of the bonds.

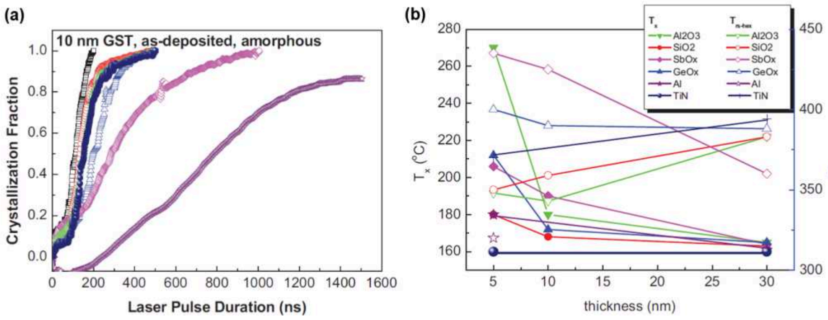

Figure 2.15 **(a) Crystallization fraction as a function of laser pulse duration for 10 nm as-deposited amorphous GST with different capping materials. (b) Crystallization temperature and rocksalt to hexagonal transition temperature as a function of film thickness [Che09].**

Doping has been performed during the deposition of the films by cosputtering or after by direct ion implantation. Privitera for example studied the amorphous-to-crystal transition through in situ resistance measurements in $Ge_2Sb_2Te_5$ thin films doped by ion implantation with nitrogen, oxygen or fluorine at different concentrations, fig. 2.16 [Pri07]. Enhancement of the thermal stability has been observed in O and N amorphous doped samples. Larger effects have been found in the case of nitrogen doping. On the contrary, doping with Fluorine produced a decrease in the crystallization temperature. The direct doping by ion implantation, in view of the required high concentration, implies low energy and fluence in excess of 10^{15} ions/cm^2. Usually the thickness of the chalcogenide films is in the order of 10–50 nm and then, for these fluence-energy combinations, preferential sputtering is expected to play a relevant role with changes in the film stoichiometry and thickness. It follows that, in the absence of a capping layer, a variation in the stability of the amorphous phase is expected because it is known that the crystallization temperature of the alloy depends on the stoichiometry and thickness of the film.

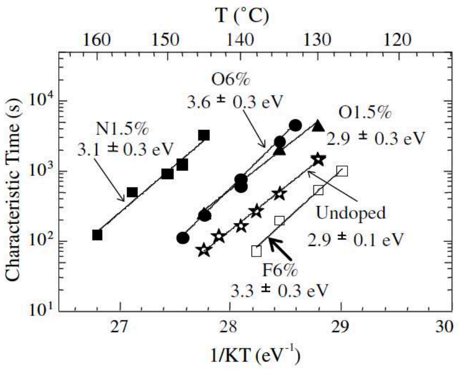

Figure 2.16 Crystallization time (τ), as function of temperature, in doped $Ge_2Sb_2Te_5$ films. The atomic percentage and the activation energy for τ are reported [Pri07].

A method to avoid the modification occurring during high fluence implantation could be the use of a cap layer although other effects due to the recoil implantation that affect the film stability must be evaluated first. This topics will be detailed in sect. 3.6.4.

References

[Avr39] M. Avrami, *J. Chem. Phys.*, 7, 1103-1112 (1939).

[Bec35] R. Becker, W. Doring, *Dampfen. Annalen der Physik*, 24, 719 (1935).

[Bru35] D. A. G. Bruggeman, *Ann. Phys. Leipzigd*, 23, 636 (1935).

[Che09] H.Y. Cheng, S. Raoux, B. Muñoz, J. L. Jordan-Sweet, *Non-Volatile Memory Technology Symposium*, (2009)

[Coo95] J. Coombs, A. Jongenelis, W., Vanesspiekman, B. Jacobs, J. Appl. Phys., 78, 4918 (1995).

[Deb08] R. De Bastiani, Crystallization and Ion Beam Induced Amorphization of $Ge_2Sb_2Te_5$ thin films, Doctoral thesis, University of Catania (2008).

[Deb08b] R. De Bastiani, A. M. Piro, M. G. Grimaldi, E. Rimini, G. A. Baratta, G. Strazzulla, *Appl. Phys. Lett.*, **92**, 241925 (2008)

[Ger79] P. Germain, K. Zeliama, S. Squelard, J. C. Bourgoin, A. Gheorghiu, *J. Appl. Phys.*, 50, 6986 (1979).

[Heg08] J. Hegedus, S. R. Elliott, *Nature Materials*, *7*, 399 (**2008).**

[Iel09] D. Ielmini, M. Boniardi, *Appl. Phys. Lett.*, **94**, 091906 (2009).

[Joh39] W. Johnson, R. Mehl, *Trans. Amer. Inst. of Mining, Metallurgical and Petroleum Engineers*, 135, 416 (1939).

[Kal04] J. Kalb, F. Spaepen, M. Wuttig, *Appl. Phys. Lett*. 84, 5240 (2004).

[Kal05] J. Kalb , C. Y. Wen, F. Spaepen, H. Dieker, M. Wuttig *J. Appl. Phys.* 98, 054902 (2005).

[Kal06] J. A. Kalb, Crystallization kinetics in antimony and tellurium alloys used for phase change recording, Doctoral thesis, RWTH Aachen University (2006).

[Kal08] J. A. Kalb, *Phase Change Materials Science and Applications*, chap. 7, Springer (2008).

[Khu00] P. K. Khulbe, E. M. Wright, M. Mansurpir, *J. Appl. Phys.*, **88**, 3926 (2000).

[Koh06]S. Kohara, K. Kato, S. Kimura, H. Tanaka, T. Usuki, K. Suzuya, H. Tanaka, Y. Moritomo, T. Matsunaga, N. Yamada, Y. Tanaka, H. Suematsu, M. Takata, *Appl. Phys. Lett.*, *89*, 201910 (2006).

[Kol04] A. V. Kolobov , P. Fons , A. I. Frenkel , A. L. Ankudinov , J. Tominaga , T. Uruga , *Nature Materials*, *3*, 703 (2004).

[Kol37] A. N. Kolmogorov, *Izv. Akad. Nauk SSR Ser. Fiz. Mat. Nauk*, **3**, 355 (1937).

[Len11] D. Lencer, M. Salinga, M. Wuttig, *Adv. Mater.*, *23*, 2030–2058 (2011).

[Pie08] L. van Pieterson, *Phase Change Materials Science and Applications*, chap. 5, Springer (2008).

[Pri04] S. Privitera, R. Zonca, and E. Rimini, *Appl. Phys. Lett.*, **85**, 3044 (2004).

[Pri07] S. Privitera, E. Rimini, C. Bongiorno, A. Pirovano, and R. Bez, *Nucl. Instrum. Methods Phys. Res.*, **257**, 352 (2007).

[Rao09] S. Raoux, H.-Y. Cheng, M. A. Caldwell, H.-S. P. Wong, *Appl. Phys. Lett.*, **95**, 071910 (2009).

[Rui02] G. Ruitenberg, A. K. Petford-Long, R. C. Doole, *J. Appl. Phys.*, 92, 3116 (2002).

[Tur49] D. Turnbull, J. Fisher, *J. Chem. Phys.*, 17, 71-73 (1949).

[Wan07] K. Wang, C. Steimer, D. Wamwangi, S. Ziegler, M. Wuttig, J. Tomforde, W. Bensch, *Microsyst. Technol.*, **13**, 203 (2007).

[Voh26] M. Vohner, A. Weber, *Zeitschrift fur Physikalische Chemie,* 119, 277 (1926).

Chapter 3

Phase transitions in $Ge_2Sb_2Te_5$

GeSbTe alloys belong to the pseudo binary line between GeTe and Sb_2Te_3. It was the 1987 when Yamada *et al.* suggested the use of these chalcogenides as active medium in optical rewritable disks [Yam87]. Looking to the phase diagram of fig. 3.1, all the three stoichiometric phases $Ge_1Sb_4Te_7$, $Ge_1Sb_2Te_4$ and $Ge_2Sb_2Te_5$ (GST) have been largely investigated during these years [Abr65]. The characteristics of the different phases have been discussed in the previous chapters. We have focused our attentions on the $Ge_2Sb_2Te_5$ alloy since it seems to have the best combination of electrical, optical, and phase changing properties. In this chapter we will discuss our studies on the local order and on the crystallization kinetics of this material looking to both the low temperature ($T \approx 150°C$) and the high temperature crystallization regime ($T \approx 500°C$), par. 3.3. and 3.5.

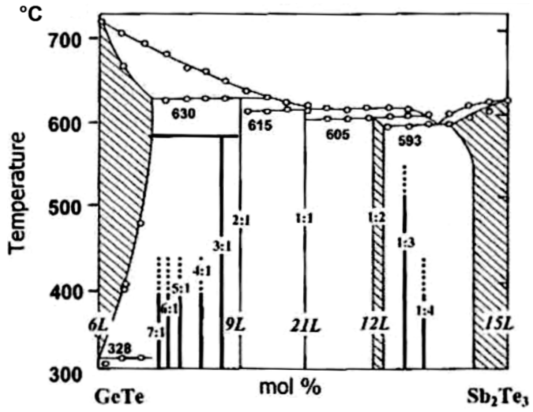

Figure 3.1 **GeTe-Sb2Te3 pseudo binary phase diagram. Three stoichiometric alloys are possible, 2:1, 1:1, 1:2 [Abr65].**

We have also studied the recrystallization process of partially amorphized thin films focusing our attention on the role of the amorphous-crystal interface. These samples have been prepared by low energy (40keV) Ge^+ ion irradiation of crystalline films whereas the recrystallization has been obtained by thermal annealing near the glass transition temperature. Transmission electron microscopy measurements were performed to detail the phase transition process, par. 3.4. The possibility to modify the properties of phase change materials by ion irradiation has been investigated in par. 3.6. We have studied the effect of ion irradiation on the amorphous phase. Differences on the local order and then on the crystallization kinetics have been detected after irradiation of the as deposited thin films. A comparison with the case of melt quenched amorphous is also presented. On the other hand, we have also demonstrated that is possible to dope chalcogenide thin film performing ion irradiation on a capped film. The capping layer can be selected to introduce by recoil implantation suitable doping species.

First of all we will discuss the characteristic of as deposited GST thin film: thickness, composition and local order.

3.1 Sample preparation

Radio frequency (rf) magnetron sputtering was used to deposit $Ge_2Sb_2Te_5$ layers from a stoichiometric target. The purity of the target used was 99.99%. Ordinary silicon wafers, covered with thermally grown SiO_2, were used as substrates. The chamber was pumped down to a pressure less than 10^{-8} mbar before the deposition. An Ar gas with a 99.999% purity was used as the sputtering gas. The target was pre-sputtered for 5-10 minutes before the deposition. The films were deposited onto substrates nominally at room temperature. The substrate was rotated continuously to ensure a constant thickness of uniform composition over a 5” area. The samples were prepared without any additional cap layer and then natural oxidation occurs after the sputter process. Films of different thickness, according to the experimental requirements, can be prepared varying the deposition time. The stoichiometry and thickness of as deposited films were evaluated by 2.0 MeV He^+ Rutherford backscattering spectrometry using a HVEE coaxial Cockroft–Walton Singletron accelerator. The scattering geometry is the IBM and refers to the case where the incident beam, surface normal, and detected beam are all coplanar, the scattering angle is 165°. Under these conditions, in normal incidence configuration, is not possible to distinguish between Sb and Te signals since the small difference in the atomic mass implies a similar kinematic factor (K_{Sb}=0.439 and K_{Te}=0.442) and then the energy separation between Sb and Te edges is smaller than the energy resolution. The Sb/Te concentration ratio was then estimated measuring the K_α peaks' intensities of the X-ray emitted during irradiation with a 2.7 MeV He^+ ion beam (PIXE).

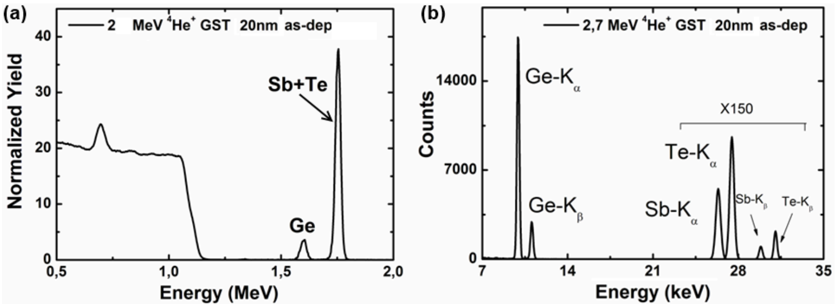

Figure 3.2 RBS (a) and PIXE (b) spectra of as deposited 20 nm $Ge_2Sb_2Te_5$ film. Thickness and stoichiometry are in agreement with the values expected.

Figure 3.2(a) shows the RBS spectrum of an as deposited 20nm thick GST film. The peak at high energy is the overlap of the signals from Sb and Te, whereas that at low energy is due to the backscattering from Ge atoms, according to the different kinematical factors. The low energy spectrum is due to the SiO_2/Si substrate. The area of each peak is proportional to $Z^2 \cdot N$, where Z is the atomic number and N is the atomic species concentration for unit area. In our spectra the statistical error (i.e. $\Delta N/N$) is of the order of 1%. A density ρ of 5.85 g/cm^3 (i.e. 3.1×10^{22} at/cm^3) is assumed to determine the thickness of the film (i.e. N/ρ). These values have been verified by the comparison between RBS measurements and transmission electron microscopy cross-sectional images. The X-ray spectrum resulting from PIXE analysis of the same sample, shown in fig. 3.2(b), states that the Te/Sb ratio remains close to the stoichiometric value of 2.5, characteristic of $Ge_2Sb_2Te_5$. The area of each peak is proportional to the cross section, to the detector efficiency, and to the concentration of the atomic species. Samples with different thickness have been prepared according to the different experimental requirements. In the next sections this feature will be specified.

3.2 Local order of the as deposited amorphous phase

As deposited samples have been characterized by extended X-ray absorption fine spectroscopy (EXAFS) and Raman spectroscopy to get insights into the amorphous network. In particular the coordination number of the different atomic species and the corresponding bond lengths have been measured. A deeper understanding of the correlation between local order and crystallization has been obtained by the merge of our data with the existing literature.

3.2.1 EXAFS analysis

I will precede the discussion of the experimental results by a short description of the physical principles underlying the EXAFS technique. The EXAFS relies on the measurement of the oscillations of the X-ray absorption coefficient at an energy higher than the absorption edge.

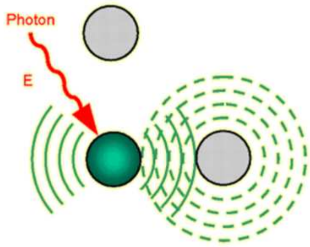

Figure 3.3 **Schematic representation of the EXAFS phenomenon.**

These oscillations are due to modification of the final state of the photoelectron by the interaction with the atoms surrounding the excited atom [Lee81][Dac11]. A schematic representation of the phenomenon is shown in fig.3.3. Outgoing photoelectron waves (solid lines), created by a photon of proper energy, propagate to the neighboring atoms. The backscattered waves (dashed lines) modify the wave function at the excited atom and give rise to EXAFS oscillations. In the case of amorphous materials, a single scattering short range order theory is adequate to describe the phenomenon. The normalized oscillatory part ($\Delta\mu/\mu_0$) of the absorption coefficient can be described by the following equation in the case of *s* state excitation

$$\chi(k) = \frac{\Delta\mu}{\mu_0} = -\sum_j \frac{N_j}{kr_j^2}\left|f_j(k)\right| \cdot \sin\left[2kr_j + \psi_j(k)\right] \cdot e^{-\sigma_j^2 k^2} \cdot e^{-2r_j/\lambda_j}$$

where N_j is the number of neighboring atoms located at a distance r_j from the excited atom. The photoelectron wave vector k is equal to

$$k = \hbar^{-1}[2m(E - E_0)]^{1/2}$$

where E is the X-ray energy, E_0 the absorption edge, m the electron mass, and $\hbar$ the Plank constant divided by π. The backscattering amplitude f is modulated by the sinusoidal term. The electron wave will be phase shifted by $2kr_j$ by the time it makes the return trip to the neighbor. The total phase function ψ_j takes into account both the phase shift due to the backscattering and the phase shift due to the interaction with the photoexcited atom. Thermal vibrations dump the EXAFS oscillations and this can be accounted by the Debye-Waller term. Moreover, electrons that suffer inelastic collisions are not able to contribute to the interference process and the second exponential term describe this phenomenon (i.e. λ is the mean free path). During the fitting procedure we have measured r_j, N_j and σ_j. The data have been extracted by the ATHENA code and fitted in k space by the ARTEMIS code using theoretically calculated EXAFS signals[Rav05]. These signals were calculated by the FEFF8.4 code using an atomic clusters model [Reh91]. More details will be discussed below. EXAFS measurements were performed at the GILDA-CRG beam line at the European Synchrotron Radiation Facility since an energy tunable and very bright X-ray source is required to obtain a high signal to noise ratio [Dac98]. X-ray energy is selected by a monochromator. It was equipped with a pair of Si(311) crystals and was run in dynamically focusing mode. Harmonic rejection was achieved by using a pair of Pd-coated mirrors. The intensity of the incoming X-ray beam was measured with a N_2-filled ion chamber whereas the fluorescence of the different atomic species was measured at room temperature with a 13-element hyperpure germanium detector. The samples were mounted on a dedicated holder for grazing-incidence geometry.

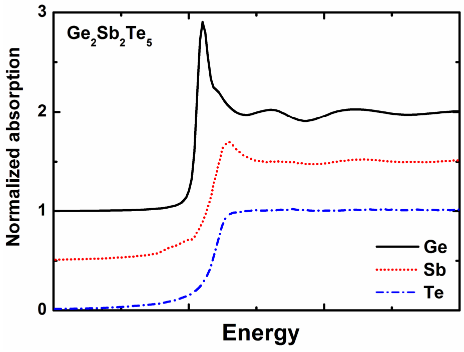

Figure 3.4 X-ray normalized absorption spectra for all three atomic species (Ge, Sb and Te), shifted in energy for comparison.

We measured the K edges of Ge, Sb, and Te and four spectra per sample were collected in order to improve the signal-to-noise ratio. The sample's thickness is 50nm. Figure 3.4 reports the spectra collected on the different atomic edges. Due to the different atomic number EXAFS oscillations appear more intense in the case of Ge edge. In the following we will describe the processing of the spectra using this spectrum as an example. The first step is the determination of the absorption edge (E_0): this is defined by the maximum in the first derivative of the absorption coefficient vs photon energy curve. The background subtraction coupled with normalization is the second point, fig. 3.5(a). EXAFS oscillations are then extracted and can be plotted as function of k, fig. 3.5(b). A window is chosen to extrapolate the significant part of the spectrum.

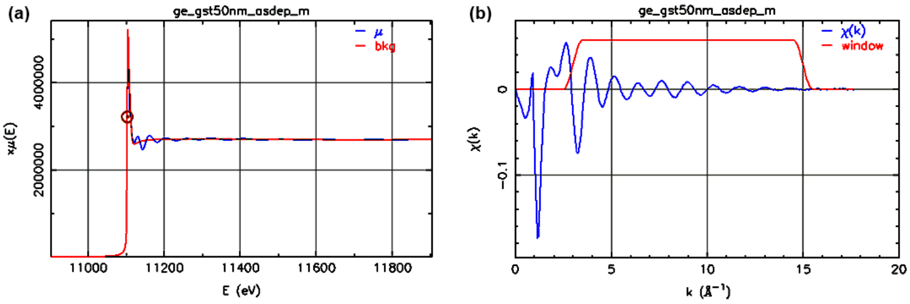

Figure 3.5 (a) Ge X-ray absorption coefficient as function of photon energy. The red line refers to the background subtraction. (b) EXAFS oscillations as function of the photoelectron wave vector. The red line indicates the Fourier transform window.

The amplitude of the EXAFS oscillations is exalted by the use of a k^3-weighted plot, fig. 3.6. All these operations are realized by the ATHENA code.

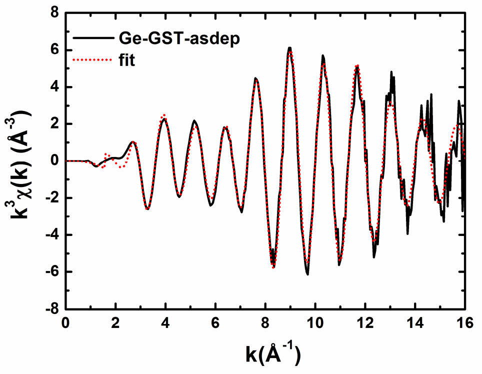

Figure 3.6 The k^3-χ plot of the Ge-edge, obtained starting from the spectrum of fig. 3.5(b), is shown coupled with the corresponding fit curve. The fitting parameters are reported in table 3.1.

Another program is required to realize the fitting procedure: ARTEMIS. The first operation is the creation of an atomistic model of the structure under investigation. The corresponding crystalline phase is generally a good starting point. The ARTEMIS program tries a fit of the experimental spectrum using as free parameters the coordination number (N_j), the bond length (r_j) and the Debye-Waller factor (σ_j), fig. 3.6. As we will discuss below, a fine agreement between experimental and simulated spectra can be achieved. A useful representation of the data can be obtained performing the Fourier transformation (FT) of the k^3-χ plot, fig.3.7. In the real space the different coordination shells are generally visible but in this GST as deposited sample only the first shell is evident. The relative abundance of the different bonds can be distinguished looking to the intensity of the corresponding peaks.

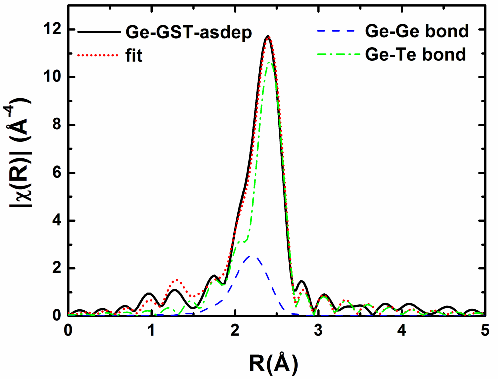

Figure 3.7 **The Fourier transform of the k^3-χ plot, reported in fig.3.6, is plotted together with the fit curve (red dotted line) and with the contributions from Ge-Ge (blue dashed line) and Ge-Te bonds (dash-dot green line).**

The FT exhibits a peak just above 2.4 Å and a shoulder at 2.2 Å denoting the presence of two types of bonds around Ge. In fact, according to Baker *et al.* [Bak06], both Ge-Ge and Ge-Te bonds are required to fit the data. It is important to note that the values of the bond lengths cannot be obtained looking to this representation since the total phase function (ψ_j) affects the position of the EXAFS oscillations. It must be noted that the similarities in photoelectron backscattering of Sb and Te render quite difficult to differentiate between Ge-Sb bonds and Ge-Te bonds in the EXAFS data. However, we have collected spectra even at the tellurium and antimony edges and, according to [Jov08], we can affirm that both Ge-Sb and Ge-Te bonds are present in the amorphous network. The Ge coordination number of the as deposited material resulted 3.4±0.6 with a Ge-Ge bond fraction of 0.9±0.3, in good agreement with the previous EXAFS analyses, in which the Ge coordination ranged between 3.5 and 3.9, and with recent theoretical calculations [Sos11]. The excellent agreement between the FT of the EXAFS signal (solid line) and the fit curve is evident. For clarity the contribution from Ge-Ge and Ge-Te bonds have been separated in the same figure. The fitting parameters are summarized in table 3.1. The presence of Ge-Sb and Ge-Te bonds has been confirmed by the EXAFS signal at the Sb and Te edge.

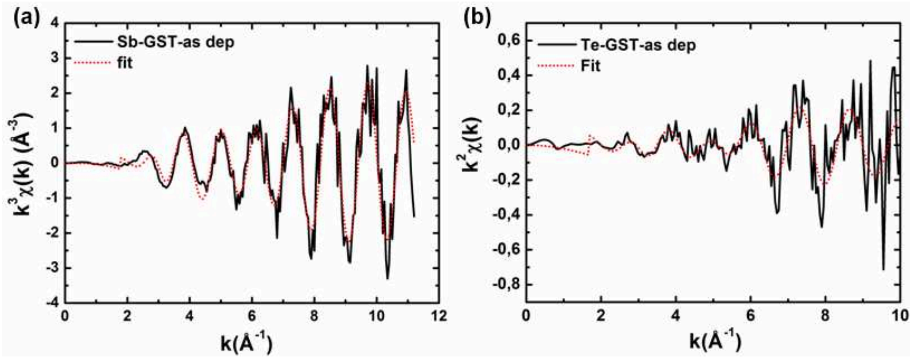

Figure 3.8 **The k-χ plots of the Sb-edge (a) and Te-edge(b) are shown coupled with the corresponding fit curve. The fitting parameters are reported in table 3.1.**

Fig. 3.8 shows the k-χ plot whereas the FTs curves are reported in fig.3.9. On the Sb edge the data have been fitted assuming the existence of Sb-Ge and Sb-Te bonds with a total coordination number of 3.0±0.6 and a Sb-Te relative coordination number of 2.0±0.3. The bond length of Sb-Ge and Sb-Te bonds is 2.68±0.05 Å and 2.86±0.02 Å, respectively. The fit of the Te edge signal required Te-Ge and Te-Sb bonds with an average total coordination number of 2±1 and a Te-Ge relative coordination number of

1.0±0.5. The bond length of Te-Ge and Te-Sb bonds is 2.63±0.02 Å and 2.85±0.05 Å, respectively. The consistency in the results is clear as the Te nearest neighbor distances were found to be the same, within the error, regardless of whether they were determined from Te-edge data or from the neighboring atom data (Sb and Ge, respectively).

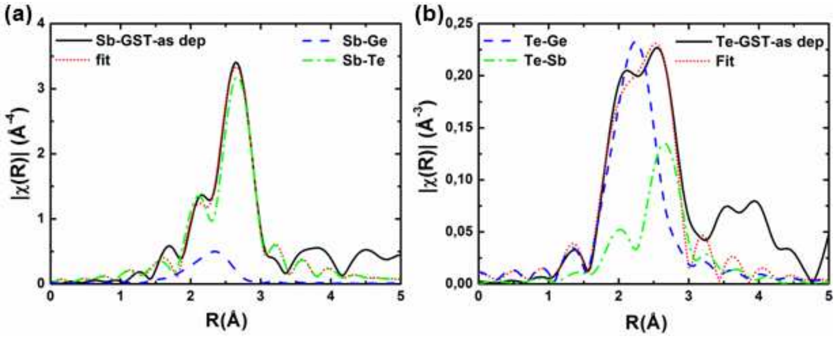

Figure 3.9 **The Fourier transform of the k^3-χ plot, reported in fig.3.8, are plotted together with the fit curve (red dotted line) and with the contributions from the different bonds.**

Our results, summarized in table 3.1, are in agreement with previous studies reported in the literature [Bak06][Jov08].

Atom	Bond	Coordination	R (Å)	σ^2 (Å^2)x10^{-3}
Ge	Ge-Ge	2.5±0.3	2.51(1)	9.0(4)
	Ge-Te	0.9±0.3	2.62(1)	5.9(4)
Sb	Sb-Ge	1.0±0.3	2.68(5)	3(2)
	Sb-Te	2.0±0.3	2.86(2)	6(2)
Te	Te-Ge	1.0±0.5	2.63(2)	5(4)
	Te-Sb	1.0±0.5	2.85(5)	12(4)

Table 3.1 **Bond lengths, coordination numbers and Debye–Waller factors measured at the different atomic edges of as deposited amorphous GST.**

As described in section 1.4.1, our analysis shows that a significative concentration of Ge-Ge and Sb-Ge “wrong bonds”, not allowed in the crystalline phase, is present in the as deposited film. Their concentration is expected to change varying the sample preparation procedure and it could influence significantly the crystallization kinetics of GST. As said before, it is not possible to distinguish by EXAFS between Sb-Te, Sb-Sb and Te-Te bonds due to the similar scattering power. Raman spectroscopy is a valid tool to overcome these difficulties as we will show in the next paragraph.

3.2.2 Raman spectrum of the amorphous phase

In this paragraph the description of the experimental results will follow a brief presentation of the Raman scattering process. The scattering of photons from atoms or molecule can occur both elastically and inelastically. In the first case, the energy of the photon is conserved after the scattering process. In the second case, part of the energy is exchanged with the vibrational modes of the irradiated system. The induced dipole moment is

$$u = \alpha \cdot E_i \cos(\omega t)$$

where α is the polarizability, E the amplitude of the electric field and ω the frequency. Since the incident light can excite molecular vibrations, the polarizability has frequency dependent contributions at the vibration frequencies ω_v

$$\alpha = \alpha_0 + \beta \cos(\omega_v t)$$

So that

$$\begin{aligned} u &= [\alpha_0 + \beta \cos(\omega_v t)] E_i \cos(\omega t) \\ &= \alpha_0 E_i \cos(\omega t) + \frac{\beta}{2} E_i [\cos(\omega - \omega_v)t + \cos(\omega + \omega_v)t] \end{aligned}$$

where the first term is the Rayleigh component at incident frequency, the second term is the Stokes component at lower frequency (i.e., the molecule absorbs energy) and the third term is the anti-Stokes component at higher frequency (i.e., the molecule loses energy). A Raman vibrational mode can be activated optically only in the presence of non-zero polarizability derivative with respect to the vibrational direction (i.e., $\beta \neq 0$). The energy of the incident photons can be then shifted up or down. Raman shift is typically expressed in wavenumbers, which have units of inverse length. In order to convert between spectral wavelength and wavenumbers the following formula is used:

$$\Delta\varphi = \left(\frac{1}{\lambda_0} - \frac{1}{\lambda_\upsilon}\right)$$

Where λ_0 is the incident photon wavelength and λ_v the Raman spectrum wavelength. Generally Raman shift is expressed in cm^{-1} and a $\Delta\varphi$=8 cm^{-1} is equal to an energy shift of 1meV. In an ideal crystal, because of the periodicity of the lattice, the vibrations are wavelike with infinite extent and a single wave vector. The light-scattering spectrum then can only show frequencies ω_v for which the mode has a wave vector k equal to the scattering vector (i.e., k≈0). This is the usual "momentum" selection rule for crystals which gives rise to the discrete set of lines seen in crystal spectra. In an amorphous material, the assumption of short correlation length, breaks the momentum selection rules since the vibrational modes cannot be characterized by a single wave vector [Shu70]. All vibrational modes can then contribute to the first-order Raman scattering and then the spectrum of an amorphous material is a measure of the density of vibrational states. It has been demonstrated that, as the coupling of the vibrations to light is not constant for all modes, Raman spectroscopy yields a “weighted” density of states, for which the weighting is not accurately known. Here we present the Raman spectra of as deposited amorphous and crystalline 50nm thick GST films. The analyses were performed at room temperature in backscattering geometry using a single spectrometer and a He–Ne laser (λ=633nm and 2 mW on the sample). The laser spot size was 6 µm in diameter and no significant heating effects were observed. Raman scattering intensity is typically very weak and to separate the inelastically peak from the intense scattered laser light an angle tunable holographic Supernotch filter (Kaiser Optical System) was used. We properly tuned the angle to permit the individuation of Raman peaks starting from 70 cm^{-1}.

Figure 3.10 shows the Raman spectra collected on the different phases of $Ge_2Sb_2Te_5$: amorphous, rocksalt and hexagonal. First of all it is interesting to note that both the amorphous and the crystalline phases don't exhibit sharp peaks. As said before, this is a common feature of amorphous materials unlike crystalline phases. In this particular case the presence of a broad peak in the crystalline phase has to be attributed to the "intrinsic" disorder of these structures discussed in paragraph 1.3.2. The corresponding interpretation of the Raman spectrum will be tackled in paragraph 3.3.3.

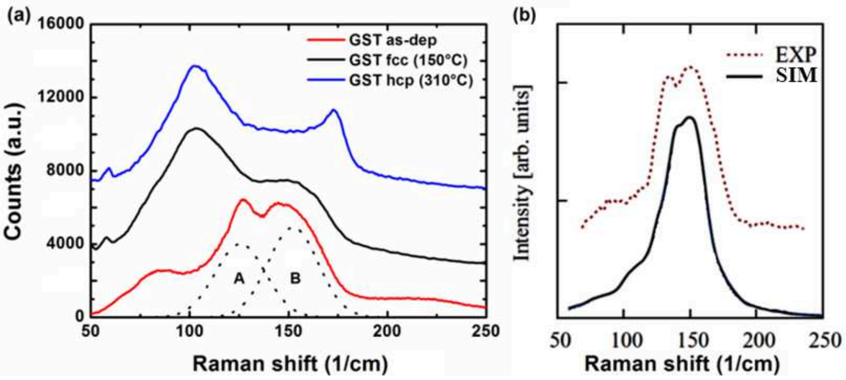

Figure 3.10 **(a) Raman spectra of amorphous (red line), rock salt (black line) and hexagonal (blue line) $Ge_2Sb_2Te_5$ thin film. (b) Comparison between simulated [ref] and measured Raman spectrum of amorphous GST [Sos11].**

In the case of amorphous GST, the interpretation of the Raman spectrum has been the object of a large debate and different models of the amorphous structure have been proposed, par. 1.4.1. The spectrum can be fitted by two main Gaussian contributions centered at ~125 cm^{-1} and ~150 cm^{-1}. According to first principles calculations both these peaks can be assigned to vibrations of defective octahedra that are the main building blocks of the amorphous network [Sos11]. In particular, they are dominated by modulations of the Sb-Te bonds which are much more polarizable than Ge-Te bonds. The projection of the Raman spectrum of a-GST on bending- and stretching-like displacements shows that the shoulder at 160 cm^{-1} is mostly due to stretching-like modes whereas the first peak is mainly related to bending-like modes. Figure 3.10(b) shows the comparison of our experimental spectrum with the calculated one in [Sos11]. We believe that even Te-Te dimers and trimers contributes to the intensity of the band at 125 cm^{-1} since it is known that crystalline Tellurium has the strongest Raman peak at 122 cm^{-1} [Pin71] and a very high Raman cross section. It turns out that Raman spectroscopy is a powerful tool to detect the presence of Te-Te bonds. These homopolar bonds, as in the case of Ge-Ge and Sb-Ge wrong bonds, are forbidden in the crystalline structure, and then their presence and abundance could influence significantly the crystallization kinetics of GST.

3.3 Crystallization near the glass temperature

The crystallization parameters (i.e. nucleation and growth) of as deposited amorphous $Ge_2Sb_2Te_5$ are reported in several papers and summarized in table 2.1 [Kal05][Kal05b]. It is known that GST is subjected to a strong variation of density upon crystallization ($\Delta\rho \approx 5\%$) [Non00]. This phenomenon induces the formation of transrotational grains characterized by an internal bending of lattice planes (i.e. elastic strain) [Koo04]. We have studied in detail the evolution of these structures during the crystallization process by X-ray diffraction (XRD) and transmission electron microscopy (TEM). The combination of these techniques makes it possible to analyze the development of transrotational crystals more thoroughly, obtaining information about the internal bending during the crystal growth. These information can be related to the crystallization process.

3.3.1 X-ray diffraction analyses

GST amorphous films, 50 nm thick, were prepared by rf sputter deposition at room temperature over a 100 nm SiO_2 layer thermally growth on silicon wafers. No capping layer was deposited. The as-deposited amorphous layers were crystallized by isothermal annealing at 122°C. The kinetics of the transition was monitored by in situ time resolved reflectivity using a low power He-Ne laser probe (λ=633 nm, 5 mW). The reflectivity increase has been converted into the crystalline fraction, f_s, by the effective medium approximation, sect. 2.2.1.

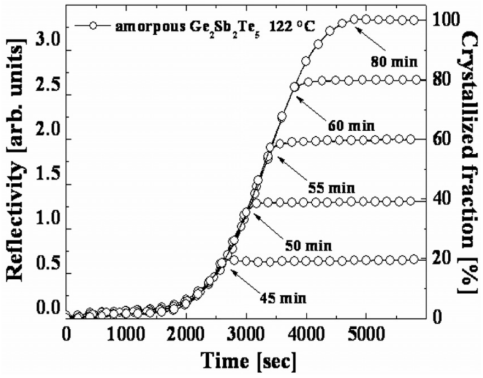

Figure 3.11 Reflectivity signal versus annealing time at 122 °C for as-deposited amorphous $Ge_2Sb_2Te_5$ films. Different amorphous samples were stopped at the annealing time indicated by the arrows to obtain different crystallized fraction.

Since the absorption length of the amorphous and crystalline GST, for λ=633 nm, is about 25 and 12 nm, respectively, the probed thickness never exceeds half of the GST film and f_S cannot be thought as a volume crystalline fraction (fig. 1.7). Several samples with f_S equal to 20%, 40%, 60%, 80%, and 100% were obtained for different annealing time in the 45–90 min range, fig.3.11. The XRD measurements were performed using a SIEMENS D5005 diffractometer operating with Cu K_α (λ=0.15406 nm) in the configuration for thin film analysis, in which the X-ray beam hits the sample surface at a grazing angle (0.5°). The position of the diffraction peaks is related to the interplanar spacing according to the Bragg law

$$n\lambda = 2d \cdot \sin\theta$$

where d, θ, n, and λ are the interplanar spacing, the angle of the lattice planes with respect to the incident X-ray beam, order of diffraction, and the wavelength of the X-ray beam, respectively. The XRD patterns of the samples with different crystalline fraction are reported in fig. 3.12. The pattern of the as deposited film shows a broad bump centered at 2σ=30° typical of the amorphous phase.

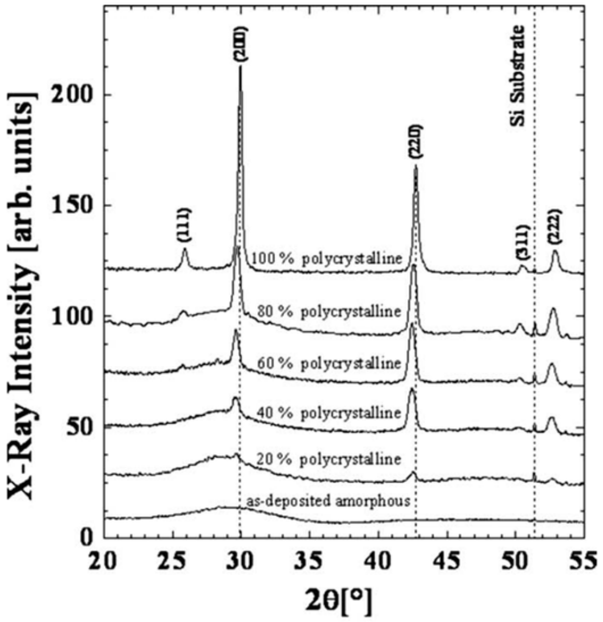

Figure 3.12 XRD of as-deposited amorphous $Ge_2Sb_2Te_5$ films at different crystalline fraction. The peaks positions related to the diffraction of (200) and (220) planes are marked with dashed vertical lines with the contribution of Si substrate.

In the partially crystallized samples, the diffraction peaks due to the (200) and (220) family planes of the metastable rocksalt phase appear, and their intensity increases with the crystalline fraction. The enhancement of the crystalline peaks is associated to a reduction of the bump of the amorphous phase until its disappearance when f_S=100%. The dashed lines identify the angular position of the (200) and (220) peaks in bulk fcc GST and these coincide with those detected in the fully crystallized film. In partially crystallized films these peaks are at smaller angles and they shift toward larger angles as the crystalline fraction increases. Such a shift is not the result of a systematic error and it is definitely greater than the error affecting these measurements as can be inferred by the position of the Si substrate peak (51.5°) that remains constant during the transition. The lattice parameter derived from XRD analyses is reported in fig. 3.13(a) as a function of crystalline fraction f_S. It starts from 6.06 Å and decreases toward the bulk value 6.01 Å at the late stage of the transformation.

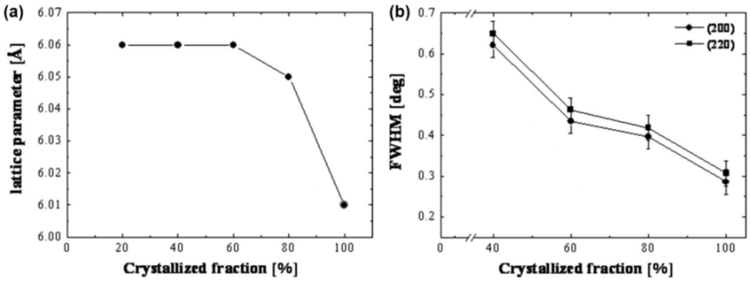

Figure 3.13 **(a) Dependence of the lattice parameter on the crystallized fraction (cubic phase). (b) Width of (200) and (220) peaks, obtained by profile fitting analysis of partially crystallized samples.**

Even the full width at half maximum (FWHM) of the (200) and (220) peaks is larger than expected, ranging from 0.65°±0.01° at 20% of surface crystallized fraction to 0.3°±0.01° at 100% fraction, fig.3.13(b). If we assume that the FWHM is only due to the small size of the crystalline grains we can evaluate the average grain diameter by the Debye-Scherrer formula

$$d = \frac{\lambda}{FWHM \cdot \cos\theta}$$

that ends up with a grain size of 40 nm for FWHM=0.3°. We have verified this estimation by TEM analyses. These measurements have been also useful to explain the behavior of the lattice parameter as function of the crystallized fraction, fig. 3.13(a).

3.3.2 Transmission electron microscopy (TEM) analyses

In order to study the morphology of our partially crystallized GST samples, transmission electron microscopy (TEM) and scanning-TEM analyses have been performed. TEM analyses, both in plan view and cross-sectional configuration, were performed using a JEOL JEM 2010F TEM/STEM equipped with a 200 kV Schottky fieldemission electron gun and an ultrahigh-resolution objective lens pole piece. Samples for plan-view images were thinned by backside mechanical lapping, followed by ion milling using a 2.5 keV Ar^+ beam incident at an angle of 8°. Under these conditions, the thinning procedure does not induce appreciable heating of the sample and consequent modifications of its structure. Samples for the cross-sectional analyses were prepared using a FEI FIB200DE focused ion beam (FIB) apparatus after deposition of a Pt layer at the sample surface to prevent damage during the FIB milling.

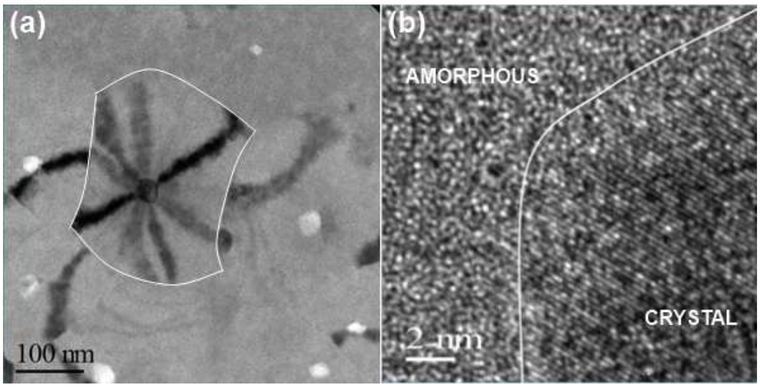

Figure 3.14 **(a) TEM image of a partially crystallized film. One of the grain boundary has been highlighted by a white line. (b) High resolution TEM image of a small "dark spot" characteristic of the early stage of the crystallization process. The boundary between amorphous and crystalline region has been highlighted.**

A typical plan view TEM image of a partially crystallized film is shown in fig. 3.14(a). The grains exhibit the typical contrast of transrotational structures characterized by dark fringes corresponding to bending contours, which move laterally by tilting the sample around axes parallel to the fringes themselves [Koo04]. Another peculiarity is the presence of "bright" or "dark" small spots (20 nm of diameter), localized at the center of each transrotational crystal grain or just surrounded by amorphous regions. They have been identified by the contrast change of TEM images during sample tilting as (dimpled) crystalline grains. A high resolution image of these structures is reported in fig. 3.14(b). Further insight into the evolution of these microstructures during crystallization can be inferred from STEM plan view micrographs of samples with f_S=20%, 40%, 80%, and 100% as shown in fig. 3.15. The analysis reveals the presence of GST crystal grains whose density and average size increase with the annealing time until their complete coalescence.

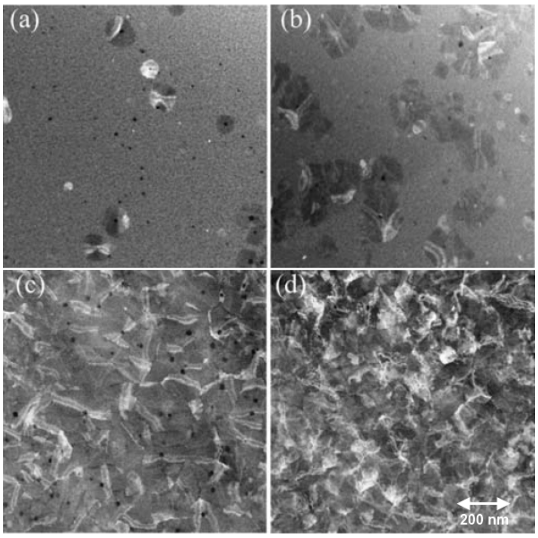

Figure 3.15 STEM plan-view micrographs of as-deposited amorphous $Ge_2Sb_2Te_5$ films, annealed at 122°C with f_S=20% (a), 40% (b), 80% (c), and 100% (d), respectively.

At about 100% the average grain size amounts to 300 nm definitely higher than that calculated using the Scherrer formula. Transrotational grains are dominant in the partially crystallized samples [figs. 3.15(a), (b), (c)] but almost disappear as f_S=100% [fig. 4(d)]. This means that at the end of the process the degree of internal bending decreases. The occurrence of the transrotational structures has been related to the different density between the crystalline and the amorphous phase. At the early stages of the transition, the crystalline clusters formed by heterogeneous nucleation at the free surface induce a local reduction of the film thickness (i.e. “dark spots”). As these crystallites grow, it is more convenient for them to bend the lattice plane at the lateral a-c interface reducing then the elastic energy due to the strain. The bending angle was estimated by measuring the shift of the dark fringe when the sample is rotated around an axis parallel to the fringe itself. The shift of the dark fringe, due to the sample rotation, is visible, for example, in fig. 3.16 in which a displacement of 59 nm occurs tilting the sample of 2.7°. An average bending angle equal to 0.05° per nanometer of lateral displacement has been measured in the partially crystallized films.

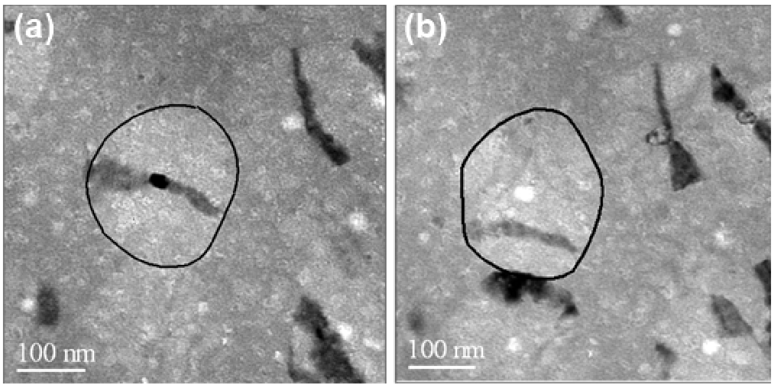

Figure 3.16 (a) TEM image of partially crystallized GST film. (b) By measuring the shift of the dark fringe when the sample is rotated around an axis parallel to the fringe itself it is possible to measure the bending angle of the crystalline grain.

To improve the description of the crystallization process we have also performed cross sectional analyses of the partially and fully crystallized samples, fig. 3.17. The sample preparation required the deposition of a Pt layer on top of GST. The partially transformed sample in fig. 3.17(a) shows a double layer structure with a crystalline surface layer over a still amorphous film. The amorphous/crystalline interface is at a depth of 25 nm, in agreement with the crystallization studies of sputtered-deposited GST films by Jeong *et al.* and Kalb *et al.* [Jeo99][Kal05]. Therefore the crystallization process starts at the free GST surface. As the crystallization further proceeds, the crystal grains grow consuming the buried amorphous fig.3.17(b) and, at the end of the transformation, the thickness of the crystallized film is reduced by 4% with respect to its initial value.

The scenario is then the following: the crystalline grains nucleate at the free surface and have a fast lateral growth giving rise to the layered structure of fig. 3.17(a). The difference between the crystalline and the amorphous density generates a strain that is accommodated by the bending of the crystalline grains. As the coalescence among the transrotational domains is complete, the crystallization proceeds in the vertical direction causing the collapse of the transrotational structure. Therefore the lattice parameter measured by X-ray diffraction in partially crystallized samples is an average value given by the semisum of the distorted lattice parameter of the top of the grain and of the bulk lattice parameter of the bottom. The knowledge of the grains angular bending and of their size, achieved by TEM analyses, allows then an independent determination of the average lattice parameter.

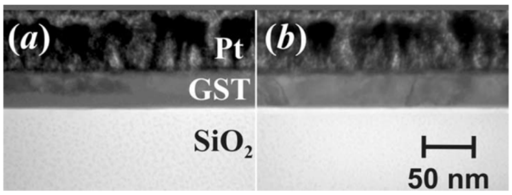

Figure 3.17 STEM cross-sectional images of samples with f_S=80% (a) and f_S =100% (b), respectively. The Pt layer on top of GST has been deposited to protect the sample during the FIB preparation.

In partially crystallized samples, with grains of about 25 nm lateral size (i.e. the half of the film thickness), it amounts to 6.07Å in good agreement with the XRD data, fig. 3.13(a). Moreover due to the bending, only a limited amounts, about 10%, of the crystalline volume contributes to the diffraction thus reducing the size of the diffracting crystal and increasing the FWHM of the diffraction peaks, fig. 3.13(b).

3.3.3 Raman spectra of the crystalline phases

In the last years, Raman spectroscopy has been proposed to analyze the structure and the corresponding vibrational properties of crystalline $Ge_2Sb_2Te_5$. As pointed out in par. 1.3.1 two possible crystalline structures exist: a metastable face centered cubic and a stable hexagonal one. A comparison between experimental and calculated [Sos11][Sos09] Raman spectra is reported in fig. 3.18(a) and (b), respectively. In the spectrum of fcc-GST we recognize two main structures, one at ~110 cm^{-1} and a second weaker at ~160 cm^{-1}.

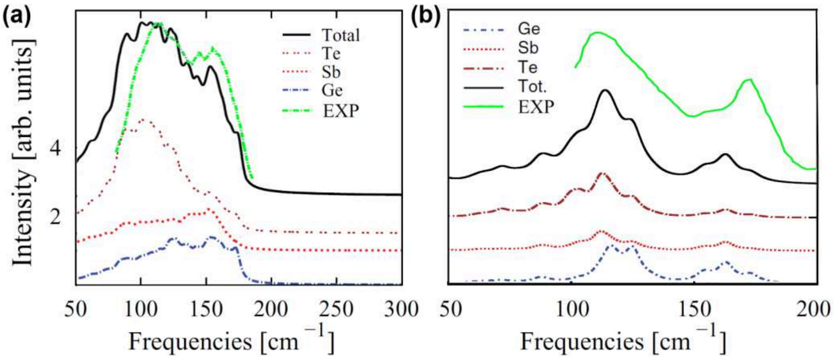

Figure 3.18 Experimental and calculated Raman spectra of rock salt (a) and hexagonal (b) $Ge_2Sb_2Te_5$. Theoretical Raman spectra are also projected on the different atomic species.

Insight on the phonons responsible for the different Raman peaks is gained from the analysis of the reduced Raman spectra projected on different types of atoms. The strongest contribution to the first peak comes out from Te atoms whereas both Sb and Ge atoms are responsible for the shoulder at 160cm^{-1}. Anyway both these peaks are due to vibrations of octahedral structures and in particular the strongest contribution is related to Sb-Te bonds. The theoretical spectrum also reproduces the fact that, as opposed to the common behavior of most materials, the Raman spectrum of the crystalline phase is broader than the spectrum of the amorphous phase, fig. 3.10. This is due to the presence of a 20% of vacancy sites in one sublattice of fcc-GST. Vacancies induce a large atomic relaxation with a broad distribution in Ge-Te and Sb-Te bond lengths, par.1.3.2. The spread in Ge-Te and Sb-Te bond lengths is larger in fcc-GST than in a-GST where, in the lack of symmetry constraints, atoms relax more easily toward the optimal length for p-type. In the hexagonal phase, fig. 3.18(b), two main contributions appear at ~110 cm^{-1} and ~175 cm^{-1}. These modes correspond to atomic displacement perpendicular and along to the c axis (normal to the hexagonal planes), respectively. Symmetry breaking due to Ge/Sb disorder makes several modes active in the Raman spectrum and induces a mixing of the displacements along and perpendicular to the c axis. The large broadening of the structure around 110 cm^{-1} is partially due to the symmetry breaking which splits the degenerate perpendicular modes. Also in this case, to easily identify the type of displacement patterns responsible for the Raman peaks, the calculated Raman spectrum is projected on Te, Sb and Ge atoms. All these atomic species contribute to the intensity of both the peaks.

Raman spectroscopy is a powerful tool to probe the local order and to distinguish between the different phase of GST (GeTe). This possibility will be largely exploited in the next paragraph and in chapter 4.

3.4 Crystallization in the presence of α-Xst interface.

The stability of the amorphous phase in presence of a crystalline substrate and the role of the amorphous-crystalline (α-Xst) interface are crucial issues for technological applications. In real devices, in fact, the erase-write cycles involve the formation of amorphous regions embedded in the crystalline matrix and the data retention capability is then related to the stability of these structures. To disentangle the effect of the a-c interface on the amorphous stability from other effects related to the nanometric size of the amorphous pocket, we have investigated the crystallization kinetics of 25nm thick continuous amorphous GST films in contact with a planar interface, with either cubic or hexagonal GST. The amorphous surface layers on top of the crystalline GST films were prepared by low energy ion irradiation. The growth of the crystalline phase, starting from amorphized layer was investigated during low isothermal annealing by in situ time resolved reflectivity measurements (TRR), X-ray diffraction (XRD), in situ transmission electron microscopy (TEM), and Raman analyses. The role played by the interface between adjacent phases has been then evaluated. $Ge_2Sb_2Te_5$ amorphous films, 50 nm thick, over a 100nm SiO_2 layer were crystallized by isothermal annealing at 150°C and 300°C for 10 min in order to obtain, respectively, the face-centered-cubic (fcc) and hcp phase. The hexagonal and cubic crystalline films were successively amorphized in the near-surface region by implantation of 28 keV Ge^+ ions at a fluence of 10^{14} ions/cm^2. The concentration profile of the implanted Ge reaches its maximum value $5x10^{19}$ cm^{-2} at a depth of 18 nm, with a straggling of 10 nm (SRIM calculation) [Zie85]. The substrate was maintained at liquid nitrogen temperature to produce a sharp a-c interface. Another sample was implanted, for comparison, with 140 keV Ge^+ ions at the same fluence in order to fully amorphize the GST film. XRD measurements were performed using a Thermo ARL X'TRA diffractometer, operating at a wavelength of 1.5418 Å (Cu K_α radiation) in the configuration for thin film analysis, in which the x-ray beam hits the sample surface at a fixed angle (4.0°) and a scan of 2θ was performed. The step size was 0.02°, the scan rate 0.06°/min. The Rietveld MAUD program was exploited to refine the X-ray data [Lut98]. TEM was performed using a JEOL JEM 2010F TEM equipped with a 200-kV Schottky field-emission electron gun, and an ultrahigh-resolution objective lens pole piece. Samples for the cross-sectional analyses were prepared using a FEI FIB200DE focused ion beam apparatus after deposition of a Pt layer at the sample surface to prevent damage during the FIB. In situ TEM analyses were performed using a Gatan 626TA single tilt heating holder equipped with a 901 SmartSet Hot Stage controller to maintain the temperature at the set-point without overshoot. The local order was inspected by micro-Raman spectroscopy. A He–Ne laser (λ=633 nm) was used as excitation source for the Raman analysis carried out in air at room temperature using a backscattering geometry. Figure 3.19 shows the XRD spectrum of GST thin films after annealing performed at 150 °C and 310 °C. Well defined XRD peaks reveal the presence of the cubic or hexagonal phase in the diffraction patterns where the labeling of the diffracting planes is reported. Crystalline layers were amorphized in the near-surface region and successively recrystallized by isothermal annealing, following the process by TRR measurements.

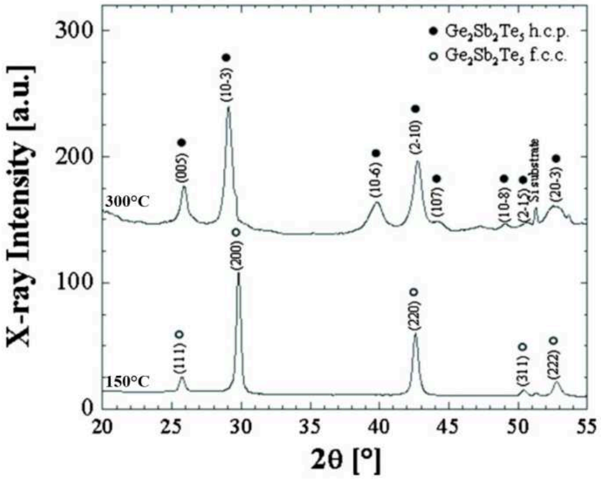

Figure 3.19 **XRD spectrum of $Ge_2Sb_2Te_5$ films after annealing at 150 or 310 °C for 10 min; the diffraction peaks indicate the presence of rock-salt (open circles) and hexagonal phase (full circles). The labeling of diffracting planes are reported.**

Figure 3.20 shows the reflectivity signal during annealing at 122 °C for a fully amorphized GST film (open triangles), partially ion amorphized layer on a polycrystalline fcc (open circles) and on hcp (open squares) films. A schematic of the samples is reported in the inset of the figure. The temperature, measured by a thermocouple adjacent to the sample, is shown in the same graph (right scale). The TRR curve of the fully amorphized film is typical of this kind of process (par. 2.2.1): the initial plateau traces the incubation time (i.e. the time to reach a steady state nucleation rate) and it is followed by an abrupt increase associated to crystallization. The initial reflectivity signal of the amorphous layer on crystalline (cubic or hexagonal) films is lower than that of the fully amorphous, due to interference effects at the amorphous/crystalline interface. The time evolution of the reflectivity signal indicates a relevant enhancement of crystallization rate. Full crystallization occurs already during the heating ramp.

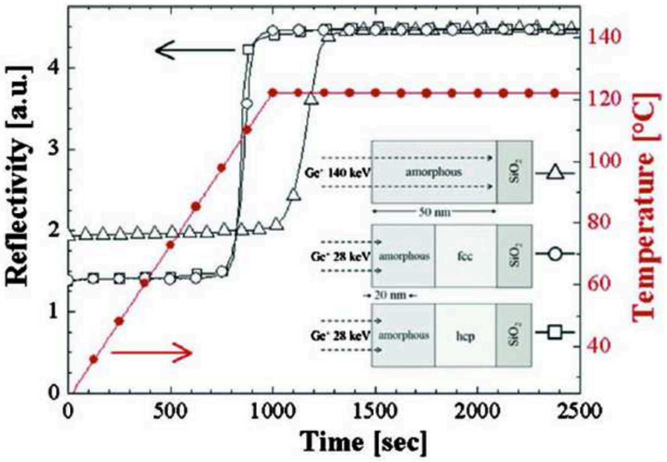

Figure 3.20 Reflectivity vs annealing time at 122 °C of ion implanted amorphous film (open triangles), implanted crystalline fcc (open circles), and hcp (open squares) films by Ge^+ ions at a fluence of 10^{14} ions/cm^2 as schematically depicted in the inset. The sample temperature was raised from RT to the set point using a ramp of 5 °C/min (red line).

This difference cannot be ascribed to the amorphous state since in all the investigated cases the amorphous layer has been formed by ion implantation. Therefore, TRR measurements unambiguously demonstrate that the crystallization rate increases in presence of an a-c GST interface, even if the details of the crystallization process cannot be defined by this technique and require microscopic analysis. For this reason we performed *in situ* TEM analyses during the annealing. Figure 3.21 shows the cross-sectional images takes at different times during the treatment at 120 °C of the sample in which the amorphous lies on cubic GST. The featureless layer at the surface of the as-implanted sample (a) is the amorphous generated by ion implantation and it is separated by a well defined interface from the underlying crystal. The thickness of the amorphous layer is ~25 nm (half of the total film thickness) in good agreement with that expected on the basis of SRIM calculation. The image of the partially crystallized sample, shown in fig. 3.21(b), indicates that the crystallization occurs through the epitaxial growth of some crystalline domains at the interface between the cubic and amorphous surface. These domains grow fast in the direction perpendicular to the a-c interface and reach the surface. The residual amorphous is then crystallized either by a lateral growth or/and by epitaxy from others crystalline domains at a lower rate. The overall effect is a coarsening of the a-c interface.

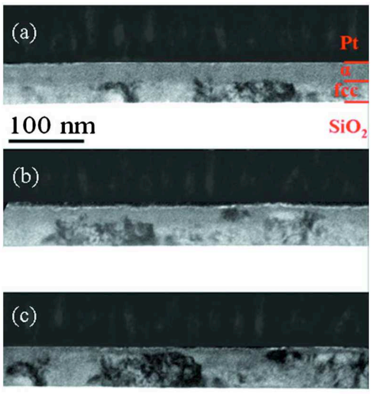

Figure 3.21 TEM cross-sectional images of the cubic GST film implanted by 28 keV Ge$^+$ ions at a fluence of 10^{14} ions/cm^2 and annealed in situ at 120 °C for different time until full crystallization. The red lines mark the different layers.

At the end of the transformation, fig. 3.21(c), the original a-c interface is not distinguishable and most of the recrystallized layer is epitaxial with the underlying pristine crystalline GST layer. Figure 3.22 shows the cross-sectional images of the amorphous on hexagonal GST film as-implanted (a) and at different times during the in situ annealing at 120 °C (b) and (c). No clear evidence of nucleation within the amorphous layer or at the a/c interface was observed; the crystallization occurs by a planar motion of the a-c interface toward the surface. The recrystallization of the amorphous layer is occasionally interrupted by amorphous pockets, between crystalline domains, that crystallize slowly by lateral movement. Moreover, after annealing the crystallized layer shows large areas with strongly inhomogeneous contrast due to a high defectiveness of crystal structures. In fact, the hexagonal phase is characterized by the presence of a large density of defects due probably to the agglomeration of lattice vacancies of the previous metastable cubic phase.

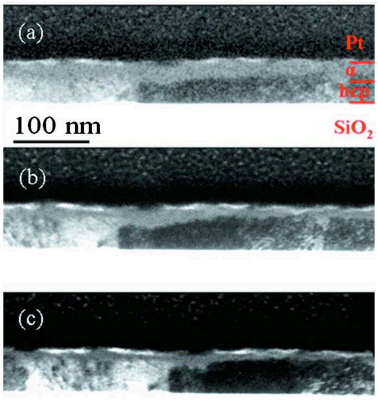

Figure 3.22 TEM cross-sectional images of the hcp GST film implanted by 28 keV Ge^+ ions at a fluence of 10^{14} ions/cm^2 and annealed in situ at 120 °C for different time until full crystallization. The red lines mark the different layers.

The short-range order of the crystalline phase grown on the cubic or hexagonal GST films, has been analyzed using micro-Raman spectroscopy. Figure 3.23 shows the Raman spectra of the crystalline GST thin films formed by annealing at 150 °C (a) and 310 °C (b), respectively. In the first case, as expected for fcc crystalline phase (par. 3.3.3), two broad peaks at 110 and 160 cm^{-1} are visible. The Raman spectrum of the sample annealed at 310°C shows two broad peaks at 110 and 175 cm^{-1} typical of the hexagonal phase. After irradiation with 28 keV Ge^+ ions (fluence of 10^{14} ions/cm^2), the Raman spectrum of both samples exhibits two well separated bands at wave number positions of ~125 and ~150 cm^{-1} typical of the amorphous phase (c) (par. 3.2.2). In fact, according to our experimental setup, the laser light is absorbed in the amorphized region without probing the underlying crystalline layer. The Raman spectra of the recrystallized α/fcc (d) and α/hcp (e) are indistinguishable and indicate the growth of the fcc phase even in presence of a hcp seed.

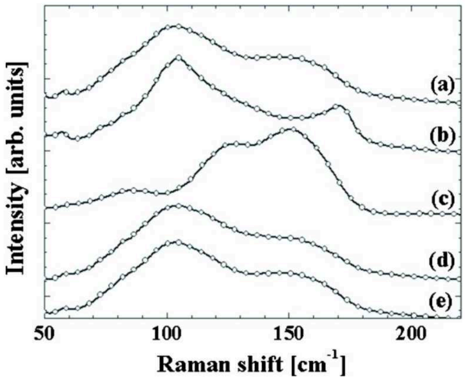

Figure 3.23 Raman spectra of cubic (a), hexagonal phase (b), and amorphous surface layer on top of the crystalline GST films (c). A He–Ne laser, able to probe the film within the amorphized thickness, was used as excitation source. The Raman spectrum of the recrystallized layer on the cubic (d) or hexagonal (e) film shows the presence of the cubic phase in both the samples.

The formation of the rocksalt phase in both cases is surprising since one would expect that the epitaxy ends up with the hexagonal phase in the α/hcp sample. To further support the Raman data we have investigated the recrystallized samples by XRD. Only fcc phase was detected in the crystallized α/fcc sample whereas hexagonal and cubic phase, with volume fractions of 68% and 32%, have been measured in crystallized α/hcp samples. In conclusion, the crystallization kinetics of amorphous thin films generated by ion irradiation was investigated by TRR, TEM, and XRD focusing on the roles played by the underlying cubic or hexagonal GST layers. By a suitable choice of the irradiation parameters a thin surface amorphous layer on top of crystalline material was obtained. In both cases thermal induced crystallization of the damaged layer was found to proceed from the interface. In both the cases the surface amorphous layer crystallizes in the cubic phase at temperatures well below those required for the crystallization in the absence of the α-fcc(hcp) interface. In particular, the recrystallized layer in contact with a hexagonal state shows a phase mainly cubic with a high defectiveness of crystal structures. The reduced stability of the amorphous phase must be ascribed to the role of the amorphous/crystal interface. This means that the data retention capability of memory devices cannot be extracted from crystallization measurements in blanket films since the a-c interface plays a crucial role also in nucleation dominated phase change materials like GST. A more realistic calculation can be performed considering both the dimension of the amorphous mark and the growth velocity of the crystalline grains neglecting then nucleation phenomena, especially if the size of the active region is on a sub-micrometric scale.

3.5 Laser induced crystallization

Despite the fact that PCRAM and optical disks are already commercially available, a remarkably high number of fundamental properties of phase change materials is still not fully understood. In particular, one of the most controversial points concerns the crystallization mechanism. It is still a challenge to explain, with a simple model, a crystallization rate that changes of more than 16 order of magnitude (from a year timescale to a nanosecond timescale!) in a restricted temperature range (~400°C) [Khu00] [Kal05b][Kal04]. A peculiar phase change mechanism could be the source of this particular behavior and several theoretical studies are reported in the literature about this topic, sect. 2.2.3. However, a clear interpretation of the phenomenon cannot be obtained until reliable experimental data on the crystallization in the different temperature regimes are not available. As discussed in sect. 2.2.2, a detailed analysis on the amorphous-crystal transition of several phase change materials near the glass transition temperature has already been reported in [Kal04][Kal05]. The direct observation of the crystals enabled establishing the temperature dependence of the nucleation rate and growth velocity near the glass transition temperature. The extrapolation of these data to higher temperature is not *a priori* meaningful. For example, assuming a simple Arrhenius dependence the growth velocity far below the melting temperature exceeds the speed of sound, which defines the maximum possible velocity for atomic rearrangements. In the case of $Ge_2Sb_2Te_5$ and AIST, the extrapolated growth velocity at 500°C is ~10^4 m/s and ~10^7 m/s, respectively! Hence, it is impossible that the growth velocity has a simple Arrhenius behavior over the entire temperature range. The origin of this peculiar feature is probably related to the characteristics of the amorphous materials undergoing the phase change. It is known that the nucleation and growth rate of the crystalline grains are inversely proportional to the viscosity (η) of the amorphous phase, par. 2.2. Therefore, for example, the growth rate versus temperature trend is expected to be influenced by the temperature dependence of η. We have discussed in par. 2.1 the viscosity of the different materials and with reference to fig. 2.2(b) we can reasonably assert that the amorphous phase of phase change materials should exhibit the characteristics of a *fragile* liquid, in contrast to covalent amorphous semiconductors (e.g Si and Ge).

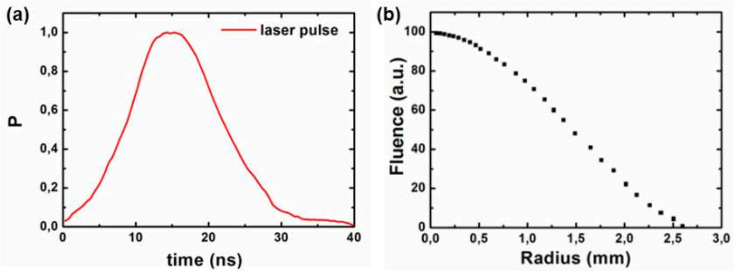

Figure 3.24 **Time (a) and spatial (b) energy profile of a single Nd:YAG laser pulse.**

As a consequence, the crystallization speed (nucleation and growth) increases more rapidly with temperature near the glass transition temperature rather than near the melting point [Kal05b]. To verify this trend we have characterized the crystallization of $Ge_2Sb_2Te_5$ far from the glass transition temperature in the fast-crystallization regime (τ~ns). To this aim we have used a pulsed Nd:Yttrium Aluminum Garnet (YAG) laser as the heat source. The stoichiometric GST films, 50 nm thick, were deposited at room temperature by radio frequency magnetron sputtering in high vacuum on a thermally grown SiO_2 layer, 550nm thick. The time evolution of the single laser pulse (measured by a photodiode) and the corresponding spatial beam profile (measured by a CCD) are reported in fig. 3.24.

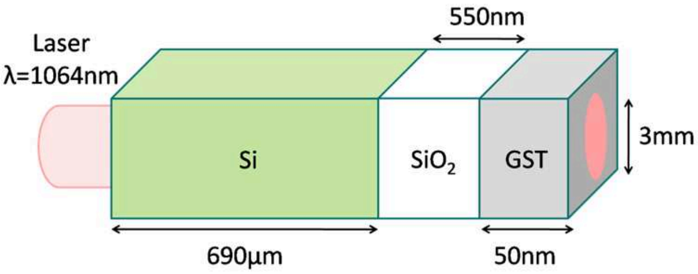

Figure 3.25 Schematic of the irradiated samples. Since the laser beam hits the Si surface the substrate acts as an attenuator and GST absorbs just a 3% of the incident fluence. A fine tuning of the energy absorbed by GST can then be achieved.

The beam is Gaussian and the energy density is constant within 10% in a circular area of 1mm diameter. This allows the direct observation of crystals and from this the estimation of the nucleation and growth rates. Transmission electron microscopy analyses have been performed using a JEOL JEM 2010F microscope. The duration and the temperature of the annealing process were independently controlled varying the number of pulses and their power, respectively. Partially crystallized film can then be prepared. The energy fluence required to induce the crystallization process in phase change materials is generally below $100mJ/cm^2$ [Hub87][Gaw11]. To obtain a fine tuning of the fluence on GST we have irradiated the sample from the backside on the (optically polished) silicon surface. The Si substrate acts as an attenuator and GST absorbs just a 3% of the incident fluence. A schematic of the irradiated samples is shown in fig. 3.25. The temperature profile as function of time has been calculated by the numerical solution of the heat equation [Poa82] using suitable, temperature dependent values for the different parameters entering in the equation

$$\frac{\partial T}{\partial t} = \frac{\alpha}{\rho c_p} I(z,t) + \frac{1}{\rho c_p} \frac{\partial}{\partial z}\left(\kappa \frac{\partial T}{\partial z}\right)$$

$$I(z,t) = E_{las} P(t)(1-R)\exp(-\alpha z)$$

where α is the absorption coefficient, ρ the density, c_p the specific heat, κ the thermal conductivity. The source term is *I* in which E_{las} is the fluence on the sample (mJ/cm^2), *R* the reflectivity, P(t) the time evolution of the laser pulse (fig. 3.24) and *z* the depth inside the sample. The parameters that we have used in these calculations are summarized in table 3.2 [Kuw06][Kuw07][Non00].

Sample	ρ (g/cm^3)	n	k	α^{-1} (nm)	c_p (J/g/K)	κ (W/m/K)
amorphous	5.86	4.3	0.8	105	0.22	0.2
fcc crystal	6.15	6.8	2.2	38	0.26	1.3

Table 3.2 **Optical and thermal properties of $Ge_2Sb_2Te_5$.**

Figure 3.26(a) shows the temperature profile as function of time at the air-GST interface in the case of laser irradiation with a fluence of 400 mJ/cm^2. The heating and the cooling rates are indicated inside the figure. Under these conditions is not possible to obtain amorphization by melt quenching since the cooling rate is too low. Figure 3.26(b) shows the corresponding temperature profile inside the GST layer at different times. The zero of the depth scale corresponds to the SiO_2-GST interface and the hottest point is at the GST free surface. The crystal nucleation is expected to occur at the GST free surface where there is the maximum of the temperature profile and where heterogeneous nucleation has been observed during low temperature annealing. We have performed several laser irradiation processes varying the incident fluence. The corresponding peak temperatures, evaluated assuming an amorphous or a crystalline (circles) GST film, are shown in fig. 3.27. At a given fluence the temperature of a crystalline film is higher than that of an amorphous film.

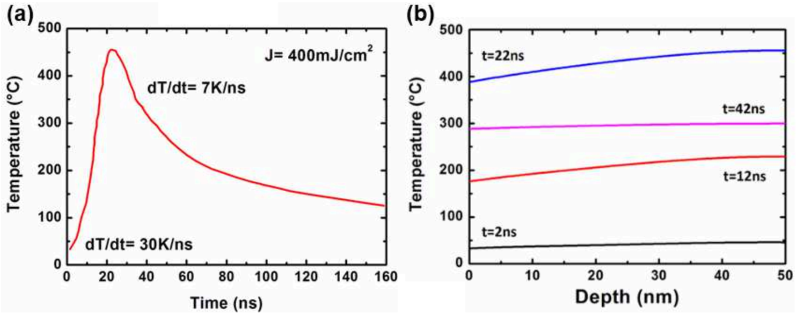

Figure 3.26 **(a) Temperature profile as function of time at the the air-GST interface in the case of laser irradiation with a fluence of 400 mJ/cm^2. (b) Corresponding temperature profile inside the GST layer for several times.**

The crystallization kinetics has been followed by ex-situ reflectivity measurements performed by a focused laser probe (λ=650nm) after the laser irradiation process.

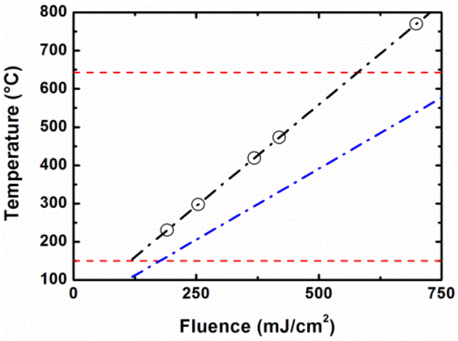

Figure 3.27 **Temperature vs incident fluence relation in the case of amorphous (blue line) and crystalline (black line) GST. The used fluencies are indicated by circles.**

In fig. 3.28(a) the measured reflectivity is reported as a function of the number of pulses for different values of the irradiation fluence. The corresponding temperatures have been calculated using the equations discussed above. At a given temperature the reflectivity increases smoothly from the amorphous to the crystalline value. The repetition rate of the pulses was 1 s^{-1} and then the sample recovers back to room temperature between successive pulses. If we assume that the relevant annealing time associated to each laser pulse is 10 ns, we can evaluate the crystallization time (τ) as the time at which the half of the whole increase in reflectivity is reached and gives the required extension of the crystallization velocity in the high temperature regime.

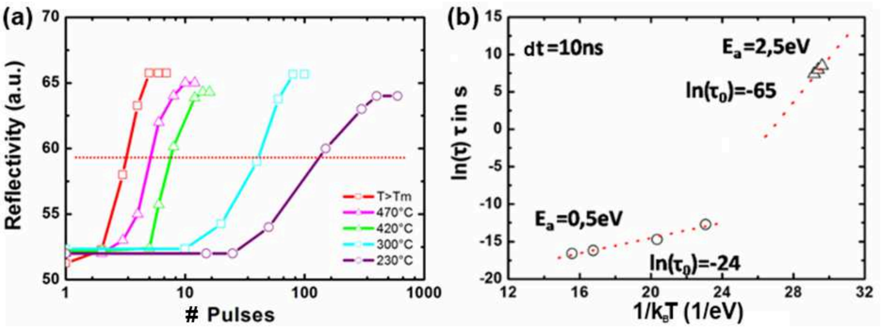

Figure 3.28 **(a) Reflectivity as function of the pulses number for several annealing temperature. (b) Crystallization time as function of 1/k_BT. The data collected near the glass transition temperature (square) are from [Kal05b].**

In fig. 3.28(b) the time τ is reported as a function of 1/k_BT and the data of the crystallization kinetics near the glass transition temperature have been added [Kal05]. The behavior in the high temperature range differs from that observed at low temperature and a single exponential law cannot fit the ensemble of the experimental data. However, using two different Arrhenius laws to fit the data in the high and low temperature regime the fitting parameters E_a and τ_0 can be extracted. It turns out that the activation energy close to the melting point is smaller than that near the glass transition temperature. Therefore we expect a difference even in the nucleation and growth rates of the crystallites. To shine a light on the crystal structure we have performed transmission electron microscopy

(TEM) and Raman analyses on partially and fully crystallized films. First of all we have identified the phase created by the laser irradiation process.

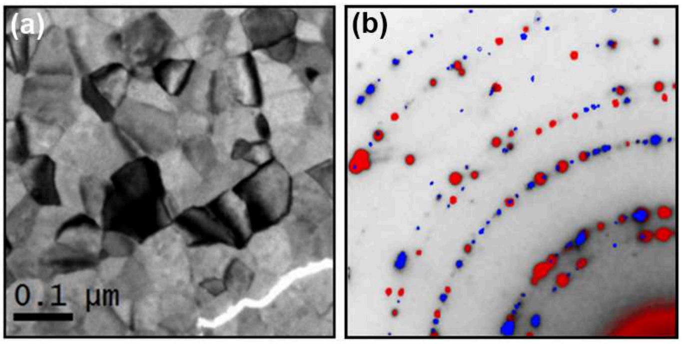

Figure 3.29 (a) Bright field TEM image of a fully crystallized GST sample (360mJ/cm^2–12 pulses). (b) The corresponding diffraction image (red) is shown with superimposed the diffraction spots of a rocksalt crystalline film annealed in furnace at ~125°C (blue).

Figure 3.29 shows a bright field TEM image of a fully crystallized sample (420°C-360mJ/cm^2–12 pulses) with the corresponding diffraction image (red dots).

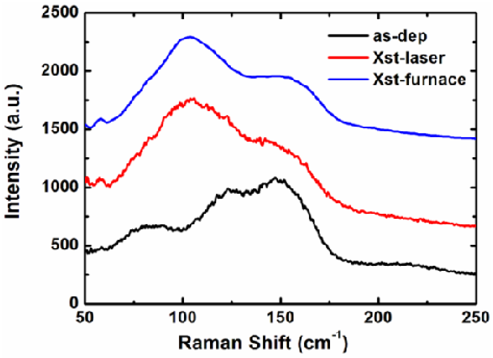

Figure 3.30 Raman spectra of amorphous and crystalline GST samples. Crystallization has been obtained by laser (red line) or in furnace annealing (blue line).

In the same figure we have superimposed the diffraction spots of a rocksalt crystalline film annealed in furnace at ~125°C (blue dots) and a perfect coincidence is clear. Figure 3.30 reports the Raman spectra collected on the same samples and again the results are indistinguishable. These observations uphold the formation of the fcc crystalline phase by laser irradiation [Fri01]. Moreover it’s interesting to note that the formation of transrotational grains does not occur during the laser irradiation process.

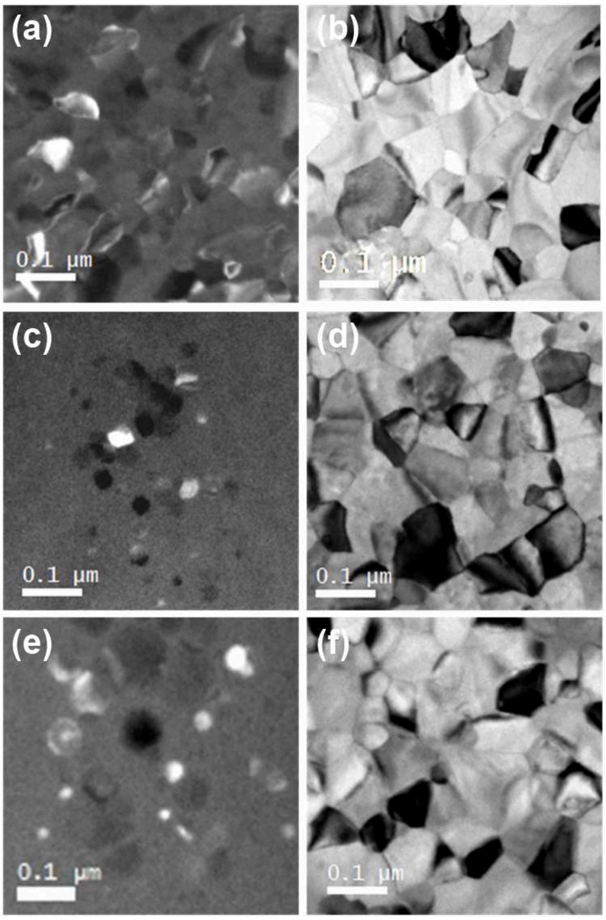

Figure 3.31 TEM images of partially and fully crystallized GST thin films after different laser irradiation processes: 250mJ/cm^2, 20(a) and 60(b) pulses; 370mJ/cm^2, 6(c) and 12(d) pulses; 420mJ/cm^2, 4(e) and 8(f) pulses.

Figure 3.31 shows the TEM images of several samples irradiated at different fluencies before and after the complete crystallization. The fluence and the corresponding number of pulses are indicated in the caption. As explained in sect. 2.2.2, it is possible to obtain a rough estimation of the grain density, of the nucleation rate and of the growth velocity by the analysis of these images assigning an annealing time of 10ns to a single pulse.

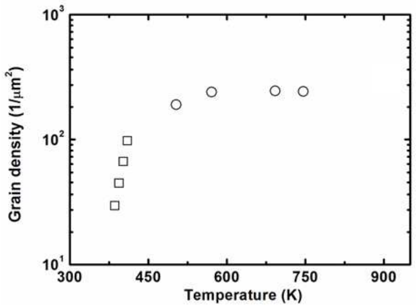

Figure 3.32 Grain density as function of temperature. Circles refer to this study whereas squares have been extracted from [Kal05].

In fig. 3.32 and 3.33 all these data are reported in comparison with the measurements performed near the glass transition temperature by Kalb [Kal04][Kal05].

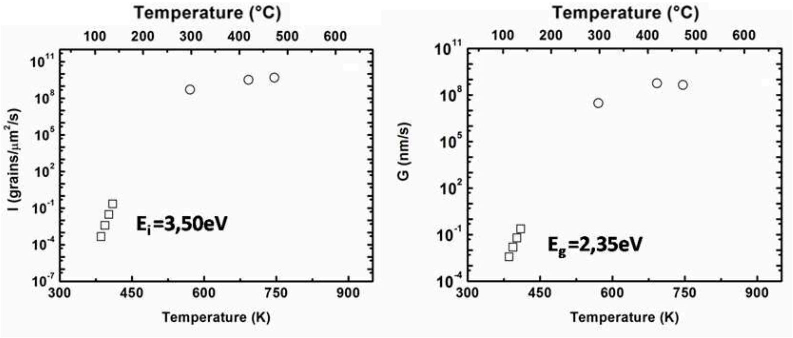

Figure 3.33 Nucleation (a) and growth (b) rate as function of temperature. Circles refer to this study whereas squares have been extracted from [Kal05][Kal04].

It is clear that in the high temperature regime both the nucleation and the growth rate approach a saturation value of $5x10^{10}$ grains/μm^2/s and $6x10^8$

nm/s. As discussed above, this behavior can be explained assuming that the amorphous state of phase change materials exhibits the characteristics of a *fragile* liquid [Kal05b].

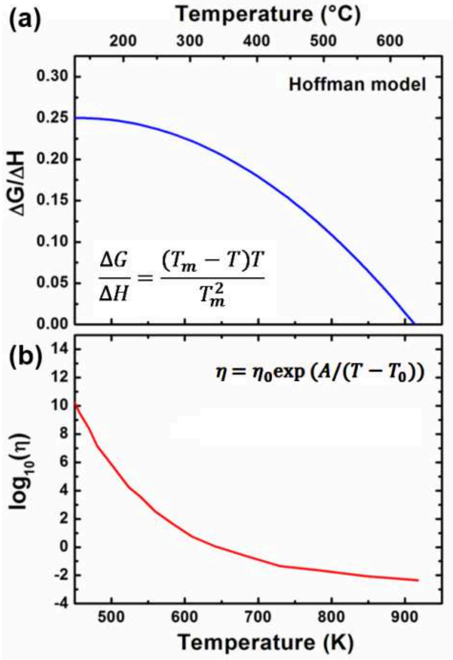

Figure 3.34 (a) Difference between Gibbs free energy of amorphous and crystalline phase as function of temperature according to the Hoffman model. (b) Viscosity as function of temperature in the case of *fragile* liquid.

According to the Hoffman model, fig. 3.34(a), below the melting temperature the driving force for crystallization (difference between Gibbs free energy of amorphous and crystalline phase) is small [Hof58]. This results in a slow transformation process despite a large atomic mobility (low viscosity). Close to the glass transition temperature, crystallization also occurs on a long time scale even though the driving force is large, since here the atomic mobility is very low, fig. 3.34(b). In the ultra-fast regime, increasing the temperature, the decrease of the viscosity is counterbalanced by the decrease of the driving force and then both the nucleation and growth rate exhibit a weak temperature dependence. As an example, fig. 3.35 shows a comparison between our measurements and the nucleation rate calculated in [Kal05b] using the standard equations discussed in par. 2.2.

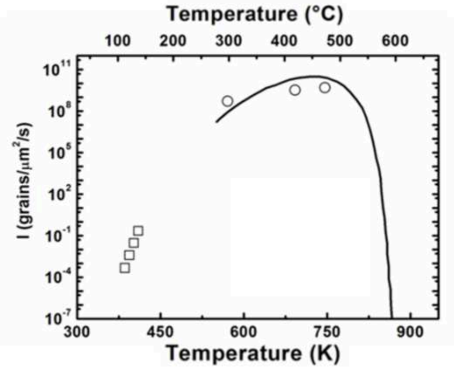

Figure 3.35 Comparison between measured and calculated [Kal05b] nucleation rate as function of temperature.

Since many of the parameters entering in the equation are not known with sufficient accuracy ((i.e. driving force and viscosity) the calculated curve has been normalized to our experimental data. Moreover it must be noted that this equation refers to the steady state whereas in our experiment we are far from this condition.

In conclusion, we have investigated the crystallization process of amorphous GST thin film in the ultra-fast regime. The crystalline state achieved by laser irradiation is the metastable rocksalt phase. Transrotational structures are not created under these conditions. Our data confirms that the extrapolation of the low temperature data to the fast-crystallization regime does not work in GST and therefore the crystallization process cannot be described by a simple Arrhenius law over the whole range of temperature. A weak temperature dependence of the nucleation and growth rates has been found far from the glass transition temperature.

This behaviour can be justified if we assume a viscosity whose temperature dependence is that of a *fragile* liquid.

3.6 Ion irradiation effects

Ion beam processing of materials results from the introduction of atoms into the surface layer of a solid substrate by bombardment of the solid with ions in the electron-volt to mega-electron-volt energy range [Nas06][Jai11]. The solid-state aspects are particularly broad because of the range of physical properties that are sensitive to this treatment. Recent interest in ion beam processing has focused on studies of ion implantation, ion beam mixing, ion-induced phase transformations. In recent years the effect of ion beam irradiation on chalcogenide alloys was investigated both in amorphous and in crystalline phases. In particular, the amorphization of a crystalline GST film by ion irradiation was investigated in detail by analyzing the effects of ion energy, fluence, and implant temperature[Deb07]. On the other hand, ion irradiation of amorphous chalcogenide, with self-atomic species (Ge^+ or Sb^+), produces a variation in the short-range order that affects the crystallization temperature of the alloys [Deb08]. A faster crystallization kinetics was measured both in GST and in GeTe because during irradiation the system is promoted, by the ion-induced thermal spike effect, to a local state closer to the crystalline phase (sect. 3.6.2 and 4.4.1). Moreover, we have demonstrated that the doping of phase change materials can be achieved by “low dose” ion irradiation as a valid alternative to co-sputtering process (sect. 3.6.4). In the next paragraphs the effect of ion irradiation on amorphous $Ge_2Sb_2Te_5$ will be detailed. Anyway, at the beginning, a brief overview on the theory of ion beam irradiation will be presented.

3.6.1 Ion-solid interaction

Once an energetic particle beam strikes matter it immediately begins to transfer energy to the target system. The energy deposition process is commonly described by the "stopping power", the energy transfer per unit path length, usually indicated in eV/nm [Nas06][Jai11]. It is also convenient to split up the particle stopping into two basic and dominant energy transfer mechanisms. One arises from ballistic (elastic) collisions with the target atoms (nuclear energy transfer) and the other from excitation and ionization of the target electrons (electronic energy transfer).

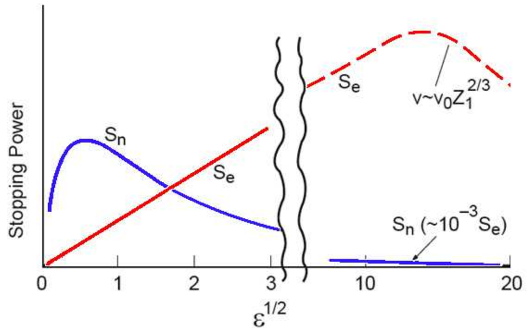

Figure 3.36 The nuclear and electronic stopping power, normalized to the atomic density, are reported as function of the square root of the reduced energy ε [Nas06].

The total stopping power is then the sum of both components whose reciprocal integral defines the total projectile range. Both stopping powers increase with increasing energy, reach a maximum and thereafter fall away as shown in fig.3.36. The electronic stopping power, however, reaches its maximum at energies which are orders of magnitude higher than that for nuclear stopping. In the low energy regime (ε<1), it is possible to roughly calculate both the stopping powers, normalized to the atomic density, by the following equations

$$S_n = 0.28 \frac{Z_1 Z_2}{\left(Z_1^{1/2} + Z_1^{1/2}\right)^{2/3}} \frac{M_1}{M_1 + M_2} \; [eV \cdot nm^2/atom]$$

$$S_e = 0.383 \frac{Z_1^{7/6} Z_2}{\left(Z_1^{2/3} + Z_1^{2/3}\right)^{3/2}} \left(\frac{E}{M_1}\right)^{1/2} \; [eV \cdot nm^2/atom]$$

where E is the ion energy, M and Z are the mass number and the atomic number of incident ions (1) and of target atoms (2). The reduced energy (abscissa of fig.3.36) is proportional to the ion energy according to the equation

$$\varepsilon = \frac{E}{Z_1 Z_2 e^2} \frac{a_{TF} M_2}{M_1 + M_2}$$

where *e* is the electron charge and a_{TF} the Thomas-Fermi screening distance. Light ions of any energy, and energetic heavy ions deliver much more energy via electronic excitation than by nuclear collisions. For low energy heavy ions the nuclear energy transfer dominates. Several phenomena are related to the ion-solid interaction and in fig. 3.37 they are summarized on the basis of the involved energy-transfer mechanism.

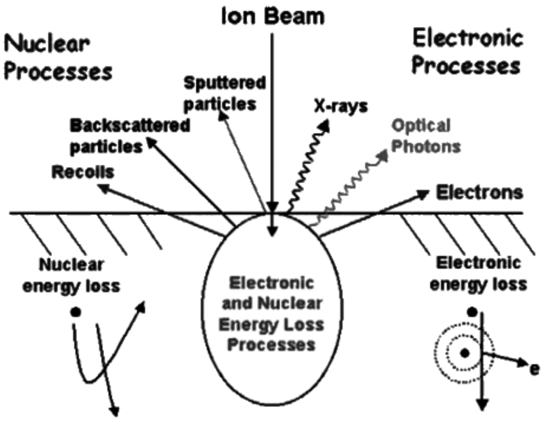

Figure 3.37 **Basic ion-solid interaction processes [Jai11].**

In our studies, we have performed ion irradiation on phase change materials with heavy ions (Ge or Sb) in a low energy regime (40-130 keV). Under these conditions ballistic processes (e.g. damage formation, sputtering, ion beam mixing) are the most important since nuclear energy loss is dominant. This is reflected in the particular not straight trajectories as the ion comes to rest within the solid, fig.3.38. The integrated distance traveled by the ion is called range, R. It depends on the stopping power and on the atomic density N according to the following equation

$$R = \int_E^0 \frac{1}{N(S_n + S_e)} dE \approx \int_E^0 \frac{1}{NS_n} dE$$

Obviously, it increases with E and decrease with N and S. The ion's net penetration into the material, measured along the vector of the ion's incident trajectory is called projected range, R_p. Ion implantation is a stochastic (random) process and the uncertainty in the scattering process as the ion travels through the target gives rise to ions coming to rest at several different distances. The mean projected range represents the most probable location for an ion to come to rest. The average fluctuation (standard derivation from the mean) in the projected range is called range straggling, ΔR_p.

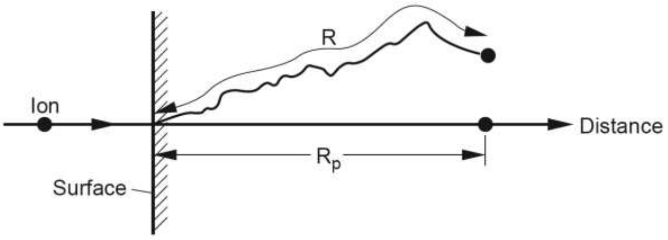

Figure 3.38 An ion incident on a solid penetrates with a total path length R, which gives a projected range R_p, along the direction parallel to that of the incident ion [Nas06].

As we pointed out above, primary nuclear interactions lead to transfer of kinetic energy from the ion to the target atoms, which can be displaced themselves from their original positions if the transferred energy exceeds a threshold value (i.e. the displacement energy). If the energy transferred to the primary atom is sufficiently high, secondary, tertiary and higher order atomic knock-on can be created thus creating a cascade of atomic collisions. This leads to a distribution of vacancies, interstitial atoms and other types of lattice disorder in the region around the ion track. As the number of ions incident on the crystal increases (i.e., increasing the irradiation fluence), the individual disordered regions begin to overlap. At some point, a heavily damaged layer is formed. The total amount of disorder and the distribution in depth depend on ion species, temperature, energy, total dose and channeling effects.

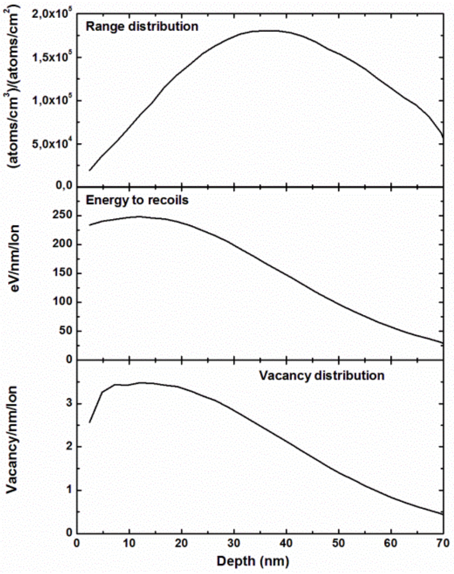

Figure 3.39 (top) Projected range distribution (R_p) of 120keV Sb^+ on GST. Corresponding energy to recoils (middle) and vacancy distribution (bottom).

The ion irradiation process can be simulated by the SRIM code [Zie85]. This is a group of programs which calculate the stopping and range of ions into matter using a quantum mechanical treatment of ion-atom collisions. It is based on a Monte Carlo simulation method and on the binary collision approximation (BCA): the incident ion moves inside the target and is subjected to a sequence of independent elastic binary collisions with sample nuclei. Between the collisions, the ion travels in a straight path and it is slowed down by the coulomb interaction with the target electrons. An example of the results from SRIM calculations is reported in fig. 3.39. We have simulated the ion irradiation with 120keV Sb ions on $Ge_2Sb_2Te_5$ film. If we assume a dose of 10^{14} ions/cm^2 the maximum Sb concentration is $1.7x10^{19}$ atoms/cm^3 (0.05 at. % of antimony). The corresponding vacancy (interstitial) concentration is $3.5x10^{21}$ cm^{-3}. This means that each ion creates more than 100 vacancies and on the other hand each atom of the alloy takes part in a collision cascade. This calculation is performed at 0 K and then recombination of defects is neglected. In the next paragraphs we will detail the consequences of ion irradiation on GST starting from the effect on the stability and on the local order of the amorphous phase.

3.6.2 Modification of the crystallization process

$Ge_2Sb_2Te_5$ amorphous films, 50 nm thick, have been deposited on a 100nm SiO_2 layer. Part of the samples have been irradiated at room temperature by 120 keV Sb^+ ions with several fluencies ranging from $2x10^{12}$ to 10^{14} ions/cm^2. The ions projected range, by SRIM calculations, is ~40nm (ΔR_P~20 nm). In the investigated dose range any chemical effect of the implanted species can be neglected. The energy density deposited, by nuclear elastic collisions inside the GST layer, amounts to 95 keV/ion and it is almost constant across the sample. The beam current was kept constant to 50 nA in order to avoid heating. The as-deposited and ion implanted amorphous layers were crystallized by isothermal annealing at 122°C. The kinetics of the transition was monitored by in situ time resolved reflectivity (TRR) using a low power He–Ne laser probe (λ=633 nm, 5 mW), fig.3.40. Ion irradiated samples exhibit a faster crystallization with respect to the as deposited one. The incubation time, defined as the time at which the first derivative of the reflectivity vs time curves show a maximum, decreases on the irradiation fluence. During the following discussion we will compare as deposited film with samples irradiated with a fluence of 10^{14} ions/cm^2. First of all, we have measured the dependence of the incubation time on temperature. In both cases an Arrhenius dependence has been found and a smaller activation energy is observed in irradiated samples (2.15eV vs 2.45eV), fig.3.40 (b). It is known, par. 2.2.1, that this value is related to both nucleation and growth activation energies but it is not possible to disentangle this dependence by TRR measurements. Moreover the narrow accessible temperature range in which it is affordable to investigate the crystallization process does not permit to evaluate with high precision the crystallization parameters also by microscopic techniques (the overall error is generally greater than 0.3eV).

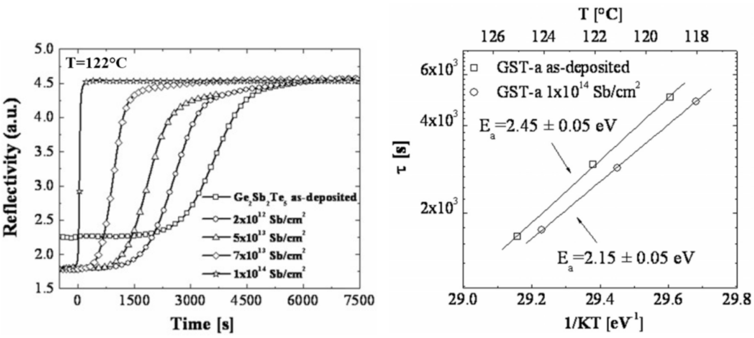

Figure 3.40 (a) Time resolved reflectivity measurements performed on as deposited and ion irradiated GST samples during isothermal annealing at 122°C. (b) Incubation time, as function of $1/k_bT$, of as deposited and 10^{14} Sb^+/cm^2 ion implanted GST.

We have then analyzed the samples by X-ray diffraction (XRD), transmission electron microscopy (TEM) and atomic force microscopy (AFM) to realize a comparison with the measurements on as deposited samples reported in paragraph 3.3.1 and 3.3.2. As in the case of as deposited film (fig.3.11), several samples with different crystalline fraction, equal to 20%, 40%, 60%, 80% and 100%, have been prepared by stopping at different time the thermal treatment. The corresponding X-ray spectra are shown in fig. 3.41. In the crystallized samples, the diffraction peaks due to the (200) and (220) planes of the metastable fcc phase appear. Their intensity increases on the crystalline fraction and simultaneously the bump associated to the amorphous phase reduces. Their position remains constant in the irradiated film during the crystallization process, indicating the formation of a fcc phase, with a lattice parameter characteristic of the bulk value. We must note here that these peaks have been found at smaller angles in the unirradiated partially crystallized samples (fig. 3.12) and that this shift was attributed to the presence of transrotational crystalline grains. Figure 3.42(a) shows the lattice parameter derived from XRD analyses, as function of the crystalline fraction in both irradiated and as deposited samples.

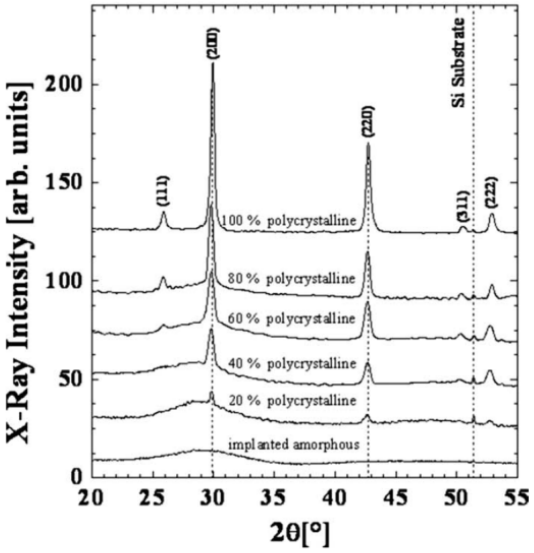

Figure 3.41 XRD of 10^{14} Sb^+/cm^2 ion implanted $Ge_2Sb_2Te_5$ films at different crystalline fraction. The peaks positions related to the diffraction of (200) and (220) planes are marked with dashed vertical lines with the contribution of Si substrate.

The FWHM of these peaks is smaller in the irradiated films and it decreases on the crystalline fraction as in the case of as deposited film, 3.42(b). To obtain a direct, although qualitative, influence of the different initial amorphous structures on the subsequent crystallization, GST samples were analyzed in a transmission electron microscope. To directly compare unirradiated and irradiated amorphous, some samples were prepared implanting 120 keV Sb^+ ions at room temperature at a fluence of 10^{14}ions/cm^2 through a mask consisting of a copper grid, with holes and bar width of 36µm and 25µm, respectively, placed at the sample surface. In this way selectively implanted regions next to unimplanted areas were formed. Figure 3.43 shows a bright-field TEM image of the film surface after 15 min *in situ* anneal at 130 °C. At this temperature, crystallization occurs inside and outside the ion irradiated area.

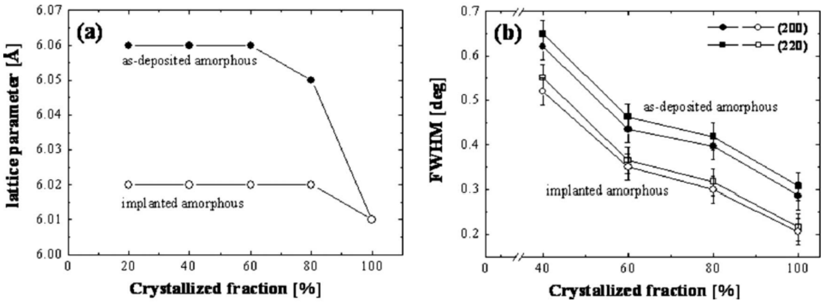

Figure 3.42 (a) Dependence of the lattice parameter on the crystallized fraction (fcc phase) for unirradiated (full circles) and irradiated (open circles) amorphous GST films. (b) Width of (200) and (220) peaks, obtained by profile fitting analysis.

A different morphology of crystalline grains in the implanted and unimplanted regions is clearly visible.

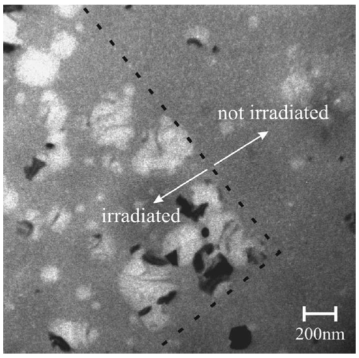

Figure 3.43 TEM plan-view micrographs of as-deposited amorphous GST films implanted with 120 keV 10^{14} Sb^+/cm^2. The presence, during implantation, of a copper mask placed on the sample surface has produced selectively implanted areas next to not implanted areas.

In the first case the typical contrast of transrotational structures, characterized by dark fringes corresponding to bending contours, does not appear. Another peculiarity is the absence of “crystalline small spots”, par.

3.3.2. The density of crystalline nuclei is higher than that in as deposited region. In other words, ion irradiation strongly influences the morphology and the crystallization kinetics of the phase transition. Further insight into the evolution of the crystalline grains can be inferred from STEM plan view micrographs of samples with different crystalline fraction 20%, 40%, 80%, and 100%, reported in fig. 3.44. The images of as deposited samples are shown again for comparison.

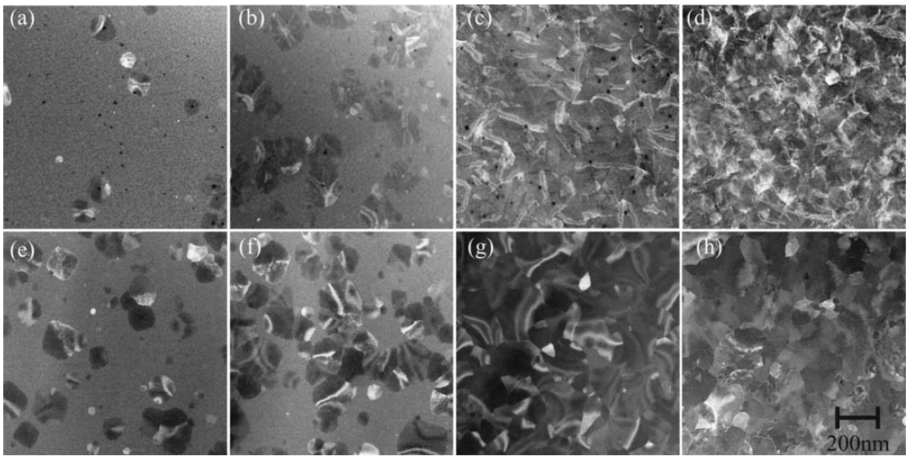

Figure 3.44 STEM plan-view micrographs of as-deposited (top) and ion irradiated (bottom) amorphous GST films, annealed at 122°C with 20% (a)(e), 40% (b)(f), 80% (c)(g), and 100% (d)(h) crystalline fraction. Ion irradiation was performed with 120 keV 10^{14} Sb^+/cm^2.

In ion irradiated samples, as the process evolves, the grains show very large fringes and a quite uniform contrast. This means that the degree of internal bending decreases. On the other hand the grain size is greater than the value expected from the X-ray measurements (using the Sherrer formula). As we pointed out in par. 3.3.2 the occurrence of the transrotational structures is related to the increase of the atomic density observed during crystallization. To accommodate this variation, crystalline grains generate an internal bending. The bending angle was estimated to be about 0.05° per nanometer of lateral displacement in the partially crystallized unirradiated films. This value decreases to about 0.02°/nm in the partially crystallized irradiated samples. To check if the bending reduction in the irradiated GST derives from a density variation due to the ion-solid interaction, we analyzed, by AFM, the morphology of the irradiated and unirradiated regions, obtained implanting trough a mask. The AFM image, shown in fig. 3.45, indicates that the ion beam induces a reduction of the film thickness, of about 1.7 nm, with respect to the surface of the unirradiated regions.

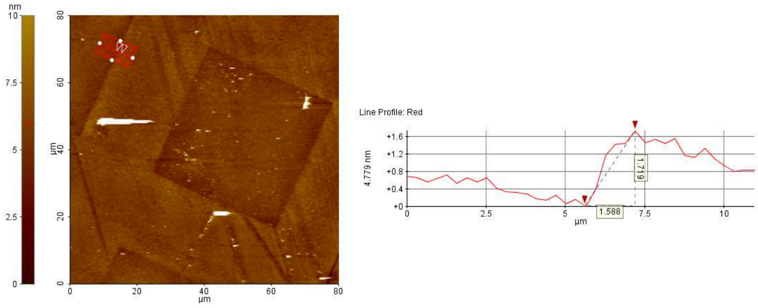

Figure 3.45 **AFM image of as-deposited amorphous $Ge_2Sb_2Te_5$ films implanted with 120 keV 10^{14} Sb^+/cm^2 trough a copper mask. As shown in the line profile, irradiated regions are depressed of ~1.7 nm compared to those not exposed to the ion beam.**

This reduction is comparable to that observed, in as deposited samples, at the boundaries of crystalline domains as a consequence of the density change upon crystallization (2-3 nm). This densification process explains then both the smaller internal bending of the crystals nucleated in the irradiated samples and also the absence of “crystalline small spots” at the beginning of the crystallization process. Moreover, taking into account the measured angular bending, the size, and the estimated thickness of the grains, one can evaluate the average lattice parameter. In partially crystallized samples, for grains of about 25 nm section size, the average lattice parameter amounts to 6.07 and 6.03 Å for as-deposited and implanted amorphous samples, in good agreement with the XRD data. As pointed out in par. 3.3.2, due to the bending, only a limited amount, about 10%, of crystalline volume contributes to the diffraction thus reducing the size of the diffracting crystal and increasing the FWHM of the diffraction peaks. The smaller bending observed in irradiated crystalline samples can then explain the smaller FWHM of the X-ray peaks, with respect to as deposited films. It is interesting to note that ion induced film densification can also influence the crystallization kinetics. After irradiation, the formation of grains with a strong internal bending is not required upon crystallization and this can lead to an energy gain. In fact, in this case, the elastic strain created to accommodate the difference in density between the amorphous and the crystalline phase will be much lower since densification is partially completed after ion irradiation. Another explanation can be related to the bond rearrangement induced on the amorphous network by the energy released during the irradiation process. We have then analyzed the irradiated samples by EXAFS and Raman spectroscopy and the results have been compared with those obtained in as deposited samples.

3.6.3 Local structural changes of the amorphous phase

It is known that the degree of short range order in amorphous solids depends on the sample processing. Differences in the crystallization velocity between as deposited, relaxed, melt quenched and ion implanted amorphous samples have been reported, par. 2.3. In particular, as we have shown, both melt quenched and ion irradiated amorphous GST show a faster crystallization with respect to the as deposited film [Khu00]. The origin of this difference is likely to be related to a variation of the structure of the amorphous state and a detailed investigation of the local order variation is needed to get insights into the microscopic mechanism governing this phase transition. In this paragraph we report the investigation, by extended X-ray absorption fine structure spectroscopy (EXAFS) and Raman spectroscopy, of the local order in amorphous GST films after ion irradiation. We will compare these data with the results of the same analyses performed on as deposited (sect. 3.2.1 and 3.2.2) and melt quenched (primed) amorphous. Amorphous $Ge_2Sb_2Te_5$ films, 50 nm thick, are deposited at room temperature on a thermally grown SiO_2 layer. The ion irradiated amorphous film was prepared by implanting 130 (120keV) keV Ge^+ (Sb^+) ions at a fluence of 10^{14} ions/cm^2 at room temperature. The melt quenched amorphous film was obtained by pulsed (10 ns) Nd:YAG laser irradiation (λ=532 nm second harmonic) at an energy density of 180 mJ/cm^2 of the deposited amorphous. To perform EXAFS analyses, we measured the K edges of Ge, Sb, and Te and four spectra per sample were collected in order to improve the signal-to-noise ratio.

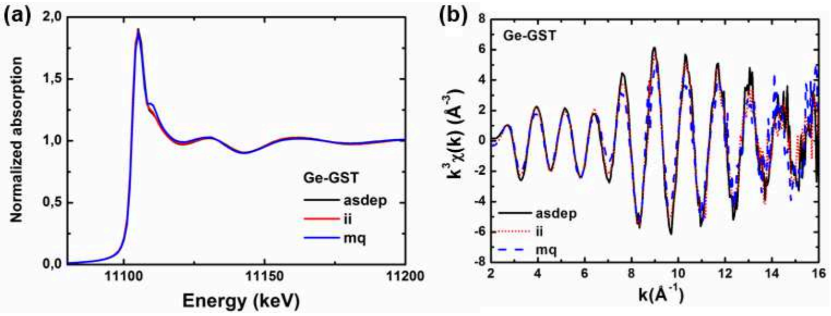

Figure 3.46 Normalized absorption spectra (a) and k^3-weighted EXAFS data (b) relative to the germanium edge of as deposited (black line), ion implanted (red line), melt quenched (blue line) GST amorphous samples.

The germanium edge absorption spectra of the different amorphous GST samples are presented in fig. 3.46(a) coupled with the corresponding k^3-weighted EXAFS data (b). The related amplitude of the Fourier transforms (Fts) are shown in 3.47. The FTs exhibit a peak just above 2.4 Å and a shoulder at 2.2 Å denoting the presence of two types of bonds around Ge. As pointed out in sect. 3.2.1, both Ge-Ge and Ge-Te bonds are required to fit the data. A dumping of the EXAFS oscillations and of the FTs signals, clearly visible in fig. 3.46(b) and 3.47, occurs after ion or laser irradiation. In particular, a reduction of the shoulder at 2.2 Å, due to homopolar Ge-Ge bonds, is evident in the melt quenched amorphous sample. It is possible to fit these variations using a greater Debye–Waller factor σ^2 coupled to a small increase of the Ge-Ge bond length. The fitting parameters are summarized in table 3.3. The increase of the σ^2 is indicative of an increase of the atomic disorder associated to a different structural configuration after laser or ion irradiation.

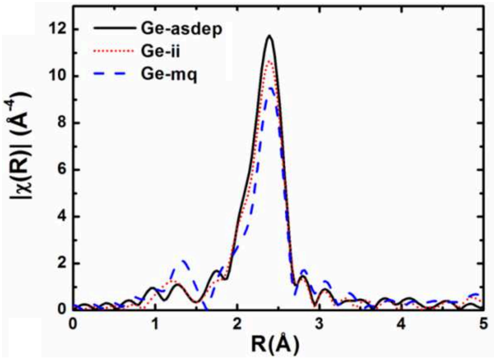

Figure 3.47 **Fourier transformed EXAFS spectra of the data shown in fig. 3.46(b).**

On the other hand, the damping of the shoulder at 2.2 Å can be alternatively ascribed to a reduction of the homopolar Ge-Ge bonds. In particular the Ge-Ge relative coordination number decreases from 0.9 to 0.8 and 0.6 after ion and laser irradiation, respectively.

Sample	d(Ge-Ge) (Å)	σ^2 (Ge-Ge) (Å^2)x10^{-3}	d(Ge-Te) (Å)	σ^2 (Ge-Te) (Å^2)x10^{-3}
as-dep	2.51(1)	9.0(4)	2.62(1)	5.9(4) Å^2
ion implanted	2.51(1)	10.2(4)	2.62(1)	6.2(4) Å^2
melt quenched	2.53(1)	13.8(4)	2.62(1)	6.6(4) Å^2

Table 3.3 **Bond lengths and Debye–Waller factors σ^2 measured at the germanium edge of the different amorphous GST samples: as deposited, ion implanted and melt quenched.**

This interpretation matches nicely the expectation based on recent density functional calculations in which a greater abundance of homopolar Ge-Ge bonds was observed in as deposited with respect to melt quenched amorphous [Ako11]. Laser irradiation of the as deposited film induces the breaking of homopolar bonds and promotes the system to a state closer to the crystalline phase, since homopolar “wrong” bonds inhibit the crystallization process of GST. As a further support we like to recall that a damping of EXAFS oscillations coupled with an increase of the bond lengths has been reported by Kolobov, fig. 1.19, during the crystallization [Kol04]; so the evolution during crystallization is very similar to the transformation of the amorphous phase upon laser or ion irradiation. We have also collected the EXAFS signal on both the Sb and Te edge, fig. 3.48. Unfortunately, the signal to noise ratio is too low to distinguish meaningful differences between the different amorphous samples (as deposited, ion implanted, melt quenched) and then the fitting parameters are the same discussed in par. 3.2.1 and reported in table 3.1.

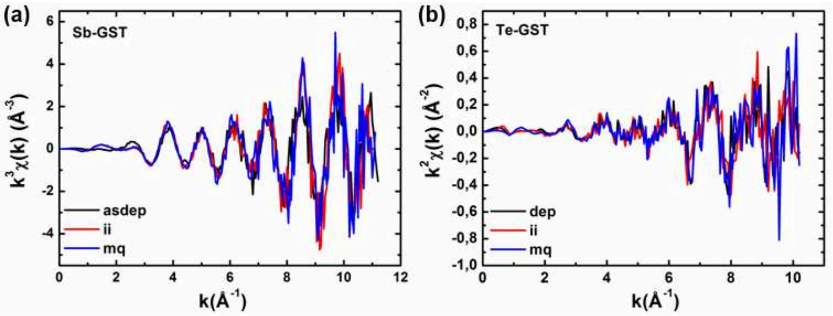

Figure 3.48 k-weighted EXAFS data relative to the Sb (a) and Te (b) edge of as deposited (black line), ion implanted (red line), melt quenched (blue line) GST amorphous samples.

In order to overcome this difficulty, we have also performed Raman spectroscopy measurements. Figure 3.49 shows the spectra of the as-deposited, of the laser and ion irradiated samples. The signals were fitted by two main Gaussian contributions centred at ~125 cm^{-1} (A) and ~150 cm^{-1} (B). Both the spectra of the irradiated amorphous exhibit a reduction of the peak A intensity with respect to unirradiated film: the area ratio A/B decreases from 0.35 to 0.22 after irradiation. This means that the variation in the local order of the amorphous phase is similar in melt quenched and ion irradiated samples. As discussed in sect. 3.2.2 and according to first principles calculations [Sos11], all the features of the spectrum can be assigned to vibrations of defective octahedra that, as stressed before, are the main building blocks of the amorphous network. Anyway, the presence of Te-Te dimers and trimers contributes to the intensity of the band at 125 cm^{-1}. In fact, it is known that crystalline Tellurium has the strongest peak at 122 cm^{-1} [Pin71]. Therefore, the reduction of peak A occurring in the irradiated amorphous in comparison with as deposited sample should be indicative of a reduction of the homopolar Te-Te bonds, that are forbidden in the crystalline structure (sect. 1.3.1). This rearrangement promotes the crystallization process and then can explain the higher crystallization rate observed in melt quenched and ion irradiated amorphous GST with respect to as deposited film.

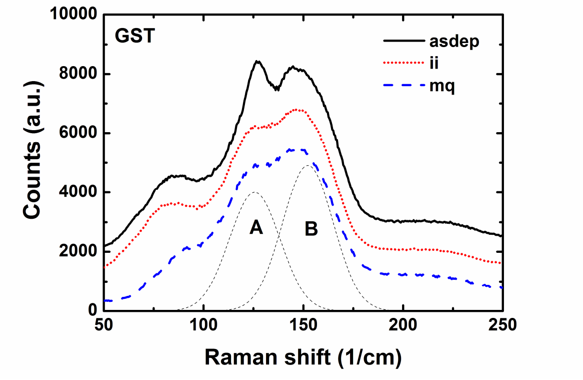

Figure 3.49 **Raman spectra of different amorphous GST films: as deposited (solid line), ion implanted (red dotted line), melt quenched (blue dashed line). The dotted lines represent the contribution of the 125 cm^{-1} and 150 cm^{-1} peaks to the Raman spectrum.**

It is important to note that this bond rearrangement is due to the energy release associated to both the irradiation processes. This energy allows an increase of temperature (atomic mobility) able to produce a reorganization of the amorphous network. During laser irradiation, photons are absorbed and then, after thermalisation, the energy is transferred to lattice vibration (heat) [Poa82]. In the case of ion irradiation the concept of *thermal spike* must be invoked [Nas06][Poa83]. As the formation of a collision cascade comes to an end, all the moving displaced atoms reach a point where they have insufficient energy to cause further displacement. Energy transfers will be at subthreshold levels. At this point the energy will be shared between neighboring atoms and will be dissipated as lattice vibrations or “heat.” After approximately 10^{-12}s, a state of dynamic equilibrium may be obtained. This period of lattice heating is known as the thermal spike phase of the collision cascade and may exist for several picoseconds before being quenched to ambient temperature. Once such a dynamic equilibrium is established, the concepts of local heating and temperature become reasonable. During both laser and ion irradiation the sample temperature is expected to reach a value near to the melting point.

In conclusion, we have performed EXAFS and Raman spectroscopy measurements on different amorphous GST thin film (as deposited, melt quenched and ion implanted) with the intent to correlate the irradiation induced variation of the local structure to the enhancement of crystallization rate of the irradiated films. By EXAFS analysis, we have observed a stronger contribution from homopolar Ge-Ge bonds in the as deposited sample with respect to irradiated films. This bond is slightly longer in MQ amorphous (2.53 Å) than in AD and II samples (2.51 Å). Ge-Te bond length (2.62 Å) is not modified by laser or ion irradiation. Raman spectroscopy measurements indicate a greater abundance of homopolar Te-Te bonds in AD film with respect to MQ and II. Both techniques show that a reduction of “wrong” homopolar bonds (Ge-Ge and Te-Te) occurs as a result of laser or ion irradiation of amorphous GST films. Therefore, the reduction of the homopolar bonds seems to be, among the different phenomena occurring during the irradiation, the most efficient in modifying the crystallization rate.

3.6.4 Recoil implantation and sputtering

As we discussed in par. 2.3, doping of chalcogenide is one of the most investigated topic. The amorphous stability and the phase change velocity can be improved varying the doping species and their amount. The direct doping by ion implantation, in view of the required high concentration, implies low energy and fluence in excess of 10^{15} ions/cm^2. Usually the thickness of the chalcogenide films is in the order of 10–50 nm and then, for these fluence-energy combinations, preferential sputtering is expected to play a relevant role with changes in the film stoichiometry and thickness. It follows that, in the absence of a capping layer, a variation in the stability of the amorphous phase is expected because it is known that the crystallization temperature of the alloy depends on the stoichiometry and thickness of the GST film, par. 2.3. A method to avoid the modification occurring during high fluence implantation could be the use of a cap layer although other effects due to the recoil implantation that affect the film stability must be evaluated first. As recently reported, ion irradiation performed with Ge^+ ions on a GST film covered with a SiO_2 layer enhances the thermal stability of the amorphous phase [Rao10]. In this scenario chemical and structural effects induced by ion implantation are entangled. Both the variation in the short-range order of the amorphous phase (sect. 3.6.3) and the Si and O doping induced by recoil implantation are expected to play a role. During slowing down, the impinging ions collide with the atoms of the cap film. As a result of these collisions atoms in the cap are set into motion and some may have enough energy to travel into the underlying substrate. On the other hand, the energy released from the implanted ions during the collision cascade (thermal spike) is enough to induce structural changes in the amorphous network. In this paragraph we show the different effects, produced by Ge ion implantation, on the stability, thickness, and stoichiometry of a GST film with and without a thin SiO_2 cap layer. We will focus our attention on the 10^{14}-10^{15} ions/cm^2 dose range. Amorphous $Ge_2Sb_2Te_5$ films, 20 nm thick, were deposited on a thermally grown SiO_2 layer. Some samples were covered with a sputtered SiO_2 cap layer, 10 nm thick. Ion implantation on both capped and uncapped samples was performed with Ge^+ ions at 40 keV and fluencies in the range between $5x10^{13}$ and $1x10^{15}$ ions/cm^2 maintaining a constant current of 0.3 µA. The pressure during irradiation was maintained below 10^{-7} mbar. The Ge projected range was 25 and 26 nm in the capped and uncapped GST films, respectively. Therefore, in the capped samples the maximum of the

Ge concentration is located inside the film, whereas in uncapped samples it is close to the GST–SiO_2 interface in the SiO_2 side. The sample stoichiometry before and after irradiation was measured by Rutherford backscattering spectrometry (RBS) and particle induced X-ray emission (PIXE), and from this the sputtering yield of each species was evaluated. Particularly, a 2.0 MeV He^+ beam was used to determine the Ge/(Sb + Te) concentration ratio by RBS, and the Sb/Te concentration ratio was estimated by PIXE (K_α peaks intensities) using a 2.7 MeV He^+ beam. The crystallization kinetics was recorded by in situ time resolved reflectivity (TRR) using a 5 mW He–Ne laser probe during annealing from room temperature to 200°C at a constant heating rate of 6°C/min. The crystallization temperature is experimentally defined as the maximum in the first derivative of the reflectivity versus temperature curve.

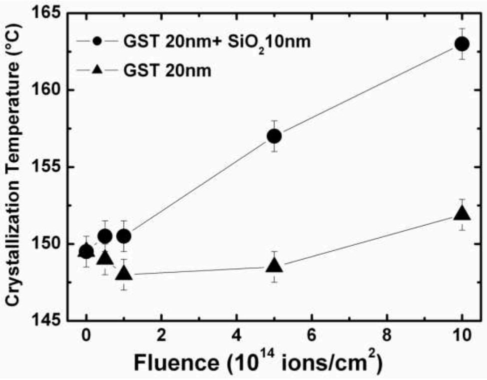

Figure 3.50 **Crystallization temperature as a function of the implanted fluence in GST samples with (circles) and without (triangles) the SiO_2 cap.**

Information on the local structure of the amorphous phase was obtained by unpolarized micro-Raman analyses performed at room temperature in a backscattering geometry using a single spectrometer. The effects of ion implantation on the GST samples are estimated by the SRIM code [Zie85]. We have also performed the same calculations by TRIDYN, an evolution of the SRIM code, developed by Möller and Eckstein, taking into account the dynamic change of thickness and composition of multicomponent targets during ion implantation [Mol84]. Figure 3.50 shows the crystallization temperature as a function of the Ge fluence in the capped (dots) and uncapped (triangle) GST samples.

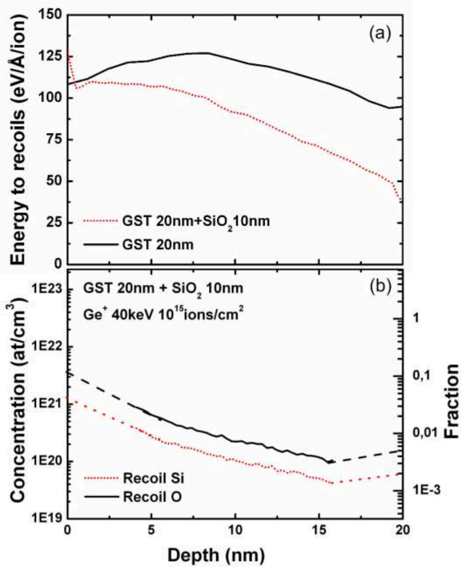

Figure 3.51 **(a) Profile of the energy transferred to recoils for the implantation of 40 keV Ge^+ ions on the capped (dotted red line) and uncapped (black solid line) GST film, 20 nm thick, calculated by the SRIM code. The zero of the depth scale is set at the surface of the GST layer. (b) Si (red dotted line) and O (solid line) recoil concentration profile inside a capped GST film after irradiation by 40 keV Ge^+ at a fluence of 10^{15} ions/cm^2 (SRIM calculation). The zero of the depth scale is set at the interface between the SiO^2 cap and the GST film.**

In capped GST the crystallization temperature increases continuously from 149.5°C in the unimplanted amorphous to 163°C after irradiation with 10^{15} ions/cm^2, indicating a greater stability of the implanted amorphous. The crystallization temperature of uncapped samples decreases by ~2°C with increasing fluence up to 10^{14} ions/cm^2 (par. 3.6.2), at higher fluencies it increases up to a maximum value of 152°C. The large difference in the stability of the capped and uncapped irradiated amorphous is likely not related to the ion energy loss profile which is similar in the two cases, as can be inferred from fig. 3.51(a) in which the depth profile of energy released to recoils is reported. The data were obtained by the SRIM code. The zero of the depth scale is set at the surface of the GST layer. The energy released into the uncapped GST layer is ~20% higher than that released in the capped film. So, if a high degree of randomization is associated with high stability of the amorphous phase, we should expect that, on the basis of the SRIM calculation, the irradiated uncapped amorphous samples are more stable with respect to the capped ones, opposite of the measured trend. On the other hand, the large similarity between the profiles of the energy released in the two samples suggests the occurrence of like variation in the local order of the amorphous phase during ion irradiation. Figure 3.52 shows the Raman spectra of the as-deposited and of the capped and uncapped GST irradiated with 5x10^{14} ions/cm^2.

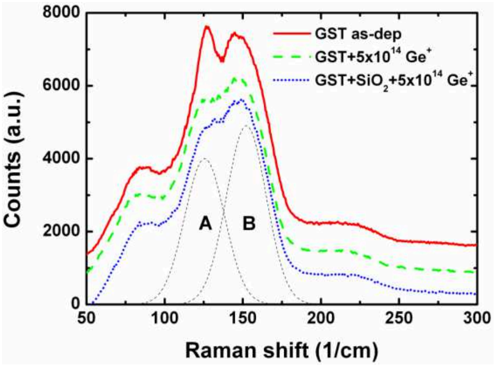

Figure 3.52 Raman spectra of as-deposited (solid line) and ion implanted GST samples 5x10^{14} ions/cm^2 with (dotted line) and without (dashed line) the SiO$_2$ cap layer.

The spectra of the irradiated samples do not show meaningful differences in the investigated fluence range. They were fitted by two main Gaussian contributions centered at ~126 cm^{-1} (A) and ~152 cm^{-1} (B). The spectra of the irradiated amorphous are undistinguishable, and they both exhibit a reduction of the peak A intensity with respect to an un-irradiated film. This means that the same variation in the local order of the amorphous phase is achieved, by thermal spike ion induced effects, in the capped and uncapped GST layers (sect. 3.6.3). The reduction of the peak A intensity is indicative of a state closer to the crystalline phase, as discussed in the previous paragraph. This feature has been invoked to justify the lowering of the crystallization temperature occurring in the uncapped samples implanted at a low fluence, below 5x10^{14} ions/cm^2, but it does not work in the case of the capped films in which the implantation enhances the stability of the amorphous phase. Other effects related to the material modification by ion irradiation will be taken into account to explain the behavior of the ion implanted capped GST. The higher crystallization temperature of the uncapped samples irradiated at a high fluence could be the result of the variation of the film stoichiometry because of the preferential sputtering during irradiation.

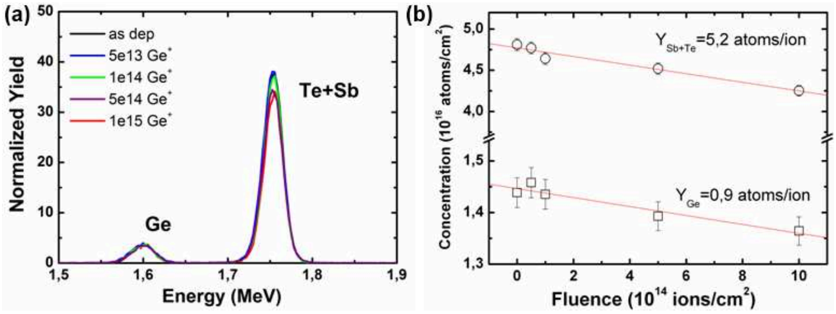

Figure 3.53 (a) RBS spectra of the as-deposited and Ge^+ implanted GST uncapped samples. The He^+ beam has an initial energy of 2 MeV. The high energy peak is an overlap of the signals from Sb and Te whereas the low energy peak is due to the backscattering from Ge atoms. (b) Corresponding sputtering yields as obtained by the fitting of the RBS measurements.

We performed RBS and PIXE analyses to monitor the change in the sample stoichiometry and thickness with irradiation. The concentration of Ge and Sb+Te in the implanted samples at several doses was obtained by the RBS measurements. Figure 3.53(a) shows the spectra of the as-deposited GST and uncapped GST implanted to a fluence of 10^{15}ions/cm^2. The He^+ beam energy was 2 MeV. The peak at high energy is the overlap of the signals from Sb and Te, whereas that at low energy is due to the backscattering from Ge atoms, according to the different kinematical factors. In our spectra the statistical error is on the order of 1 atom %. The Sb+Te peak intensity is clearly reduced after irradiation whereas the Ge peak intensity is almost unchanged. This behavior is confirmed over the range of fluence and it suggests the occurrence of the preferential sputtering of Sb and Te. The measured sputtering yields are reported in fig. 3.53(b). The X-ray spectra resulting from PIXE analysis of the same samples, shown in fig. 3.54(a), state that the Te/Sb ratio remains quite constant close to the stoichiometric value 2.5, fig.3.54(b).

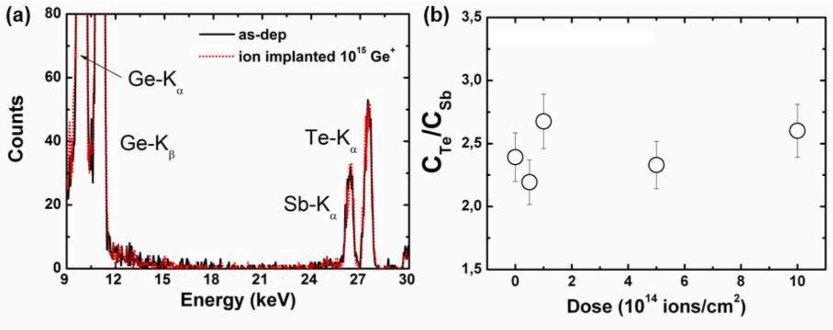

Figure 3.54 (a) PIXE spectra of the as-deposited and Ge$^+$ 10^{15} ions/cm^2 implanted GST uncapped samples. The He$^+$ beam has an initial energy of 2.7 MeV. The K$_\alpha$ lines of the different atomic species are clearly reported. (b) The Te/Sb concentration ratio, obtained by the PIXE measurements, is shown as function of the irradiation fluence (uncapped film).

We can then obtain the sputtering yield of the different atomic species: 0.9, 1.5, and 3.7 atoms/ion for Ge, Sb, and Te, respectively. Therefore, at high fluence, the Sb–Te preferential sputtering leaves the film surface richer in Ge. The surface binding energy is the key parameter that limits the sputtering yield. This is the energy that the atoms must overcome to leave the surface of the target. A rough estimation of this energy is the sublimation energy characteristic of each atomic species: Ge has a higher value (3.85 eV) with respect to Sb and Te (2.74 and 2.04 eV) [Kud05]. On the other hand it is known that the bond energy in the Ge–Sb–Te system is

higher for Ge–Te bonds (4.7 eV) with respect to the other bonds (~3 eV) [Wea97]. This consideration essentially supports the lower sputtering yield of Ge with respect to Sb and Te. Moreover, it is also possible to estimate the surface binding energy by the fit of the measured sputtering rate using the SRIM code. A good agreement between the calculated and measured sputtering yields is obtained using a surface energy of 3.2 and 4.8 eV for Sb–Te and Ge, respectively. We have also performed the same calculations by using the TRIDYN code and a fairly good agreement between the calculations and experimental data was obtained using the different sublimation energies as the surface binding energies. The Ge concentration in the sample implanted with 10^{15} ions/cm^2 is 24.5 atom% when compared with the value of 23 atom% of the as-deposited film. It must be noted that the different sputtering rates account for an increase of the Ge concentration that is about half of the measured one, while the remainder is due to the profile of the implanted Ge. It is known that by increasing the Ge concentration the crystallization temperature of the GST alloys increases and this may explain the increased stability of the high dose implanted samples in spite of the simultaneous local rearrangement of the amorphous structure . In fact, by varying the stoichiometry from $GeSb_2Te_4$ (Ge 14 atom %) to $Ge_2Sb_2Te_5$ (Ge 22 atom %), the crystallization temperature increases of 10°C [Yam91]. We measured a variation of the Ge concentration of ~1.5 atom %, and then an increase of the crystallization temperature of a few degrees Celsius is expected. On the other hand, the sputtering not only modifies the stoichiometry of the alloy but also reduces the thickness of the film. In our samples (20 nm thick), a reduction of the thickness by a couple of nanometers should induce an enhancement in the crystallization temperature of ~1°C [Che10]. These estimates are in good agreement with the values measured in the sample implanted with a dose of 10^{15} ions/cm^2.
In the capped samples an additional process related to the ion irradiation must be taken into account because during the Ge ion implantation some Si and O atoms in the SiO_2 cap layer recoil in the GST film, and the recoils distribution, estimated for a fluence of 10^{15} ions/cm^2 by SRIM calculation, is

shown in fig. 3.51(b.) The zero of the depth scale is set at the interface between the SiO_2 cap and the GST film. In the central region, between 4 and 16 nm, the concentration profiles of O and Si are well described by an exponentially decaying function with a characteristic length of about 9 nm. Extrapolation at depth below 4 nm is not feasible, because at this small distance one should take into account the collision mixing and the BCA breaks down. Recoil atoms originate from three different types: primary recoils, which are produced directly by primary ions; secondary recoils, which are produced with moderate energy by other recoils; and cascade recoils, which are produced at very low energy by a cascade process very near the interface. These have ranges of only a few nanometers but are produced in the greatest number and may enhance the near-surface concentration by orders of magnitude. However it is evident that the concentration of oxygen and silicon in the first nanometers inside the chalcogenide layer is above 4 and 2 atom%, respectively. This estimation is also confirmed by TRIDYN calculation performed under the same conditions. It has been reported that oxygen in GST at a concentration of 6 atom% increases the crystallization temperature by more than 10°C [Pri04][Pri07]. A content of silicon equal to 7 atom % produces an increase of about 25°C [Fen07]. The Si and O enrichment of the GST, due to recoil implantation, estimated in our samples is capable to reasonably take into account the enhanced thermal stability of the implanted samples with respect to the as-deposited one. The crystallization process is characterized by an heterogeneous nucleation at the interface between the GST and the upper layers (fig. 3.17), and after irradiation this region is heavily affected by the doping that then retards the crystallization process. The samples covered with the SiO_2 layer are not affected by the sputtering effect on the GST film because the cap layer is too thick to be fully eroded by the adopted fluencies (~1 nm of SiO_2 is expected to be sputtered at a fluence of 10^{15} ions/cm^2).

In conclusion, we have investigated the ion beam effects on stability, stoichiometry, and thickness of GST thin films, with and without a SiO_2 cap layer. In uncapped GST, the crystallization temperature initially decreases with fluence (sect. 3.6.2), whereas it increases for fluence higher than 10^{14} ions/cm^2. The behavior at low dose is due to the variations in the local order of the amorphous network achieved by the ion induced thermal spike effects (sect. 3.6.3) that promote the system to a state closer to the crystalline phase. The improved stability at a high fluence is caused by the thickness reduction and stoichiometry variation (richer in germanium) due to preferential sputtering. In the capped samples the progressive increase of the crystallization temperature with the implantation dose is due to the doping of GST with the oxygen and silicon recoiled atoms. Variations of the crystallization temperature consistent with a doping concentration of 5 atom% have been observed. The capping layer, present in the PCM devices, can be selected to introduce by recoil suitable doping species that affect the thermal stability of the GST layer by the formation of new atomic bonds. Recoil implantation may then be a useful and viable tool to obtain a thin doped chalcogenide layer in the future PCM devices.

References

[Abr65] N. K. Abrikosov, G. T. Danilova-Dobryakova, *Izv. Akad. Auk. SSSR Neorg. Mater.*, 1, 204 (1965).

[Ako11] J. Akola, J. Larrucea, R. O. Jones, *Phys. Rev. B*, 83, 094113 (2011).

[Bak06] D. A. Baker, M. A. Paesler, G. Lucovsky, S. C. Agarwal, P. C. Taylor, *Phys. Rev. Lett.*, *96*, 255501 (2006).

[Che10] H. Y. Cheng, S. Raoux, and Y. C. Chen, *J. Appl. Phys.*, 107, 74308 (2010).

[Dac11] F. d' Acapito, *Semicond. Sci. Technol.*, 26, 064004 (2011).

[Dac98] F. d'Acapito, S. Colonna, S. Pascarelli, G. Antonioli, A. Balerna, A. Bazzini, F. Boscherini, F. Campolungo, G. Chini, G. Dalba, I. Davoli, P. Fornasini, R. Graziola, G. Licheri, C. Meneghini, F. Rocca, L. Sangiorgio, V. Sciarra, V. Tullio, S. Mobilio, *ESRF Newsletter*, 30, 42-44. ISSN 1011-9310 (1998).

[Deb07] R. De Bastiani, A. M. Piro, M. G. Grimaldi, E. Rimini, *Nucl. Instrum. Methods Phys. Res. B*, 257, 572 (2007).

[Deb08] R. De Bastiani, A. M. Piro, M. G. Grimaldi, E. Rimini, G. A. Baratta, G. Strazzulla, *Appl. Phys. Lett.*, 92, 241925 (2008).

[Fen07] J. Feng, Y. Zhang, B. W. Qiao, Y. F. Lai, Y. Y. Lin, B. C. Cai, T. A. Tang, B. Chen, *Appl. Phys. A*, 87, 57 (2007).

[Fri01] I. Friedricha, V. Weidenhof, S. Lenk, M. Wuttig, *Thin Solid Films*, 389, 239 (2001).

[Gaw11] W. Gawelda, J. Siegel, C. N. Afonso, V. Plausinaitiene, A. Abrutis, C. Wiemer, *J. Appl. Phys.*, 109, 123102 (2011).

[Hof58] J.D. Hoffman, *Journal of Chemical Physics*, 29, 1192 (1958).

[Hub87] E. Huber, E. E. Marinero, *Phys. Rev. B*, 36, 1595 (1987).

[Jai11] I.P. Jain, G. Agarwal, *Surface Science Reports*, 66, 77–172 (2011).

[Jeo99] T. H. Jeong, M. R. Kim, H. S. Sang, J. Kim, S. Y. Kim, *J. Appl. Phys.*, 86, 774 (1999).

[Jov08] P. Jovari, I. Kaban, J. Steiner, B. Beuneu, A. Schops, M. A. Webb, *Phys. Rev. B*, *77*, 035202 (2008).

[Kal04] J. Kalb, F. Spaepen, M. Wuttig, *Appl. Phys. Lett*. 84, 5240 (2004).

[Kal05] J. Kalb , C. Y. Wen, F. Spaepen, H. Dieker, M. Wuttig *J. Appl. Phys.* 98, 054902 (2005).

[Kal05b] J. Kalb, F. Spaepen, M. Wuttig *J. Appl. Phys.* 98, 054910 (2005).

[Khu00] P. K. Khulbe, E. M. Wright, M. Mansurpir, *J. Appl. Phys.*, **88**, 3926 (2000).

[Khu00] P. K. Khulbe, E. M. Wright, M. Mansurpir, *J. Appl. Phys.*, 88, 3926 (2000).

[Kol04] A. V. Kolobov , P. Fons , A. I. Frenkel , A. L. Ankudinov , J. Tominaga , T. Uruga , *Nature Materials*, *3*, 703 (2004).

[Koo04] B. J. Kooi and J. Th. M. De Hosson, J. Appl. Phys. 95, 4714 (2004).

[Kud05] Y. Kudriavtsev, A. Villegas, A. Godines, R. Asomoza, *Appl. Surf. Sci.*, 239, 273 (2005).

[Kuw06] M. Kuwahara, O. Suzuki, N. Taketoshi, Y. Yamakawa, T. Yagi, P. Fons, K. Tsutsumi, M. Suzuki, T. Fukaya, J. Tominaga, T. Baba, Jpn. J. Appl. Phys., 45, 1419 (2006).

[Kuw07] M. Kuwahara, O. Suzuki, Y. Yamakawa, N. Taketoshi, T. Yagi, P. Fons, T. Fukaya, J. Tominaga, T. Baba, Jpn. J. Appl. Phys., 46, 3909 (2007).

[Lee81] P. A. Lee, P. H. Citrin, P. Eisenberg, B. M. Kincaid, *Rev. Mod. Phys.*, 53, 770 (1981).

[Lut98] L. Lutterotti and S. Gialanella, *Acta Mater.*, 46, 101 (1998).

[Mol84] W. Möller, W. Eckstein, *Nucl. Instrum. Methods Phys. Res. B*, 2, 814 (1984).

[Nas06] M. Nastasi, J.W. Mayer, *Ion Implantation and Synthesis of Materials*, New York (2006).

[Non00] T. Nonaka, G. Ohbayashi, Y. Toriumi, Y. Mori, H. Hashimoto, *Thin Solid Films*, 370, 258-261 (2000).

[Pin71] A. S. Pine and G. Dresselhaus, *Phys. Rev. B*, 4, 356 (1971).

[Poa82] J. M. Poate, J. W.Mayer, Laser Annealing of Semiconductors, Academic, New York (1982).

[Poa83] J. M. Poate, G. Foti, D. Jacobson, Surface Modification and Alloying by Laser, Ion, and Electron Beams, Plenum, New York (1983).

[Pri04] S. Privitera, R. Zonca, E. Rimini, *Appl. Phys. Lett.*, 85, 3044 (2004).

[Pri07] S. Privitera, E. Rimini, C. Bongiorno, A. Pirovano, R. Bez, *Nucl. Instrum. Methods Phys. Res.*, 257, 352 (2007).

[Rao10] S. Raoux, G. M. Cohen, R. M. Shelby, H. Y. Cheng, J. L. Jordan Sweet, *Mater. Res. Soc. Symp. Proc.*, 1251, H02 (2010).

[Rav05] B. Ravel, *J. Synchrotron Rad.*, 12, 537 (2005).

[Reh91] J. J. Rehr, J. Mustre de Leon, S. I. Zabinsky, T. C. Albers, *J. Am. Chem. Soc.*, 113, 5135 (1991).

[Shu70] R. Shuker, R. W. Gammon, *Phys. Rev. Lett.*, *25*, 222 (1970).

[Sim11] R. E. Simpson, P. Fons, A. V. Kolobov, T. Fukaya, M. Krbal, T. Yagi and J. Tominaga, Nature Nanotechnology 6, 501–505 (2011).

[Sos09] G. C. Sosso, S. Caravati, C. Gatti, S. Assoni, M. Bernasconi, *J. Phys. Condens. Matter*, 21, 245401 (2009).

[Sos11] G. C. Sosso, S. Caravati, R. Mazzarello, M. Bernasconi, *Phys. Rev. B*, *83* , 134201 (2011).

[Wea97] R. C. Weast, *CRC Handbook of Chemistry and Physics*, 78th ed., CRC Press, Cleveland, (1997).

[Yam87] N. Yamada, E. Obno, N. Akahira, K. Nishiuchi, K. Nagata, M. Takao*, Jpn. J. Appl. Phys. Part 1,* 26, 61 (1987).

[Yam91] N. Yamada, E. Ohno, K. Nishiuchi, N. Akahira, M. Takao, *J. Appl. Phys.*, 69, 2849 (1991).

[Zie85] J. F. Ziegler, J. P. Biresack, U. Littmark, *The Stopping and the Range of Ions in Solids*, Pergamon, New York, (1985).

Chapter 4

Phase transitions in Ge_xTe_{1-x}

Stoichiometric GeTe, in 1986, was the first single phase material that exhibit better phase change properties with respect to the corresponding eutectic alloy: the crystallization time by laser irradiation decreases from 100µs to 50ns whereas the crystallization temperature increases from 160°C to 180°C with respect to the eutectic composition, fig. 4.1 [Che86]. Recently, the binary compounds Ge_xTe_{1-x} have attracted again great attention for high temperature applications (especially automotive application) since they present significant improvement of data retention at high temperature compared to commonly used GST and an excellent contrast in terms of electrical resistivity between the two states, fig. 1.11.

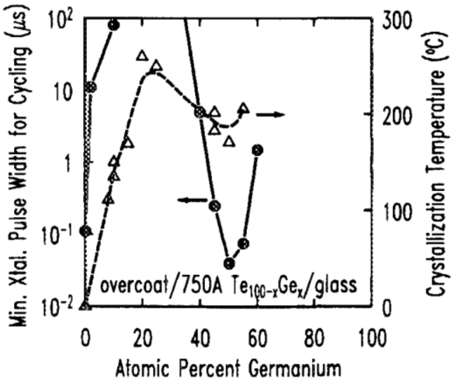

Figure 4.1 **Minimum crystallization laser pulse width and crystallization temperature as function of Ge concentration in Ge_xTe_{1-x} alloys [Che86].**

Moreover phase transitions on the nanosecond time scale are possible for GeTe alloys using laser or current pulses of proper duration and intensity [Bru09][Rao09]. In this scenario, stoichiometric GeTe seems to be a good candidate as active medium in PCM devices. Varying the stoichiometry of the GeTe alloy, it is possible to improve the stability of the amorphous phase but the higher crystallization temperature is generally coupled with a lower crystallization rate. Even though some papers are present in the literature on the phase transitions in non-stoichiometric GeTe alloys, several details on the physical processes involved during these transitions are still unknown [Oka86][Rao09b].

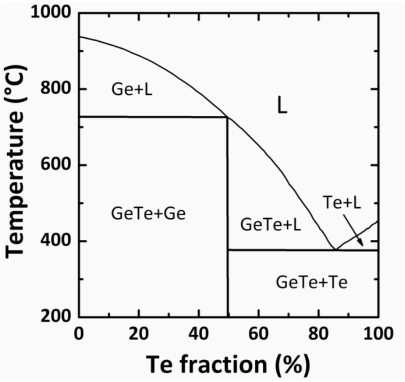

Figure 4.2 **Phase diagram of the binary Ge-Te system [Che86].**

The phase diagram of the Ge-Te system reported in fig. 4.2 foresees only the GeTe as stable phase so that the precipitation of the excess species is expected during the crystallization process of amorphous non stoichiometric alloys [Han58]. In spite of the large influence that the precipitation process can have on the phase change kinetics of GeTe alloys a detailed description of the interplay between the precipitation and crystallization is missing. Moreover, even small deviation from the stoichiometry can give rise during the device cycling to significant local variation of stoichiometry that could become a source of failure in PCM devices [Nam09][Kim09]. This phenomenon is not well described in the literature although it strongly affects the phase changing kinetics. In this chapter we report on the crystallization process of both stoichiometric and non-stoichiometric Ge_xTe_{1-x} alloys (x=0.36, 0.51 and 0.63) using several in situ and ex situ techniques: time resolved reflectivity (TRR), Raman spectroscopy, transmission electron microscopy (TEM) and X-ray diffraction

(XRD) in such a way to achieve a full comprehension of the relevant parameters affecting the transformation. On the other hand, we will first describe the sample preparation and the characterization of the as deposited amorphous films. In section 4.3.5 we will discuss the re-crystallization of ion and laser amorphized samples looking to the effect of phase separation on this phenomenon. Finally, as discussed in par. 3.6. in the case of GST, we will discuss the local rearrangement and the consequent variation of crystallization kinetics of ion and laser irradiated Ge_xTe_{1-x} alloys.

4.1 Sample preparation

Amorphous Ge_xTe_{1-x} (x=0.36, 0.51 and 0.63) films, 50 nm thick, were deposited at room temperature on thermally grown SiO_2 layer using a rf magnetron co-sputtering from elemental targets. The concentration of Ge and Te in the alloy was varied by changing the applied rf powers.

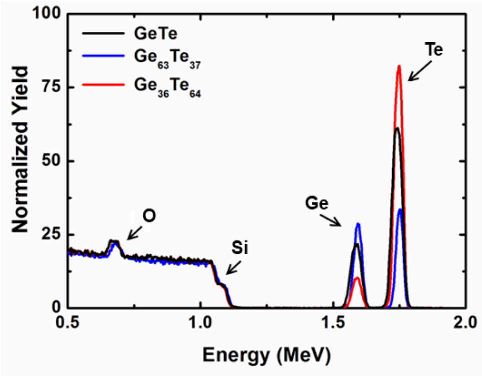

Figure 4.3 **RBS spectra of as deposited 50 nm Ge_xTe_{1-x} film.**

The stoichiometry and the thickness of the amorphous films were evaluated by 2.0 MeV He^+ Rutherford backscattering spectrometry, fig. 4.3. A density $\rho=5.60\ g/cm^3$ has been assumed in the calculation. The peak at high energy is due to Te atoms, whereas that at low energy is related to the backscattering from Ge atoms, according to the different kinematical factors. The low energy spectrum is due to the SiO_2/Si substrate. More details on the experimental setup are contained in section 3.1.

4.2 Local order of the as deposited amorphous phase

In the last years, as described in sect. 1.4, many efforts have been dedicated to the investigation of the local order in Ge_xTe_{1-x} alloys. In particular, *ab initio* simulations coupled with Raman spectroscopy analyses pointed out the main features of the amorphous network in the case of stoichiometric GeTe. Mazzarello *et al.* suggested that, similarly to previous results on a-GST (sect. 1.4 and 3.2), Ge atoms are mostly fourfold coordinated, while Te atoms are mostly threefold coordinated [Maz10]. All Te and 77% of Ge atoms are in a defective octahedral-like geometry with octahedral bonding angles (~90°) but a lower than six coordination. In the defective octahedral geometry, Ge atoms form three shorter bonds in a 3+n (n=0-2) geometry similar to that of crystalline trigonal GeTe (sect. 1.3.1).

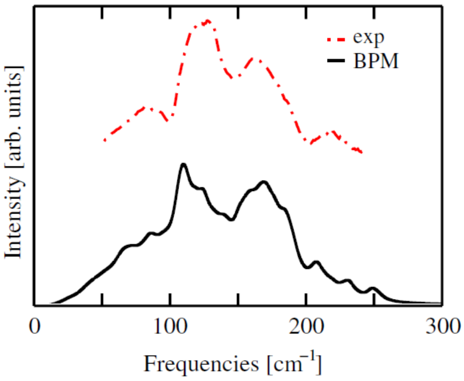

Figure 4.4 **Experimental and calculated Raman spectra of amorphous stoichiometric GeTe [Maz10].**

Some Ge atoms are tetrahedrally coordinated, as also inferred from EXAFS data [Kol04], although only in the fraction of ~25%. The distribution of different tetrahedral units shows that the tetrahedral coordination of Ge is favored by homopolar Ge-Ge bonds, as occurs in amorphous GST. There are no chains of Te atoms but a few dimmers in this calculated melt quenched amorphous structure of stoichiometric GeTe. According to this model, they have simulated the corresponding Raman spectrum and the results are reported in fig. 4.4 [Maz10]. Insight on the phonons responsible for the different Raman peaks is gained from the analysis of the reduced Raman spectra projected on tetrahedra, octahedra and different type of atoms reported in fig. 4.5.

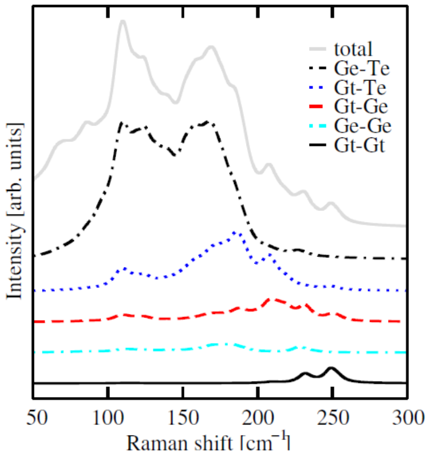

Figure 4.5 **Calculated Raman spectrum of amorphous stoichiometric GeTe projected on tetrahedral (Gt-), octahedral (Ge-) and different atomic species [Maz10].**

Tetrahedral Ge atoms dominate the spectrum above 200 cm^{-1} and contribute (albeit marginally) also to the 170-200 cm^{-1} range. Octahedral-like bonds dominate instead the spectrum below 200 cm^{-1}. the projections of the Raman spectrum on bending and stretching-like displacements of Ge and Te atoms show a marginal predominance of stretching-like (bending-like) vibrations in the Raman peak at 175 cm^{-1} (110 cm^{-1}). It must be noted that these calculations refer to a melt quenched amorphous. As in the case of as deposited amorphous GST, we believe that the presence of Te-Te dimers and trimers contributes to the intensity of the band at ~125 cm^{-1}. In fact, it is known that crystalline Tellurium has the strongest Raman peak at 122 cm^{-1} (the second peak is at ~140 cm^{-1}) [Pin71]. Moreover, crystalline Te exhibits a very high Raman cross section and then Raman spectroscopy is a powerfull tool to detect the presence of Te-Te bonds. On the other hand, has been demonstrated that the abundance of homopolar bonds is higher in as deposited amorphous phase change materials with respect to melt quenched amorphous [Ako11].

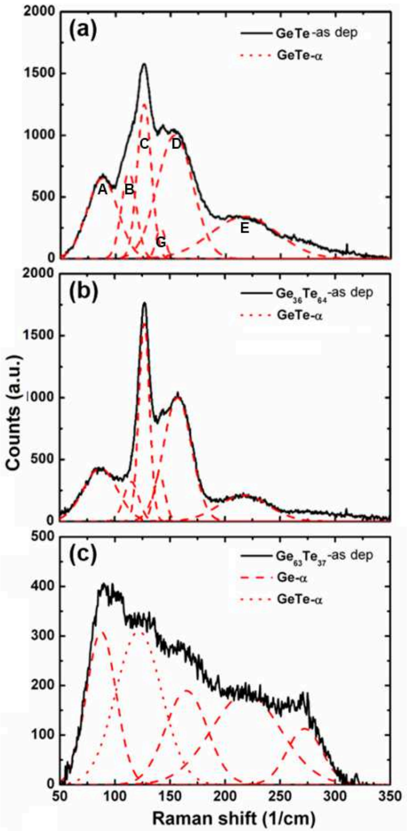

Figure 4.6 Raman spectra of several amorphous Ge_xTe_{1-x} alloys: GeTe (a), $Ge_{36}Te_{64}$ (b), $Ge_{63}Te_{37}$ (c).

We have performed Raman spectoscopy analyses on both stoichiometric and non-stoichiometric samples and the results are reported in fig. 4.6. The spectrum of as deposited GeTe is similar to both the experimental and theoretical spectra reported in fig. 4.4. The fit of the data required five main Gaussian contributions, denoted A, B, C, D, and E visible in the same figure (red dashed lines). The fitting parameters (peak position, width, and normalized area) of the raw Raman data are summarized in Table 4.1. The presence in the spectrum of a small band at ~140 cm^{-1} (G peak) confirms the significative presence of homopolar Te-Te bonds since it is known that at this wavenumber the second peak of crystalline Te appears. As we discussed in sect. 3.2.2, it is not possible to quantify the abundance of the different bonds in amorphous alloys looking to the Raman spectrum since it has been demonstrated that, because the coupling of the vibrations to light is not constant for all vibrational modes, Raman spectroscopy on amorphous materials yields a "weighted" density of states, for which the weighting is not accurately known. On the other hand, meaningful information can though be obtained as we will show discussing about non stoichiometric alloys.

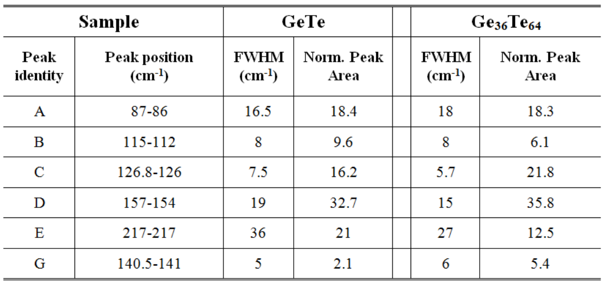

Sample		GeTe		$Ge_{36}Te_{64}$	
Peak identity	Peak position (cm^{-1})	FWHM (cm^{-1})	Norm. Peak Area	FWHM (cm^{-1})	Norm. Peak Area
A	87-86	16.5	18.4	18	18.3
B	115-112	8	9.6	8	6.1
C	126.8-126	7.5	16.2	5.7	21.8
D	157-154	19	32.7	15	35.8
E	217-217	36	21	27	12.5
G	140.5-141	5	2.1	6	5.4

Table 4.1 Peak parameters (position, width, and normalized area), as determined through fits of the experimental data of as deposited amorphous GeTe and $Ge_{36}Te_{64}$ samples.

The Raman spectrum of Te-rich sample is similar to that of stoichiometric GeTe, fig. 4.6(b). Peaks wavenumber positions and the assignment of each peak to a particular vibrational mode are the same as those reported for GeTe. The main difference is related to the intensity of peak C that is 34% more intense increasing the Te concentration, tab.4.1. It could be related to an increase in the abundance of homopolar Te-Te bonds since, according to the stoichiometry, a 40% of Te atoms should be bound to another Te atom.

On the other hand it is interesting to note a reduction of peak E intensity (-60%). This peak is related to the presence of homopolar Ge-Ge bonds, fig. 4.5, and its reduction is consistent with an increase (decrease) of Te (Ge) concentration. Figure 4.6(c) reports the Raman spectrum of the Ge rich sample: the signal extends from $70cm^{-1}$ to $300cm^{-1}$ in the characteristic region of amorphous germanium [Des01]. It is possible to distinguish the transversal acoustic (TA $90cm^{-1}$) and optical (TO $280cm^{-1}$) modes of α-Ge. These two peaks are not well defined and the signal to noise ratio is low. Both the longitudinal acoustic ($160cm^{-1}$) and optical ($240cm^{-1}$) α-Ge modes are required to fit this spectrum whereas the peak at $125cm^{-1}$ is assignable to α-GeTe structures. These features may be due to the low Te concentration that favors the formation of highly distorted $GeGe_4$ tetrahedra. There is no evidence of peaks due to the crystalline Ge ($300cm^{-1}$) [Des01] or GeTe ($89cm^{-1}$ and $118cm^{-1}$) modes.

4.3 Crystallization Process

We have studied the crystallization process of both stoichiometric and non-stoichiometric alloys. Unlike GeSbTe alloys, stoichiometric GeTe shows a growth-dominated crystallization. Under these conditions, to study the amorphous-crystal transition, it’s then necessary an optical microscope (with an optical resolution ~1 µm) rather than a transmission electron or atomic force microscope. The change in reflectivity is used to distinguish the formation of crystalline grains within the amorphous background. Nucleation and growth rates of as deposited samples can be measured in a wide area (about 5×10^4 μm^2) and from these data, the activation energy and pre-exponential terms of each process can be calculated. These results have been already reported in table 2.2 and analyzed in section 2.2.2. Anyway we will tackle this topic again in sect. 4.4.1. Here we will discuss then the case of non stoichiometric alloys. We have studied the crystallization process using several in situ and ex situ techniques: time resolved reflectivity (TRR), Raman spectroscopy, transmission electron microscopy (TEM) and X-ray diffraction (XRD) in such a way to achieve a full comprehension of the relevant parameters affecting the transformation. The results, if possible, are compared with those of stoichiometic GeTe. Looking to the phase diagram of fig. 4.2, the precipitation of the excess atomic species is expected to play a relevant role during the crystallization of non stoichiometric alloys. The time resolved reflectivity curves recorded during the annealing of the Ge_xTe_{1-x} films (x=0.36, 0.51, 0.63) are reported in fig. 4.7. A constant heating ramp of 6° C/min was used.

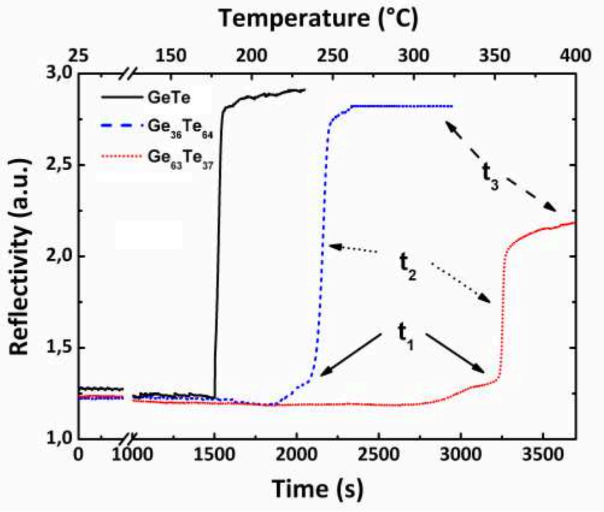

Figure 4.7 Time resolved reflectivity measurements, during an heating ramp of 6 °C/min, of three different Ge_xTe_{1-x} alloys (x=0.36, 0.51, 0.63). We prepared three samples, for both the non-stoichiometric composition, by stopping at different times the annealing process. The arrows point to these different times.

The enhancement of reflectivity observed during the annealing process is due to the transition from the amorphous to the crystalline phase. The crystallization temperature of the Ge-rich alloy (dotted red line) was 354 °C, higher than those of the Te-rich alloy (244°C, dashed blue line) and of the stoichiometric GeTe (180°C, solid black line). In the non-stoichiometric alloys, the reflectivity vs temperature curves show, before the rise due to the crystallization, an intermediate step, labeled t_1 in fig. 4.7, that it will be shown to be linked to the precipitation of the excess atomic species. To get insights into the structural and morphological modifications occurring during the annealing, we prepared different samples stopping the process at some relevant points labeled t_1, t_2, and t_3 in fig. 4.7. As already anticipated, t_1 is the time at which the first enhancement of the reflectivity occurs (solid arrows), t_2 is the time at which the reflectivity reaches a value half-way between the initial and the final values, and t_3 is the time at which the reflectivity signal reaches the steady state value (dashed arrows). These samples were then analyzed by Raman Spectroscopy, TEM and XRD.

4.3.1 Te-rich alloy

In this paragraph we present a detailed description of the evolution of the Te-rich alloy during the annealing process. The samples were prepared by changing the annealing duration from t_1 to t_3 (fig.4.7). Figure 4.8(a) reports again the Raman spectrum of the as deposited amorphous film. The problem of the interpretation of the Raman signal has been discussed in the sect. 4.2. Here Raman spectroscopy is just a tool to distinguish between the different phases. The Raman spectrum of the sample annealed up to the time t_1 (first step in the reflectivity curve) reported in fig. 4.8(b) shows the presence of two additional bands at $122cm^{-1}$ and $142cm^{-1}$ (green dotted line in the figure) with respect to that of the as-deposited film. These two peaks are associated to the vibrational modes of crystalline tellurium [Pin71]. Therefore, at this stage of the annealing process the crystalline tellurium precipitates coexist with the amorphous regions. The corresponding XRD pattern, fig.4.9(a) solid line, shows sharp and intense peaks deriving from crystalline Tellurium [Wyc63] while the (100) and (110) peaks of crystalline GeTe [Non00] are barely visible, overlapped with the broad band of the residual amorphous regions. No detectable change of either position and shape of the amorphous signal are produced by this thermal treatment as can be inferred from the comparison of the XRD pattern of the annealed and of the as deposited sample (red dotted line) reported in the same figure.

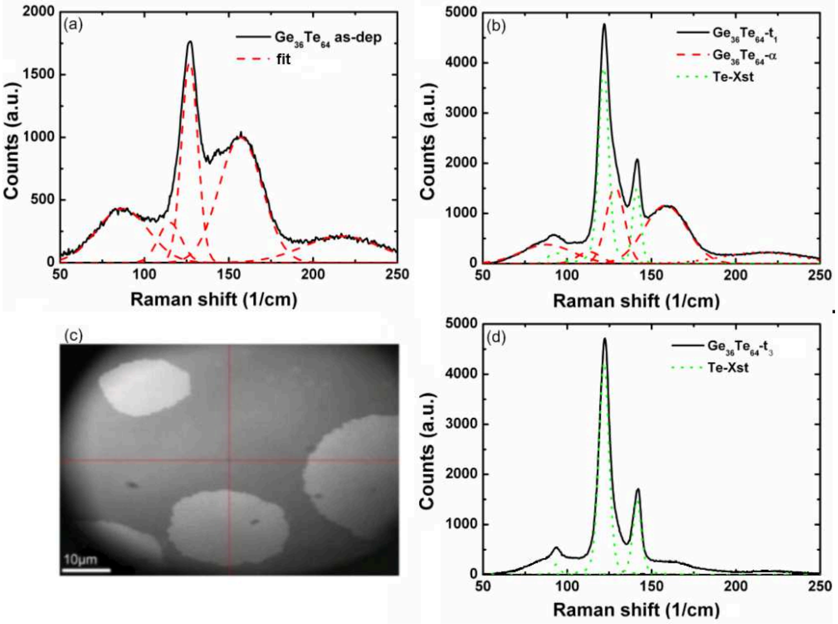

Figure 4.8 (a)(b)(d) Raman spectra of the Te-rich alloy at different times of the annealing process: as deposited, first stair of the reflectivity curve (time t_1) and complete crystallization (time t_3). (c) Optical micrograph of a partially crystallized $Ge_{36}Te_{64}$ film (time t_2). The Raman spectrum within the brighter grains is the same of fig.4.8(d) whereas outside it is the same of fig.4.8(b).

The bright field TEM image, fig. 4.10(a), of the same sample indicates that, at this stage, the Te-rich sample consists of an amorphous film containing rectangular grains that the electron diffraction pattern confirmed to be crystalline Te grains. Therefore, the comparison between Raman, XRD and TEM analyses unambiguously demonstrate that the formation of crystalline Te precipitates is the first step during the annealing of Te-rich alloy. The change observed at the time t_1 in the TRR curve is then related to this phenomenon. We discuss now the features of the sample annealed up to the time t_2 when the reflectivity reaches a value halfway between the amorphous and the crystal. Figure 4.8(c) shows a 50x optical image of the sample surface. Some micrometric grains brighter with respect to the background are clearly visible and resembles those observed in partially crystallized stoichiometric GeTe film. This is typical of a crystallization limited by a low nucleation rate, characteristic of this compound, in which the few nucleated crystallites grow up generating micrometric crystalline domains.

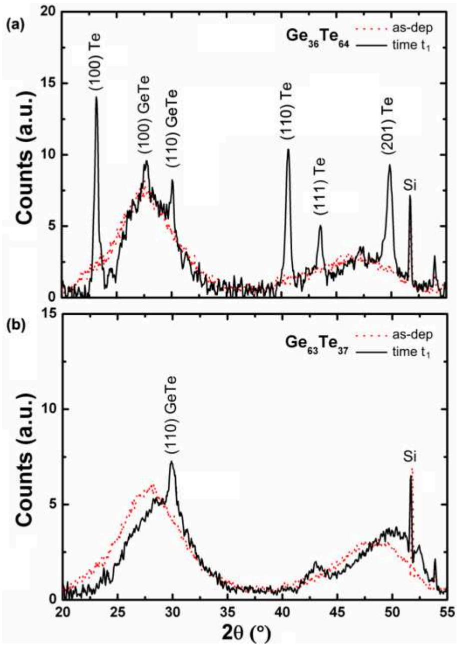

Figure 4.9 (a), (b) X-ray diffraction pattern of as deposited (red dotted line) and annealed till the time t_1 (solid line) $Ge_{36}Te_{64}$ and $Ge_{63}Te_{37}$ samples.

The Raman spectrum, fig. 4.8(d), inside these grains shows peaks associated to the crystalline Tellurium modes without the band at 160 cm^{-1} characteristic of the amorphous film while outside these grains it coincides with that shown in fig. 4.8(b), relative to the sample annealed up to the time t_1. As will be shown below, the formation of these micrometric grains is associated to the GeTe crystallization although this statement cannot be supported by Raman analyses since the signal of crystalline GeTe, characterized by two bands centred at 89cm^{-1} and 118cm^{-1} respectively (fig.4.27), is hidden by the near very intense crystalline Te bands. Figure

4.10(b) shows the bright field TEM image of a micrometric grain. The associated diffraction pattern (not shown) exhibits rings due to crystalline Te and GeTe whereas outside the grain only the crystalline Te rings are visible (overlapped to a broad ring due to the amorphous). We can then conclude that the second step during the crystallization process of the Te-rich alloy is the formation of micrometric crystalline GeTe grains.

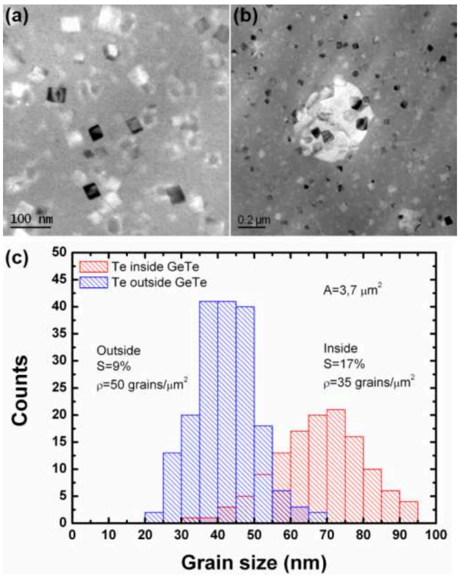

Figure 4.10 (a), (b) Bright field TEM micrographs of the Te-rich film at the annealing time t_1 and t_2, respectively. (c) Histogram of Te precipitates grain size inside and outside GeTe crystalline domains.

It is interesting to note that the average size of the crystalline tellurium grains inside the GeTe crystalline domains is greater than in the adjacent amorphous regions whereas their surface density exhibits instead an opposite trend, as shown in fig. 4.10(b). To quantify this effect we performed a similar analysis in a sample subjected to an isothermal annealing at 220°C (for 150 min) and the size distributions inside and outside the GeTe crystalline grains are reported in fig. 4.10(c). The Te precipitates cover a fraction of the sample surface equal to ~10% and ~20%

outside and inside the GeTe grains, respectively. The average grain size and density vary from 40nm to 70nm and from 50 to 35 grains/μm^2, respectively thus supporting the occurrence of a ripening during the crystallization of the GeTe. The atomic interdiffusion coefficient can be roughly estimated assuming a diffusion length equal to half of the average distance between the precipitates and a diffusion time equal to the rise time of the reflectivity curve (from 10% to 90% of the whole reflectivity variation). It comes out with a value of ~5.5×10^{-15} cm^2/s and ~8.0×10^{-15} cm^2/s in amorphous and crystalline GeTe, respectively; very similar to that measured for Te self diffusion in crystalline phase [Gho67].

4.3.2 Ge-rich alloy

We describe now the crystallization process of the Ge-rich alloy. Figure 4.11(b) reports the Raman spectrum of the sample annealed up to the time t_1: as in the case of as deposited film, the signal extends from 70cm^{-1} to 300cm^{-1} in the characteristic region of amorphous germanium [Des01]. It is possible to distinguish the transversal acoustic (TA 90cm^{-1}) and optical (TO 280cm^{-1}) modes of α-Ge. These two peaks are well defined and more intense with respect to that of the as deposited sample, fig.6(a), in which the Raman spectrum is a broad asymmetric bump. The longitudinal acoustic (160cm^{-1}) and optical (240cm^{-1}) α-Ge modes are required to fit these spectra whereas the peak at 125cm^{-1} is assignable to α- GeTe structures. The ratio between the integrated intensity of TA and TO peaks is an index of the local disorder within the amorphous Ge matrix: a higher I_{TA}/I_{TO} value is indicative of a less ordered network [Des01][Mor95]. This ratio, measured in an as-deposited α-Ge film (prepared for comparison) and in the annealed still amorphous $Ge_{63}Te_{37}$ film, amounts to 0.72 and to 1.68 respectively. Moreover, the distortion of the Ge-Ge bond angle can be estimated from the FWHM of the TO (280cm^{-1}) peak [Mor95]: it amounts to 0.8° in the as-deposited α-Ge sample and it reaches 2.4° in the $Ge_{63}Te_{37}$ film annealed at t_1. This suggests the formation of highly disordered and distorted amorphous germanium precipitates during the initial stage of the annealing of the Ge-rich alloy.

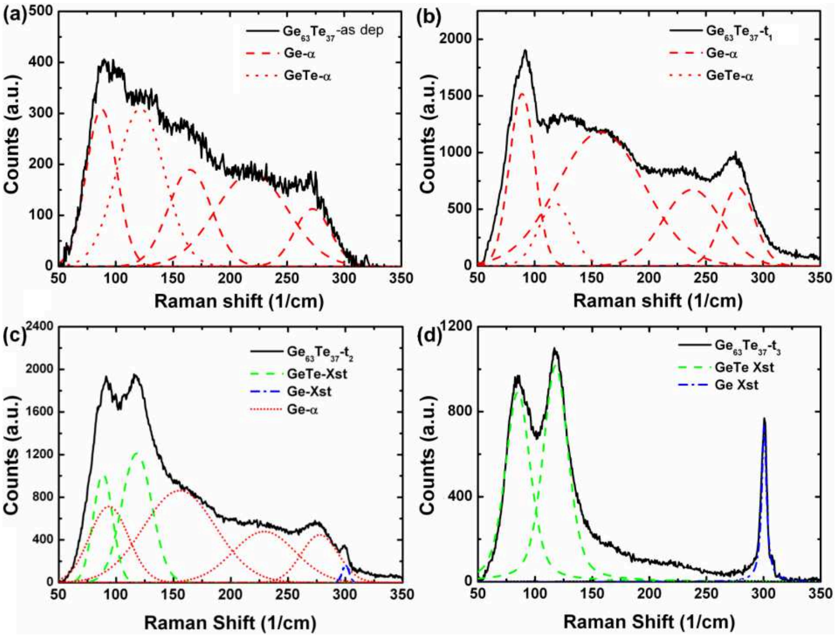

Figure 4.11 **(a), (b), (c), (d) Raman spectra of the Ge-rich alloy at different times of the annealing process: as deposited, first stair of the reflectivity curve (time t_1), half of the variation of reflectivity (time t_2) and complete crystallization (time t_3).**

Further XRD and TEM analyses support this statement. The XRD pattern of the annealed (time t_1) $Ge_{63}Te_{37}$ film reported in fig. 4.9(b) shows, in fact, the broad peaks typical of the amorphous phase and, superimposed, a single peak due to the (100) GeTe planes [Non00]. In the same figure is reported the XRD pattern of the as deposited film and it is evident that the broad peak centered at 28° in the as deposited material shifts of about +2° in the annealed sample thus indicating that some rearrangement of the local order of the amorphous phase occurs during the thermal treatment. The rhombohedral GeTe is the first observed crystalline phase. The modifications in the Ge-rich amorphous phase were also explored by in situ energy filtered TEM analysis, at 330°C. In conventional bright field images the contrast between the amorphous Ge and the matrix is poor. On the other hand, the background subtracted chemical maps require too much time with respect to the speed of *in situ* evolution of the system.

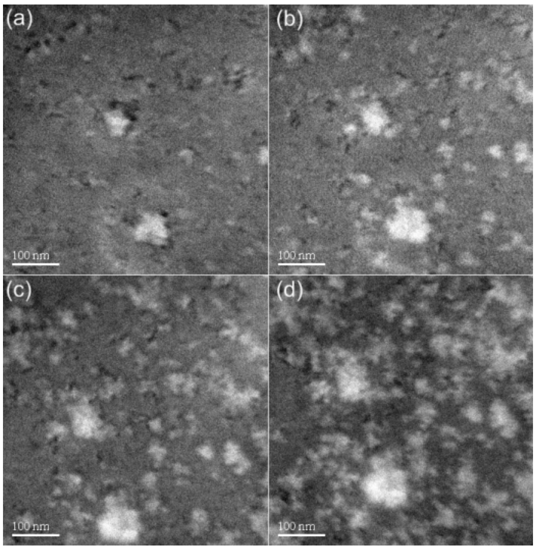

Figure 4.12 **(a), (b), (c), (d) Energy filtered TEM (255eV) of the $Ge_{63}Te_{37}$ film during an in situ annealing performed at 330°C. The brighter regions are richer in Germanium with respect to the background.**

To overcome this problem, we performed a contrast vs energy calibration using a fully crystallized sample. Several images were acquired at different energy loss and, by comparison with chemical maps, the best image contrast was found to be at 255eV energy loss. Under this condition, amorphous Ge clusters are clearly visible within the matrix and appear brighter than the background. A sequence of filtered TEM images is reported in fig.4.12. The formation and growth of Ge rich areas (bright area in the images) with increasing the annealing duration is evident whereas the background becomes gradually poorer in Ge (dark). A rough estimation of the surface fraction covered by the Ge precipitates can be achieved by the analysis of the EF-TEM images: in fig. 4.12(a) and (b) about the ~10% of the surface is covered by Ge-rich areas whereas in fig. 4.12(c) and (d) this value rises to ~20%. The average size of the precipitates is ~35 nm, and their surface density increases from ~130 to ~170 grains/μm^2 during the annealing process. From this the atomic interdiffusivity at 330°C is estimated to be ~4x10^{-14} cm^2/s. This value is much higher than that observed, at the same temperature, for Ge self-diffusion in crystalline phase [Hug08] (~2x10^{-25} cm^2/s) and then Te is probably the diffusing species also in this Ge-rich alloy. It must be noted that the present value has been measured at a higher annealing temperature (330°C against 220°C) with respect to the previous estimation in the Te-rich alloy (~5,5x10^{-15} cm^2/s).

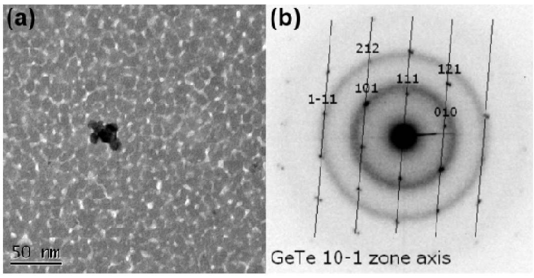

Figure 4.13 **(a), (b) Bright field TEM and the corresponding diffraction pattern of a GeTe crystalline grain within a Ge-rich film annealed till the time t_2.**

The Raman spectrum of the Ge-rich sample annealed up to the time t_2, fig. 4.11(c), shows peaks due to crystalline GeTe (89 cm^{-1} and 118 cm^{-1}) and Ge (300 cm^{-1}) [Des01], although a signal due to α-Ge (TO mode is clear at 280cm^{-1}) is still present. At the end of the crystallization process, fig.4.11(d) (time t_3), the bands of the amorphous phase disappear whereas the peaks of the crystalline phase are well defined. The partially crystallized films have been also analyzed by conventional TEM. The bright field image of a region containing a small crystalline grain (~40 nm) is shown in fig. 4.13(a) together with the corresponding electron diffraction pattern, fig. 4.13(b), that shows spots characteristic of crystalline GeTe coupled with the rings of the amorphous phase. Figure 4.14(a) shows the image of a larger (~150nm in size) crystalline grain whose diffraction pattern exhibits diffraction spots, fig. 4.14(b), from both crystalline Ge and GeTe. The dark field micrographs reported in fig. 4.14(c) and (d) were obtained by selecting two diffraction spots unambiguously associated to the GeTe and Ge crystal structures, respectively.

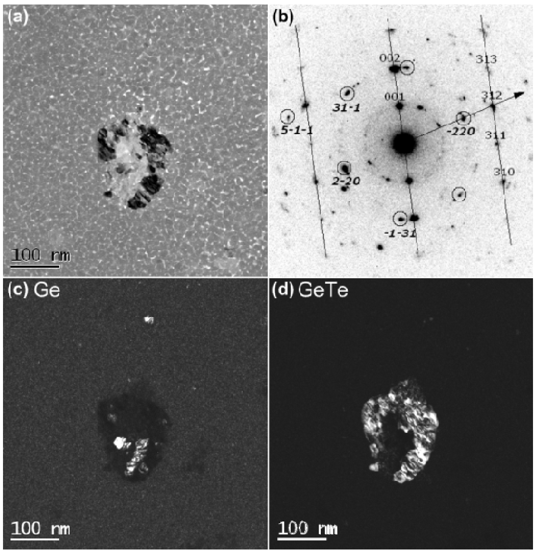

Figure 4.14 (a)(b) Bright field TEM and the corresponding diffraction pattern of a crystalline grain within a Ge-rich film annealed till the time t_2. Both GeTe (lines) and Ge (circles) crystalline peaks are present and, as indicated by an arrow, an alignment is clear between GeTe and Ge diffraction patterns. (c)(d) We have selected by a slit the diffraction peaks due to crystalline Ge or GeTe and the different crystalline regions are clearly visible.

As observed in several areas of the sample, the Ge precipitates are nestled inside the GeTe grains and they look to have some aligned crystal orientations. A detailed analysis of the diffraction pattern in fig. 4.14(b) reveals the coexistence of two zone axis, one for each phase. The alignment of the [-220] Ge crystallographic direction with [312] GeTe ones, as shown by the arrow, suggests an epitaxial relation between the two crystals. To summarize: the rhombohedral GeTe is the first crystalline phase that forms during the annealing of the Ge-rich alloy whereas the amorphous Ge precipitates, formed at the initial stage (t_1) of the annealing process, crystallize epitaxially using the GeTe crystals as a seed. This accounts for the temperature at which these processes occur, in fact, the crystallization temperature of the Ge-rich alloy, ~350°C, is too low to permit Ge crystallization by nucleation and growth (in α-Ge at 350°C $N_{rate}<10^{-6}$ grains/s/μm^3) [Ger79] but it is high enough to allow the epitaxial growth on a crystalline seed, being the epitaxial growth rate of amorphous Ge 0.1 nm/s at this temperature [Joh08].

4.3.3 Fully crystallized samples

We have analyzed the structure of crystalline stoichiometric GeTe in par. 1.3 and then here we complete discussing the case of non-stoichiometric samples at the end of the crystallization process (time t_3). Figure 4.15 reports XRD patterns and bright field TEM images of Te-rich (*a* and *b*) and Ge-rich samples (*c* and *d*), respectively. The peaks present in the XRD pattern of the Te rich sample, fig. 4.15(a), are due to crystalline Tellurium [Wyc63] and GeTe [Non00], as expected on the basis of the phase diagram of fig. 4.2. Peaks assignment is reported inside the figures. However the relative peak intensity differs from that expected for a random crystallite distribution, and in particular the (101) peak is barely visible whereas it should be the most intense. Further XRD analyses performed in Bragg-Brentano configuration indicated that a partial texture along the (100) direction is responsible for the above discussed peak intensity. The micrograph of fig. 4.15(b) shows the presence of rectangularly shaped dark crystalline regions surrounded by a crystal of different contrast. There aren't residual amorphous areas. The electronic diffraction pattern exhibits both Te and GeTe crystalline rings although the rings are too close to generate a selected area diffraction image. As we have shown in the previous section the dark regions are nanometric crystalline Te grains embedded in a micrometric GeTe crystal. The images in the second row of fig. 4.15 refer to the Ge-rich sample. The bright field TEM, fig. 4.15(d), shows a fully crystallized film. The electronic diffraction pattern exhibits both Ge and GeTe crystalline peaks but again it is not possible to distinguish by selected area diffraction the two different phases. The XRD pattern in fig. 4.15(c) clearly exhibits peaks due to the simultaneous presence of crystalline Germanium [Coo62] and GeTe [Non00].

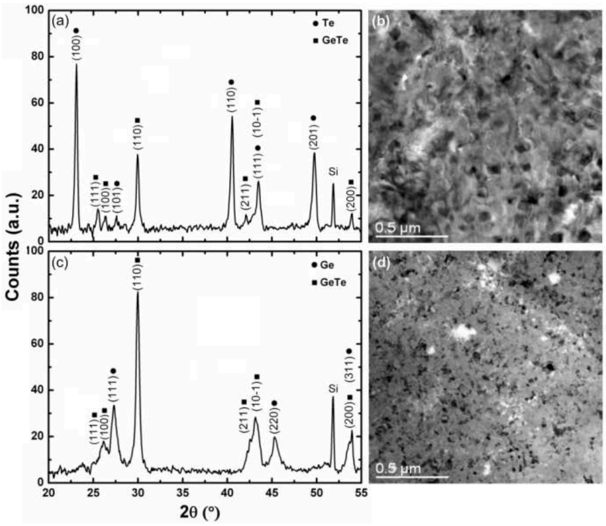

Figure 4.15 (a) X-ray diffraction pattern of a full crystallized $Ge_{36}Te_{64}$ film (time t_3). Both GeTe and Te peaks are clearly visible. (b) Bright field transmission electron micrograph of the Te-rich alloy at the end of the phase transition. (c) X-ray diffraction pattern of a full crystallized $Ge_{63}Te_{37}$ film. Both GeTe and Ge peaks are clearly visible. (d) Bright field TEM of the Ge-rich sample at the end of the phase transition.

Here the relative intensities of the peaks follow those expected from a powder of crystalline Ge and GeTe and no evidence of texture was obtained by XRD analysis in Bragg-Brentano configuration. Therefore, as expected looking to the phase diagram (fig. 4.2), the fully crystallized films of both Te-rich and Ge-rich samples consist of GeTe and precipitates of the atomic species in excess.

4.3.4 Dynamics of crystallization

The merge of the morphological and crystallographic analysis so far reported with isothermal TRR measurements allows the determination of the relevant parameters controlling the crystallization of both stoichiometric and non stoichiometric alloys. In stoichiometric GeTe the parameters related to the nucleation and growth of the crystalline grains, as well as the corresponding activation energies and preexponential factors, are correlated to the results of TRR measurements assuming the JMAK model [Rui02]. In non-stoichiometric alloys, the TRR curves indicate the occurrence of at least two processes: precipitation of the atomic species in excess and crystallization of the two separated phases (Te and GeTe, Ge and GeTe respectively). In addition, the change in reflectivity is mainly associated to the crystallization of GeTe rather than to the other phase transition. Figure 4.16 shows the TRR curves recorded on both stoichiometric and non-stoichiometric alloys in the temperature range in which the transformation occurs. The settled temperature was reached at the time t_0. As pointed out, in non stoichiometric samples, the first enhancement of the reflectivity is associated to the precipitation of the atomic species in excess. In the Ge-rich film the precipitation starts already during the heating ramp and then the first bump on the TRR characteristics appears always at the same time. Nevertheless, we could still define the crystallization time (τ) as the time at which the maximum of the first derivative of the reflectivity vs time curve occurs. It corresponds to a GeTe crystalline fraction of about 0.5. This physical quantity is temperature (T) dependent by an exponential law according to the equation

$$\tau(T) = \tau_0 exp\left(\frac{E_A}{k_B T}\right)$$

where k_B is the Boltzmann constant. The values of E_a and τ_0 have been extracted by the linear fit of the ln(τ) data as function of $1/k_BT$. The fitting results are summarized in table 4.2. It is interesting to note that in both the non-stoichiometric Ge_xTe_{1-x} alloys the crystallization is characterized by similar activation energy, ~3.3eV, higher than the value measured in stoichiometric GeTe, 2.9eV. In diffusion-controlled reactions, this physical quantity, measured with similar methods, gives an estimation of the activation energy of the diffusion process [Col96]. As a matter of fact, for x=0.37 and 0.64, the crystallization process is triggered by the precipitation of the atomic species in excess that occurs also during the GeTe crystallization. This behavior could explain the higher activation energy measured in the non-stoichiometric alloys since probably we measure a combination of the activation energies of precipitation and crystallization.

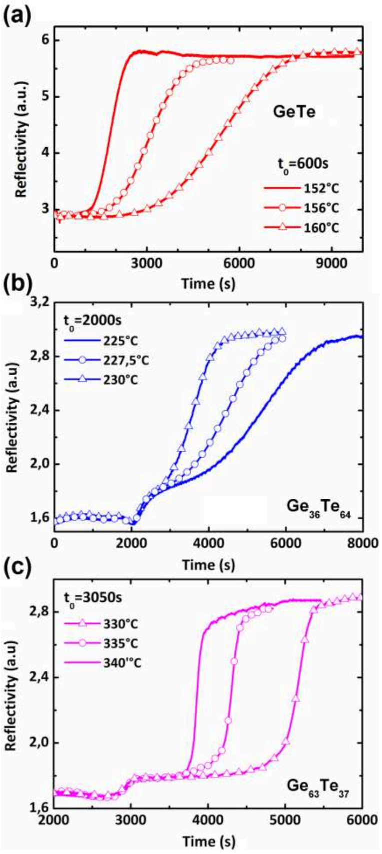

Figure 4.16 (a)(b) Time resolved reflectivity measurements performed during the isothermal annealing of GeTe, $Ge_{36}Te_{64}$ and $Ge_{63}Te_{37}$ samples. The heating ramp ends at the time t_0.

In particular, in the Te-rich alloy, fig. 4.16(b), the slope of the reflectivity vs time curve changes noticeably varying the temperature and then it's reasonable that both precipitation and GeTe crystallization contribute to the definition of E_a and τ_0. On the other hand in the Ge-rich alloy, fig. 4.16(c), this slope is quite similar in the range of the investigated temperature and then the activation energy and the pre-exponential factor are probably correlated to the diffusion mechanism and to the rearrangement of α-Ge rather than to the GeTe crystallization process (at this temperature GeTe should crystallize on a μs time scale).

Sample	$\ln(\tau_0)$ (τ_0 in s)	E_a (eV)
$Ge_{51}Te_{49}$	-71(4)	2.9(1)
$Ge_{36}Te_{64}$	-72(4)	3.4(1)
$Ge_{63}Te_{37}$	-55(4)	3.2(1)

Table 4.2 **Crystallization parameters as found by time resolved reflectivity measurements. The crystallization time is temperature (T) dependent by an exponential law according to the equation $\tau=\tau_0\exp(E_a/k_BT)$ where k_B is the Boltzmann constant.**

Moreover, a huge reduction of the pre-exponential factor τ_0 occurs varying the stoichiometry from Ge-rich (~10^{-24} s) to Te-rich (~10^{-32} s). This variation, of about 8 orders of magnitude, is linked to the lower crystallization temperature observed increasing the Te amount. It is known that the nucleation and growth pre-exponential factors are proportional to the atomic diffusivity (par. 2.2) and then this low pre-exponential factor τ_0, characteristic of phase change materials, could be related to the higher atomic diffusivity observed in the Te-rich alloy, with respect to the Ge-rich sample. Anyway, in the case of non-stoichiometric alloy, for what said, these extracted physical quantities do not have a clear meaning since several phenomena are partially entangled. Instead, in the case of stoichiometric GeTe is possible to correlate the TRR results with the direct measurement of nucleation (I) and growth (u) parameters determined by microscopic *in situ* observation. This topic was presented in sect. 2.2.1 and the relevant parameters that we are going to use here are reported in table 2.2: activation energies E_I and E_u, pre-exponential factors $\ln(u_0)$ (u in μm/s) and $\ln(I_o)$ (I in $\mu m^{-2}s^{-1}$). These parameters, are related to those accessible by TRR using the following equation

$$E_a = \frac{E_I + bE_u}{n} \leftrightarrow 2.9(1) \approx \frac{4.3 + 2 \cdot 2}{3} = 2.8(6)$$

$$\ln \tau_0 = -\frac{1}{n}(\ln(I_0) + b \cdot ln(u_0)) \leftrightarrow -71(4) \approx -\frac{1}{3}(103 + 2 \cdot 48) = 66(5)$$

where *b* is the dimensionality of the growth and *n* the Avrami exponent. It's interesting to note that all the data are consistent within the JMAK model.

4.3.5 Re-crystallization of ion and laser amorphized samples

In this section we describe the re-crystallization process of ion and laser amorphized samples. This study is intended to provide some details on the reversibility of phase transitions in non-stoichiometric GeTe alloys. A critical difference between the amorphization induced by ion and laser irradiation is that in the first case long range atomic mixing does not occur during irradiation whereas it does in the second case. In fact, laser amorphization requires the melting of the crystalline phase and then the high value of the atomic diffusivity in the liquid (~10^{-4} cm^2/s) allows a redistribution of the atomic species on a range scale of ~10 nm [Poa82]. On the other hand, ion irradiation produces the amorphous phase by the overlap of isolated damaged regions created by the collision cascade of individual ions impinging on the sample [Poa83]. It follows that, in fully crystallized non-stoichiometric GeTe alloys, ion irradiation is unable to dissolve the precipitates of the excess atomic species. Figure 4.17 shows the Raman signals of as deposited (solid line) and ion amorphized (red dotted line) Ge-rich samples: the spectra are quite similar and this suggests that both the films are amorphous. When these samples are subjected to the constant ramp thermal treatment (6°C/min), the TRR curve shows a large enhancement in the reflectivity (and therefore crystallization) already at ~135°C in the ion amorphized sample whereas, as noted before, crystallization occurs at ~354°C in the as deposited film. The Raman spectrum, fig. 4.17, indicates the presence, in the ion amorphized and then annealed (135 °C) sample (blue dashed line), of a single crystalline GeTe phase while the crystalline Ge peak at 300cm^{-1} is absent.

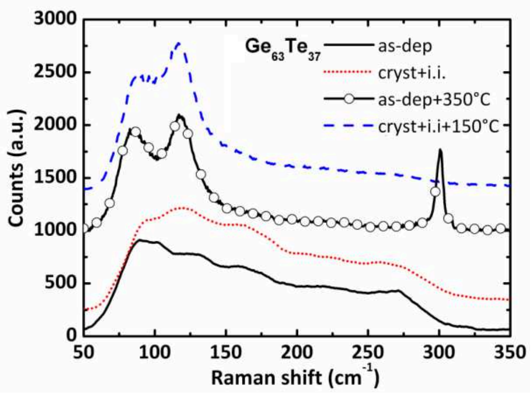

Figure 4.17 **Raman spectra of different Ge-rich samples: as deposited (solid line), ion amorphized with 10^{14} Ge^+ ions (red dotted line), ion amorphized and annealed at 150°C (blue dashed line), as deposited and annealed at 350°C (circles and solid line).**

This behaviour is not surprising since, being ion implantation unable to mix Ge precipitates with GeTe, the sample is a mixture of separated amorphous Ge and GeTe regions that crystallize at different temperatures. In fact α-Ge precipitates crystallize at ~350°C as in the as deposited sample. This temperature is too low to permit the Ge crystallization by nucleation and growth and then it is reasonable to assume that again the GeTe crystalline grains act as a seed for Ge crystallization. An ion amorphized sample, annealed at 350°C, has been analyzed by TEM and fig. 4.18 shows the electronic diffraction pattern of a region in which both crystalline GeTe and Ge are present. It is interesting to note that again, in the diffraction pattern of fig. 4.18, two zone axis are present, one for each phase, indicating an epitaxial relationship. In the ion amorphized Te-rich alloy, the Raman spectroscopy indicates that the ion irradiated sample is a mixture of amorphous GeTe and crystalline Te regions. In fact crystalline tellurium cannot be amorphized by ion irradiation since its crystallization temperature is very low (~10°C) and then the ion induced damage is immediately restored. Also in this film the recrystallization temperature, measured by TRR, is lower (~185°C) than in the as deposited sample, near to the value measured in the stoichiometric GeTe.

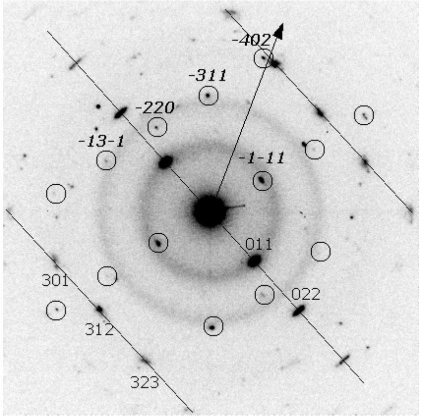

Figure 4.18 **Dark field TEM of ion amorphized and then annealed at 350°C Ge$_{63}$Te$_{37}$ sample. An alignment is again present between GeTe (lines) and Ge (circles) diffraction patterns.**

To summarize, figure 4.19(a) reports the crystallization temperature in as deposited and ion amorphized samples for the different compositions. We analyze now the re-crystallization process in laser amorphized samples. As pointed out in the previous sections, melt quenched amorphous has been obtained by a laser spot wider than 2mm and then both Raman and TRR characterization are feasible. The Raman spectra of as deposited (solid line) and laser irradiated (red dashed line) Te-rich samples are reported in fig. 4.20: the two signals are similar and this indicates that both the films are in the amorphous phase. The crystallization temperatures, measured by TRR, are almost equal, ~240°C. In this case the melting of both the crystalline phases allows a long range atomic mixing of the atomic species. Laser irradiation restores the sample to an amorphous state close to the as deposited one and then it is possible to keep the high crystallization temperature of non-stoichiometric GeTe alloys. The same behavior was also observed in the Ge-rich sample. In this case a SiO$_2$ capping layer (10nm) was deposited on the chalcogenide film to avoid evaporation during laser irradiation. The melting temperatures of Ge and GeTe are very different (940°C and 730°C) and then the laser energy density was increased to 180mJ/cm^2 to amorphize, as observed by Raman spectroscopy, both the crystalline phases. The measured re-crystallization temperature of 353°C is very close to that of the as deposited sample.

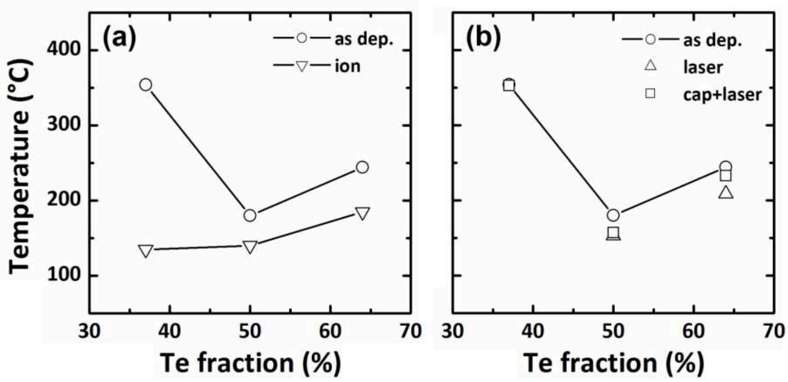

Figure 4.19 (a) Crystallization temperature, obtained by time resolved reflectivity measurements, as function of Tellurium concentration in as deposited (circles) and ion amorphized (triangles) samples. (b) Crystallization temperature as function of Tellurium concentration in as deposited (circles), laser amorphized capped (squares) and uncapped (triangles) samples.

A capping layer has been deposited on both Te-rich and stoichiometric GeTe but no appreciable variation on the re-crystallization temperature with respect to the uncapped films has been detected. TRR measurements of laser irradiated off-stoichiometric alloys show then the same features observed in the case of as deposited films. In fig. 4.19(b) all the data on the recrystallization temperature of capped and uncapped samples, are reported in comparison with the values of the as-deposited films and it is clear that the higher crystallization temperature of the non-stoichiometric alloys is preserved after the melt quenching.

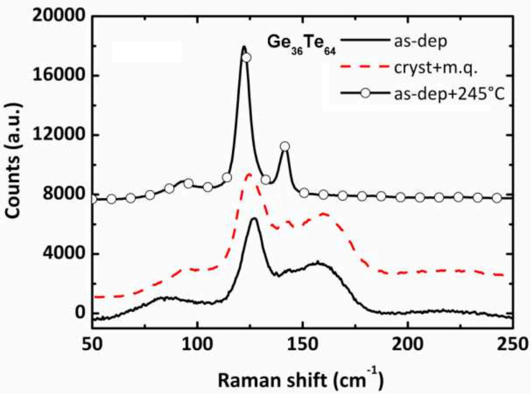

Figure 4.20 Raman spectra of different Te-rich samples: as deposited (solid line), laser amorphized (red dashed line), as deposited and annealed at 245°C (circles and solid line).

In conclusion, both TRR and Raman analyses have shown that the crystallization of laser amorphized samples proceed by the same steps observed in the case of the as deposited film, although small differences in the crystallization temperatures can be observed varying the irradiation conditions

4.4. Ion irradiation effects

We have tackled in sect. 3.6.2 and 3.6.3 the effect of low dose ion irradiation ($\phi<10^{15}$ ions/cm^2) on the crystallization kinetics and on the local order of as deposited amorphous $Ge_2Sb_2Te_5$. In this paragraph we will discuss the case of amorphous Ge_xTe_{1-x} probing the crystallization kinetic by Time Resolved Reflectivity (TRR) and the local order by Raman spectroscopy. As we will show below, the results are consistent and the same description can explain the different behavior observed varying the stoichiometry.

4.4.1 Stoichiometric GeTe

GeTe amorphous films, 40 nm thick, were irradiated at RT with 130 keV Ge^+ ions at several fluencies in the range between 10^{13}-10^{15} ions/cm^2. The beam current was kept constant to 100 nA to avoid heating of the sample. The ions projected range, by SRIM calculations [Zie85], is ~54 nm (ΔR_P=24 nm). The dose and the beam energy were chosen in such a way to avoid any appreciable change in the stoichiometry of the sample and to provide a nearly uniform energy loss (~1.35 keV $\text{ion}^{-1}\text{nm}^{-1}$) in nuclear encounters, across the sample. Some samples were implanted at the liquid-nitrogen temperature (LN_2) to ascertain the influence of irradiation-induced defects recombination. Moreover, some implants were performed through a mask to make more reliable the comparison between irradiated and unirradiated zones. Room-temperature unpolarized micro-Raman spectra were recorded in a backscattering geometry using a single spectrometer. The GeTe samples were excited with a He-Ne laser (λ=633 nm), focused using a microscope objective lens. The incident laser power was adjusted to minimize heating effects in the illuminated sample region. The crystallization of unirradiated and irradiated amorphous films was followed by *in situ* time-resolved reflectivity (TRR) using a low power He-Ne laser probe during annealing at 163 °C at a pressure of about 10^{-3} Torr. The heating rate was 10 °C/min and the settled temperature was constant within 0.1 °C. In order to obtain complementary information related to the crystallization process, transmission electron microscopy (TEM) analyses in plan-view configuration, were performed on partially crystallized pre-irradiated amorphous GeTe films, using a JEOL JEM 2010F TEM/STEM equipped with a 200 kV Schottky field emission electron gun and an ultra high resolution objective lens pole piece. The morphology of implanted GeTe samples was investigated by atomic force microscopy (AFM) analyses using a Digital Instruments Microscope Dimension 3100 in high amplitude mode with ultra sharpened Si tips. Figure 4.21(a) shows the reflectivity signal during the annealing, for as-deposited unirradiated (open circles) and irradiated amorphous GeTe films at fluence of 10^{14} ions/cm^2 at room (open triangles) or liquid-nitrogen temperature (open squares). The zero of the time scale is the time at which the settled temperature is reached. In the unirradiated GeTe the reflectivity remains initially constant up to about 15 minutes. After this transient it increases abruptly and saturates at the crystalline value when the crystallization is complete and the polycrystalline phase is formed. A similar trend occurs in the irradiated samples although the overall transformation time is considerably reduced.

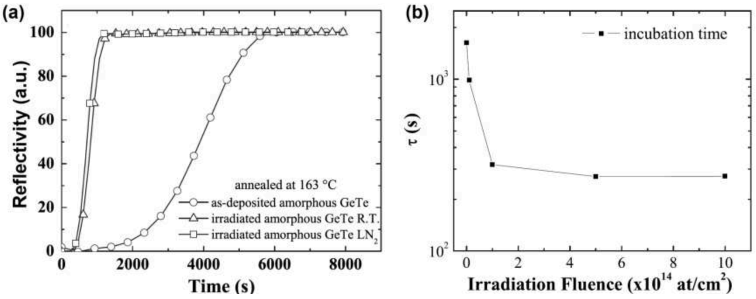

Figure 4.21 (a) Reflectivity vs annealing time at 163 °C for as deposited amorphous (open circles) and Ge^+ irradiated amorphous films at a fluence of 10^{14} ions/cm^2 performed at room (open triangles) or liquid-nitrogen temperature (open squares). (b) Incubation time τ versus implantation fluence in pre-irradiated amorphous GeTe films. The samples were annealed, after a constant heating rate, at 163 °C.

Therefore, TRR measurements indicate that the crystallization process is faster in the implanted amorphous layer with respect to the unirradiated film as observed in the case of $Ge_2Sb_2Te_5$. The temperature during irradiation does not affect the crystallization kinetics as can be inferred from the TRR curves shown relatives to samples implanted under the same conditions at different temperatures (-196°C and 25°C). This unambiguously demonstrates that any dynamic annealing process occurring during the implantation does not change the density of the defects responsible for the crystallization enhancement and that the main effect of irradiation is associated to the prompt regime of the collision cascade (thermal spike) [Nas06] and not to the delayed effect, influenced by the movement of the displaced atoms. Figure 4.21(b) reports the incubation time as a function of the irradiation fluence in preirradiated amorphous GeTe films (in the range between 10^{13}-10^{15} ions/cm^2), measured during annealing at 163 °C by means of TRR analysis. The incubation time, necessary to establish a steady-state nucleation, is here assumed to be the elapsed time until the reflectivity signal increases by 10% of its initial value. The incubation time of preirradiated amorphous films is dramatically enhanced compared to the unirradiated GeTe sample. In particular, by increasing the irradiation fluence, it exhibits an abrupt decreases until a saturation value for an implantation fluence of 10^{14} ions/cm^2.

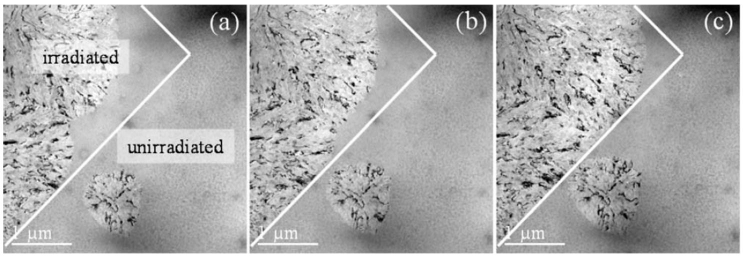

Figure 4.22 TEM plan-view micrographs of as-deposited amorphous GeTe films, implanted with 130 keV Ge^+ at 10^{14} ions/cm^2, after (a) 15 min, (b) 16 min, and (c) 17 min anneal performed at 163 °C. The presence, during implantation, of a copper mask placed on the sample surface has produced selectively implanted areas next to not-implanted areas.

To directly compare unirradiated and irradiated amorphous, some samples were prepared implanting at the saturation fluence of 10^{14} ions/cm^2 through a mask consisting of a copper grid, with holes and bar width of 36 and 25 µm, respectively, placed at the sample surface. In this way selectively implanted regions next to unimplanted areas were formed. Figure 4.22 shows a sequence of bright-field TEM image of the film surface after anneal at 163 °C for several times. At this temperature, crystallization occurs mainly inside the ion irradiated area and only at later time grains nucleate in the unirradiated region. Even the growth velocity is enhanced in the irradiated regions, the growth stops at the boundary with the unirradited area, fig. 4.22(c). The effect of the irradiation on the film density has been evaluated by measuring the step height (by atomic force microscopy) in a sample implanted through the mask grid. The AFM image of the irradiated region, shown in fig. 4.23, indicates that the ion beam induces a depression, of about 3 nm (i.e., ~7%), with respect the surface of the unirradiated regions. This vertical shrinkage is comparable to that occurring during the crystallization of GeTe due to the different density of the deposited amorphous and crystalline phases (~8%) [Non00].

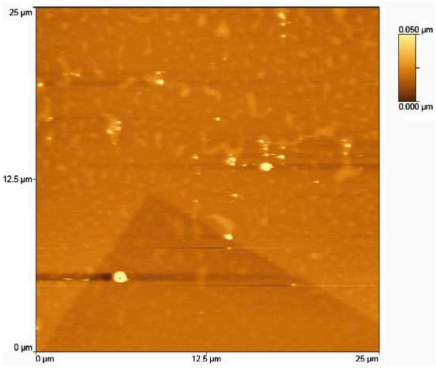

Figure 4.23 Representative AFM image for as deposited amorphous GeTe films implanted, through a mask grid, with 130 keV Ge^+ at 10^{14} ions/cm^2. Irradiated regions are depressed of 3 nm compared to those not exposed to the ion beam.

As in the case of $Ge_2Sb_2Te_5$ (fig.3.45 and sect. 3.6.2), the densification of the amorphous generated by the ion irradiation reduces considerably the mechanical stress during the phase change in line with the enhancement of the crystallization kinetics measured in the implanted samples.

As we discussed before stoichiometric GeTe crystallize by the formation of micrometric grains and then if you want to measure both nucleation and growth rate you must use an optical microscope rather than a TEM. In order to study in a reliable way the crystallization kinetics of the different GeTe amorphous systems (as deposited and ion irradiated), we have analyzed the process on as deposited samples ion irradiated trough a mask. The crystallization was investigated with an optical Mitutoyo microscope, equipped with a 20× objective lens and a stage position measurement system. Images were stored at different times, for several temperatures in the 143–155 °C range, with an optical resolution ~1 µm. A typical sequence of optical images is shown in fig. 4.24 for a sample annealed at 153 °C. The analyzed region spans both an as deposited amorphous area and a contiguous irradiated amorphous region. The sample was annealed at 153°C for different times. The enhancement of both nucleation rate and grain growth velocity in the irradiated area is clearly visible as well as the stop of the growing grains at the border of the unirradiated area.

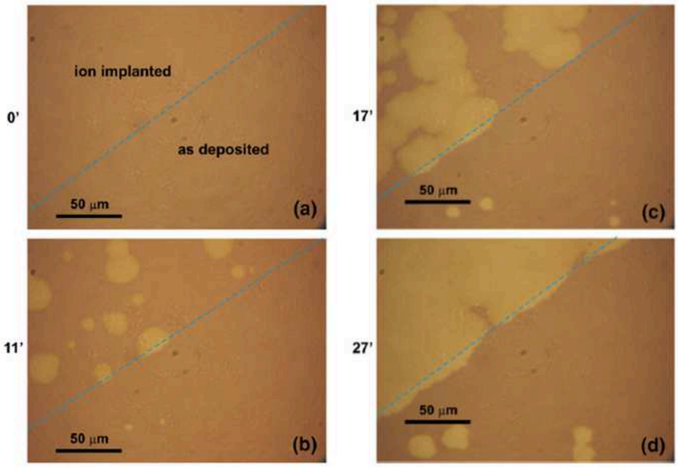

Figure 4.24 Optical sequence of a GeTe sample irradiated with Ge at a fluence of 10^{14} ions/cm^2 on the left upper region (a) and annealed at 153 °C. The crystallization dynamic is faster in the implanted region where it is complete (d) while in the contiguous unirradiated amorphous region the process is just starting. Note that the grain growth velocity slows down at the border of the unirradiated area (dashed line).

At each settled temperature several images have been stored. Starting from these images and measuring both the grain radius and the grain density as function of time is possible to extract, at several temperatures, both the nucleation and growth rates. Assuming an Arrhenius behavior, the measurements performed on both as deposited and ion irradiated areas are reported in fig. 4.25 and the results are summarized in table 4.3. The grain growth activation energy is slightly lower in the irradiated samples (1.8 eV±0.2 eV) with respect the unirradiated region (2.0 eV±0.2 eV). One might argue that they are the same within the experimental uncertainties. Vice versa, the activation energy of the nucleation rate is 4.3±0.2 eV in the as deposited sample and 4.7±0.2 eV in the irradiated sample. An opposite behavior characterizes the pre-exponential factor; it is higher for the nucleation rate of the irradiated amorphous samples and lower for the growth velocity of irradiated samples with respect to those of the unirradiated amorphous ones. The narrow accessible temperature range in which it is affordable to investigate the crystallization process does not allow then to attribute a clear physical meaning to the differences in the activation energy and pre-exponential terms.

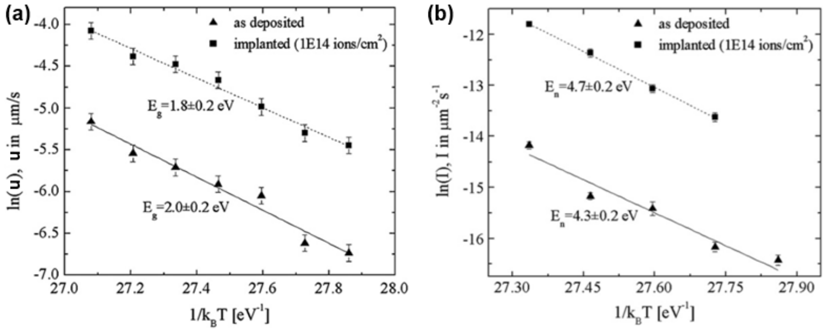

Figure 4.25 Arrhenius plot of the grain growth velocity u (a) and of the nucleation rate I (b) at several temperatures for the as deposited amorphous (triangles) and the implanted (squares) samples respectively.

Anyway, looking to the images of fig. 4.24, some interesting considerations can be inferred. At first, nucleation takes place in the irradiated area, after an incubation time shorter than that which occurred in the as deposited area. Grains grow very fast reaching the implantation interface and continuing their growth in the unirradiated region. Here, their velocity slows down to the same value found for the grains nucleated in the as deposited area. The higher value found in nucleation rate and growth velocities of irradiated film can be ascribed then to a more favorable energetic surrounding in which crystallization takes place. In this environment the lattice organization can occur easier because, probably, every step concurring to crystallization must overcome the same or near the same energy barrier encountered in the unirradiated amorphous sample, but less bonds must be rearranged (or more sites are rearranged at the same time) upon crystallization. To verify this hypothesis, we have performed Raman analyses on as deposited and ion irradiated amorphous samples. A laser irradiated amorphous sample was also prepared for comparison. Irradiation was performed by a 532 nm Nd:YAG laser (pulse duration was about 10 ns) at an energy density of 150 mJ/cm^2. The spot size was 2 mm.

	As deposited	Irradiated
Correlation coefficient (growth velocity fit)	0.98	0.992
$\ln(u_0)$ u_0 in [μm s^{-1}]	48 ± 4	44 ± 4
E_g	2.0 ± 0.2 eV	1.8 ± 0.2 eV
Correlation coefficient (nucleation rate fit)	0.97	0.9994
$\ln(I_0)$ I_0 in [/μm^{2}s]	103 ± 6	117 ± 6
E_n	4.3 ± 0.2 eV	4.7 ± 0.2 eV

Table 4.3 Crystallization parameters as found by in situ optical measurements.

Figure 4.26 shows the Raman spectra of the different amorphous samples. As discussed in par. 4.2 five main Gaussian contributions are required to fit the data but in this last figure we have put in evidence just the peaks related to the presence of Te-Te bonds.

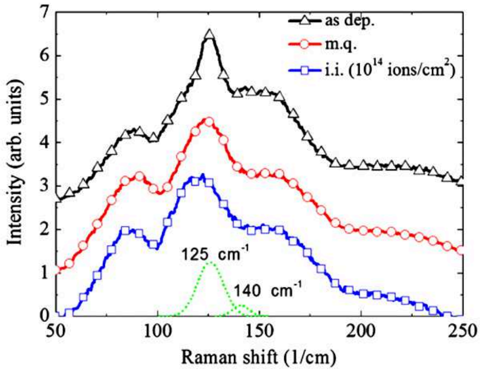

Figure 4.26 Raman spectra of different amorphous GeTe films: as deposited (open triangles), melt quenched (open circles) and ion implanted (open squares). The dotted lines represent the contribution of the 125 cm^{-1} and 140 cm^{-1} peaks to the as deposited Raman spectrum.

It's clear that after ion and laser irradiation their intensity is reduced. Therefore, in comparison with as deposited sample and according to simulations, we believe that a reduction of the homopolar Te-Te bonds, forbidden in the crystalline structure, occurs during ion and laser irradiation (sect. 3.6.3). Moreover, the Raman spectra collected in the amorphous region of partially crystallized GeTe film exhibited a reduction of the 125 cm^{-1} peak intensity similar to that observed in the irradiated samples. The optical micrograph reported in the inset of fig. 4.27, shows that the annealed sample consists of crystalline islands (white regions) embedded in an amorphous matrix (gray area). Crystalline and amorphous areas are clearly visible due to the large optical contrast between the two phases. The resulting spectra are reported in fig. 4.27.

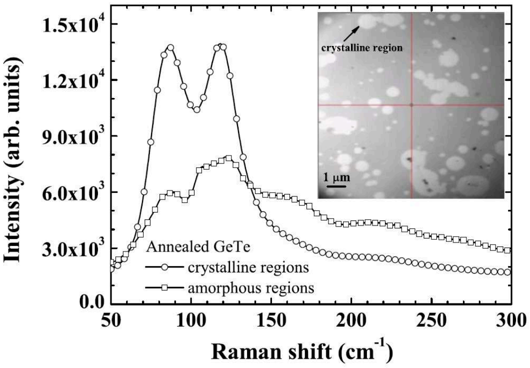

Figure 4.27 Micro-Raman spectra of (unirradiated) partially crystallized GeTe sample collected in the amorphous (open squares) and crystalline (open circles) regions. The inset reports an optical micrographs of the annealed amorphous GeTe film with a surface crystalline fraction of ~20%.

The spectra of the white regions (open circles) is typical of the crystalline GeTe film [And06] whereas the spectra collected in gray regions (open squares) differ from that of the as deposited and are similar to that of the irradiated amorphous films. Appreciable structural rearrangements took place in the amorphous network at the early stage of the phase transition and this rearrangement is similar to that occurred during irradiation. We have discussed this topic also in the case of $Ge_2Sb_2Te_5$ and both the effect and the description is very similar (sect. 3.6.2 and 3.6.3). The reduction of homopolar bonds, can be explained in terms of a selective bond rearrangement due to thermal effects. Indeed, during ion irradiation, in a dense collision cascade, energy is dissipated as a lattice vibration or heat at the end of displacement spike (T~600°C), whereas after laser irradiation, this rearrangement can occur during the cooling of the liquid phase.

4.4.2 Non-stoichiometric GeTe alloys

We have studied the effect of ion and laser irradiation also on non-stoichiometric alloys. Both laser and ion irradiation have been performed on amorphous films under the same experimental conditions described in the previous section. Time resolved reflectivity and Raman spectroscopy have been used to characterize the samples.

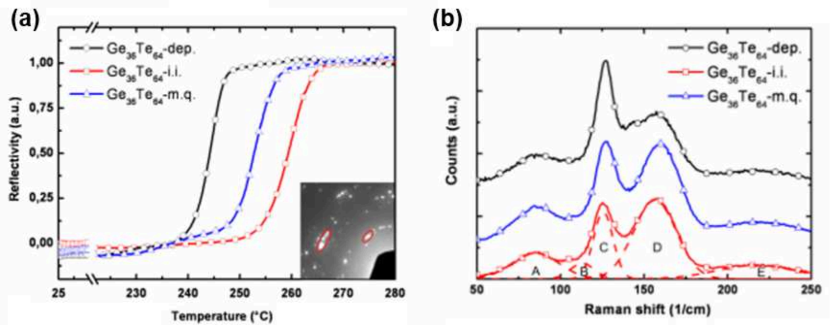

Figure 4.28 **(a) Reflectivity vs temperature curves for asdeposited (black), melt quenched (blue), and Ge^+ irradiated (red) $Ge_{36}Te_{64}$ amorphous samples. The inset shows electron diffraction pattern of the annealed sample. The (100) and (110) GeTe spots are circled, whereas the other spots refer to crystalline tellurium. (b) Comparison between the Raman spectra of the three different states of amorphous before the annealing.**

The crystallization kinetics was investigated by in situ time by TRR using a He–Ne laser probe during annealing from room temperature to 450°C. The crystallization temperature is experimentally defined as the maximum in the first derivative of the reflectivity vs temperature curve. Figure 4.28(a) shows the reflectivity signal during a heating ramp of 6°C/min for the as-deposited, ion implanted, and laser irradiated amorphous $Ge_{36}Te_{64}$ films: crystallization temperature is 244°C in the as-deposited sample, 253°C in the melt quenched (primed) sample, and 260°C in the ion implanted sample. For convenience, normalized reflectivity curves are shown. In any case, the crystallization temperature is higher than that of stoichiometric GeTe because precipitation of the Te excess species is required, sect. 4.3.1. The inset shows the electron diffraction pattern of the annealed sample; the spots of (100) and (110) GeTe are circled, whereas the other spots refer to crystalline Tellurium. Figure 4.28(b) shows the Raman spectra of the three different amorphous samples before annealing. The abscissa scale is limited to the window in which the Raman signal is present. The fitting procedure is the same discussed in par. 4.2. The integrated intensity of peak C (126 cm^{-1}), in melt quenched (primed) and ion implanted samples decreases from 22% of the as-deposited sample to 19 and to 18%, respectively. This reduction is counterbalanced by the enhancement of peak D (156 cm^{-1}) whose integrated intensity increases to 43 and 46% in melt quenched and ion irradiated samples, whereas 36% is the value for the as-deposited film. These observations suggest that both ion and laser irradiation induce the breaking of Te-Te bonds in favor of Ge–Te bond formation, agreeing with the behavior reported for the ion irradiated GeTe and $Ge_2Sb_2Te_5$. The breaking of Te–Te bonds is responsible for the higher crystallization temperature of the irradiated samples because precipitation of Tellurium is required during the alloy crystallization.

A different behavior was observed in the Ge-rich alloy. Figure 4.29(a) shows the reflectivity signal during the annealing of the as deposited, ion implanted, and laser irradiated amorphous $Ge_{63}Te_{37}$ films. The crystallization temperature is 354°C for all the samples. Crystalline GeTe and Ge are observed after the annealing, as shown in the inset of fig.4.29(a) in which the (111) and (220) Ge rings (arrows) along with other rings belonging to polycrystalline GeTe are visible. Figure 4.29(b) shows the corresponding Raman spectra of the three different amorphous samples. The spectra extend up to the region of α-Ge Raman signal as discussed in par. 4.2. Meaningful differences cannot be detected varying the amorphous status and consequently the crystallization temperature of the different samples is the same. This behavior can be understood looking to the data reported in sect. 4.3.4. The stability of the Ge-rich alloy does not depend on the amorphous state because in this case crystallization is limited by Ge mobility and the thermal spike does not cause a significant local atomic rearrangement in view of the low diffusivity. Moreover, the bonds generally involved in this local rearrangement (Te-Te, Ge-Te) don't play a relevant role upon crystallization of Ge-rich alloys since in this case it is triggered by Ge precipitation.

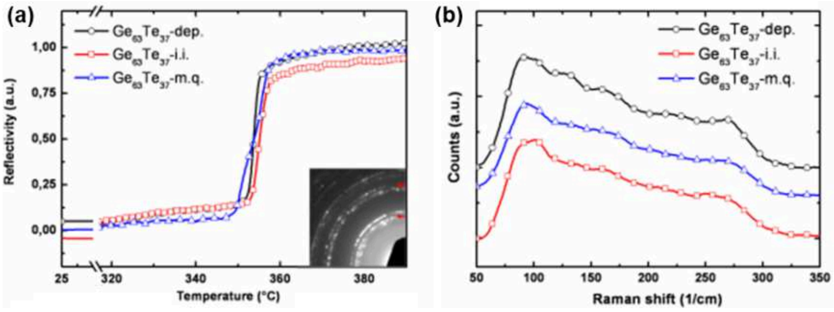

Figure 4.29 (a) Reflectivity vs temperature curves for asdeposited (black), melt quenched (blue), and Ge$^+$ irradiated (red) $Ge_{63}Te_{37}$ amorphous samples. The inset shows electron diffraction pattern of the annealed sample. The arrows point the (111) and (220) Ge diffraction rings, whereas the other rings belong to polycrystalline GeTe. (b) Comparison between the Raman spectra of the three different states of amorphous before the annealing.

It's interesting to note that ion irradiation is able to modify in a different way the crystallization kinetics of Ge_xTe_{1-x}. Despite the fact that the effect on the local order of stoichiometric GeTe and Te-rich alloy is the same (Te-Te bond breaking) the crystallization after irradiation is faster in the first case and slower in the second one. In fact, in the first case Te-Te bonds are an obstacle upon crystallization whereas in the second case their formation is the first step in the phase transition process. The amorphous Ge-rich alloy instead is not affected by ion irradiation since the atomic low diffusivity prevent the rearrangement of the amorphous network.

References

[Ako11] J. Akola, J. Larrucea, R. O. Jones, *Phys. Rev. B*, 83, 094113 (2011).

[And06] K. S. Andrikopoulos, S. N. Yannopoulos, G. A. Voyiatzis, A. V. Kolobov, M. Ribes, J. Tominaga, *J. Phys.: Condens. Matter*, 18, 965–979 (2006).

[Bru09] G. Bruns, P. Merkelbach, C. Schlockermann, M. Salinga, M. Wuttig, T. D. Happ, J. B. Philipp, M. Kund, *Appl. Phys. Lett.*, 95, 043108 (2009).

[Che86] M. Chen, K. A. Rubin, R. W. Barton, *Appl. Phys. Lett.*, 49, 502-504 (1986).

[Col96] E. G. Colgan and F. M. d'Heurle, *J. Appl. Phys.*, 79, 4087 (1996).

[Coo62] A. S. Cooper, *Acta Crystallographica*, 15, 578–582 (1962).

[Des01] I. D. Desnica-Francovic, K. Furic, U. V. Desnica, M. C. Ridgway, C. J. Glover, *Nucl. Instrum. Methods Phys. Res. B*, 178, 192–195 (2001).

[Ger79] P. Germain, K. Zeliama, S. Squelard, J. C. Bourgoin, A. Gheorghiu, *J. Appl. Phys.*, 50, 6986 (1979).

[Gho67] R. N. Ghoshtagore, *Phys. Rev.*, 155, 598-602 (1967).

[Han58] M. Hansen, *Constitution of binary alloys*, McGraw-Hill, New York (1958).

[Hug08] E. Huger, U. Tietze, D. Lott, H. Bracht, D. Bougeard, E. E. Haller, H. Schmidt, *Appl. Phys. Lett.*, 93, 162104 (2008).

[Joh08] B. G. Johnson, P. Gortmaker, J. C.McCallum, *Phys. Rev. B*, 77, 214109 (2008).

[Kim09] C. Kim, D. Kang, T. Y. Lee, K. H. P. Kim, Y. S. Kang, J. Lee, S. W. Nam, K. B. Kim, Y. Khang, *Appl. Phys. Lett.*, 94, 193504 (2009).

[Kol04] A. V. Kolobov, P. Fons, J. Tominaga, A. Lankudinov, S. N. Yannopoulos, K. S. Andrikopoulos, *J. Phys.: Condens. Matter*, 16, S5103–S5108 (2004).

[Maz10] R. Mazzarello, S. Caravati, S. Angioletti-Uberti, M. Bernasconi, M. Parrinello, *Phys. Rev. Lett.*, 104, 085503 (2010).

[Mor95] G. Morell, F. L. S. Katiyar, S. Z. Weisz, H. Jia, J. Shinar, I. Balberg, *J. Appl. Phys.*, 78, 5120 (1995).

[Nam09] S. W. Nam, C. Kim, M. H. Kwon, H. S. Lee, J. S. Wi, D. Lee, T. Y. Lee, Y. Khang, K. B. Kim, *Appl. Phys. Lett.*, 92, 111913 (2009).

[Nas06] M. Nastasi, J.W. Mayer, *Ion Implantation and Synthesis of Materials*, New York (2006).

[Non00] T. Nonaka, G. Ohbayashi, Y. Toriumi, Y. Mori, and H. Hashimoto, *Thin Solid Films*, 370, 258 (2000).

[Oka86] T. Okabe, M. Nakagawa, *Journal of Non-Crystalline Solids*, 88, 182–195 (1986).

[Pin71] A. S. Pine and G. Dresselhaus, *Phys. Rev. B*, 4, 356 (1971).

[Poa82] J. M. Poate, J. W.Mayer, Laser Annealing of Semiconductors, Academic, New York (1982).

[Poa83] J. M. Poate, G. Foti, D. Jacobson, Surface Modification and Alloying by Laser, Ion, and Electron Beams, Plenum, New York (1983).

[Rao09] S. Raoux, H.-Y. Cheng, M. A. Caldwell, H.-S. P. Wong, *Appl. Phys. Lett.*, 95, 071910 (2009).

[Rao09b] S. Raoux, B. Munoz, Huai-Yu Cheng, J. L. Jordan-Sweet, *Appl. Phys. Lett.*, 95, 143118 (2009).

[Rui02] G. Ruitenberg, A. K. Petford-Long, R. C. Doole, *J. Appl. Phys.*, 92, 3116 (2002).

[Wyc63] R. W. G. Wyckoff, *Crystal Structures* vol. 1, Interscience Publishers, New York (1963)

[Zie85] J. F. Ziegler, J. P. Biresack, U. Littmark, *The Stopping and the Range of Ions in Solids*, Pergamon, New York, (1985).

Conclusions

Aim of this work was the investigation of the phase transitions in $Ge_2Sb_2Te_5$ and Ge_xTe_{1-x} thin films. These alloys are of interest since they exhibit an excellent combination of electrical-optical and phase changing characteristics for memory applications. This topic has been reviewed in Chapter 1 looking to the huge amount of studies reported in the literature. In particular we have focused our attention on the amorphous-crystal transition and the theory of crystallization in solids has been then discussed in Chapter 2. The uniqueness of this class of materials consists in the combination of high structural stability of both phases up to moderate temperatures (T~150 °C) and extremely fast phase transitions (t~10-100 ns) at higher temperatures.

As reported in Chapter 3, we have investigated the crystallization process in both these regimes providing a unified analysis of these results. In contrast to covalent semiconductors (e.g. Si and Ge), the amorphous state of phase change materials exhibits the characteristics of a *fragile* liquid. As a consequence, the crystallization speed (nucleation and growth) increases more rapidly with temperature near the glass transition temperature rather than near the melting point.

We have also discussed the correlation between the local order in the amorphous network and the crystallization kinetics. To this aim we have modified the properties of the amorphous phase by laser and ion irradiation looking to the consequent variation in the phase transition speed (par. 3.6 and 4.4). In stoichiometric alloys the amount of homopolar bonds (Ge-Ge or Te-Te), not allowed in the crystalline phase, strongly influence the amorphous stability. Upon laser or ion irradiation a reduction in the abundance of these bonds has been measured coupled with a faster crystallization kinetics.

In non stoichiometric alloys, we have detailed the crystallization mechanism near the glass transition temperature. The precipitation process represents the first step of the crystallization process and then, as a consequence, a different scenario has been described with respect to stoichiometric films (par. 4.3).

We have also investigated the crystallization process of $Ge_2Sb_2Te_5$ in presence of an amorphous-crystal interface to verify, on a nanometric scale, if, near the glass transition temperature, the crystallization occurs via nucleation of the new phase or by the growth from the amorphous-crystal rim. This second hypothesis has been demonstrated in par. 3.4.

In conclusion we have also demonstrated that is possible to dope chalcogenide thin film performing ion irradiation on a capped sample. The capping layer can be selected to introduce by recoil implantation suitable doping species (e.g. Si and O) that affect the crystallization kinetics of the active layer by the formation of new atomic bonds (sect. 3.6.4).

List of Publications

This thesis is based on the following publications:

1) *Amorphous-crystal phase transitions in Ge_xTe_{1-x} alloys.* Carria E., Mio A.M., Gibilisco S., Miritello M., Bongiorno C., Grimaldi M.G., Rimini E. *Journal of The Electrochemical Society (In press).*

2) *Polymorphism of amorphous $Ge_2Sb_2Te_5$ probed by EXAFS and Raman spectroscopy.* Carria E., Mio A.M., Gibilisco S., Miritello M., d'Acapito F., Grimaldi M.G., Rimini E. *Electrochemical and Solid-State Letters 14 (12) H480-H482 (2011).*

3) *Ion irradiation on phase change materials.* Rimini E., Carria E., Mio A. M., Miritello M., Gibilisco S., Bongiorno C., D'Arrigo G., Spinella C., D'Acapito F., Grimaldi M. G. *Mat. Res. Soc. Symp. Proc. 1354, pp. ii06-06, (2011).*

4) *Tuning the crystallization temperature of amorphous $Ge_2Sb_2Te_5$ by O and Si Recoil Implantation.* Carria E., Mio A.M., Gibilisco S., Miritello M., Grimaldi M.G., Rimini E. *Electrochemical and Solid-State Letters 14 (3), H124-H127 (2011).*

5) *Nucleation and grain growth in as deposited and ion implanted GeTe thin films*. Mio A.M., Carria E., D´Arrigo G., Gibilisco S., Miritello M., Grimaldi M.G., Rimini E. *Journal of Non-Crystalline Solids 357, 2197–2201 (2011).*

6) *Local order and crystallization of laser quenched and ion implanted amorphous Ge_xTe_{1-x} thin films.* Carria E., De Bastiani R., Gibilisco S., Mio A. M., Miritello M., Pennisi A. R., Bongiorno C., Grimaldi M. G., Rimini E. *Mat. Res. Soc. Symp. Proc. 1251, H02-08 (2010).*

7) *Local order and crystallization of laser quenched and ion implanted amorphous Ge_xTe_{1-x} thin Films.* Carria E., Mio A. M., Miritello M., Gibilisco S., De Bastiani R., Pennisi A. R., Bongiorno C., Grimaldi M. G., Rimini E. *Electrochemical and Solid-State Letters 13 (9), H317-H320 (2010).*

8) *Crystallization of ion amorphized $Ge_2Sb_2Te_5$ thin films in presence of cubic or hexagonal phase.* De Bastiani R. , Carria E., Gibilisco S., Bongiorno C. , Piccinelli F., Grimaldi M. G., Rimini E. *J. Appl. Phys. 107, 113521 (2010).*

9) ***Crystallization of ion amorphized $Ge_2Sb_2Te_5$ in nano-structured thin films.*** **Mio A.M., Carria E., De Bastiani R. , Miritello M., Bongiorno C. , D´Arrigo G. , Spinella C. , Grimaldi M.G. , Rimini E.** ***Mat. Res. Soc. Symp. Proc. 1251, H02-03 (2010).***

10) ***Ion-irradiation-induced selective bond rearrangements in amorphous GeTe thin films.*** **De Bastiani R., Carria E., Gibilisco S., Grimaldi M.G., Pennisi A. R., Gotti A., Pirovano A., Bez R., Rimini E.** ***Phys. Rev. B 80, 245205 (2009).***

11) ***Crystallization of sputtered-deposited and ion implanted amorphous $Ge_2Sb_2Te_5$ thin films.*** **Rimini E., De Bastiani R., Carria E., Grimaldi M.G., Nicotra G., Bongiorno C., Spinella C.** ***J. Appl. Phys. 105, 123502 (2009).***

12) ***Evolution of the transrotational structure during crystallization of amorphous $Ge_2Sb_2Te_5$ thin films.*** **Rimini E., De Bastiani R., Carria E., Grimaldi M.G., Nicotra G., Bongiorno C., Spinella C.** ***Mat. Res. Soc. Symp. Proc. 1160, 1160-H12-08 (2009).***

Other publications:

13) ***Novel approach to the fabrication of Au/Silica core-shell nanostructures based on nanosecond laser irradiations of thin Au films on Si.*** **F. Ruffino, A. Pugliara, E. Carria, L. Romano, C. Bongiorno, C. Spinella, M. G. Grimaldi.** ***Nanotechnology*** **(in press)**

14) ***Towards a laser fluence dependent nanostructuring of thin Au films on Si by nanosecond laser irradiation.*** **F. Ruffino, A. Pugliara, E. Carria, L. Romano, C. Bongiorno, G. Fisicaro, A. La Magna, C. Spinella, M. G. Grimaldi.** ***Applied Surface Science*** **(in press).**

15) ***A combined ion implantation/nanosecond laser irradiation approach towards Si nanostructures doping.*** **F. Ruffino, L. Romano, E. Carria, M. Miritello, M. G. Grimaldia, V. Privitera, F. Marabelli.** ***Journal of Nanotechnology*** **(in press)**

16) ***High-level incorporation of antimony in germanium by laser annealing.*** **Bruno E., Scapellato G. G., Bisognin G., Carria E., Romano L., Carnera A., and Priolo F.** ***J. Appl. Phys. 108, 124902 (2010).***

17) ***Role of the strain in the epitaxial regrowth rate of heavily doped amorphous Si films.*** **D´Angelo D., Romano L., Crupi I., <u>Carria E.</u>, Privitera V., Grimaldi M.G.** ***Appl. Phys. Lett. 93, 231901 (2008).***

Curriculum vitae

Egidio Carria was born on 13th of March 1984 in Catania. He attained his Master Degree in Physics from the University of Catania in 2008 (110/110 *cum laude*). In 2008 was also admitted to the Ph.D. course in Physics at the University of Catania. He is currently working under the supervision of Prof. Maria Grazia Grimaldi and Prof. Emanuele Rimini. The main scientific interest is focused on the study of phase transitions in chalcogenide materials (PCM). In particular, his research activity is devoted to the understanding of the structural properties of thin chalcogenide films and of their modification under ion and laser irradiation. On the other hand, he has been involved in experimental studies concerning laser annealing of semiconductor and metallic thin films. He has also collaborated with CNR-IMM-Matis in Catania and with CNR-IOM-OGG, ESRF-GILDA beam line, in Grenoble. During the Ph.D. course he has presented the results of his work at the following conferences giving oral and poster contributions: E\PCOS 2009 (Aachen, Germany), MRS-Spring Meeting 2010 (San Francisco, USA), E\PCOS 2010 (Milano, Italy), MRS-Spring Meeting 2011 (San Francisco, USA), E-MRS-Spring Meeting 2011 (Nizza, Francia). He has attended a training at the European Synchrotron Radiation Facility (ESRF), GILDA beam line, January 2011, Grenoble, France. He has also attended the “47th Course of the International School of Solid State Physics on Materials for Renewable Energy”, Erice, Italy. Moreover, Egidio Carria is author or co-author of several articles, published in international referred scientific journals.